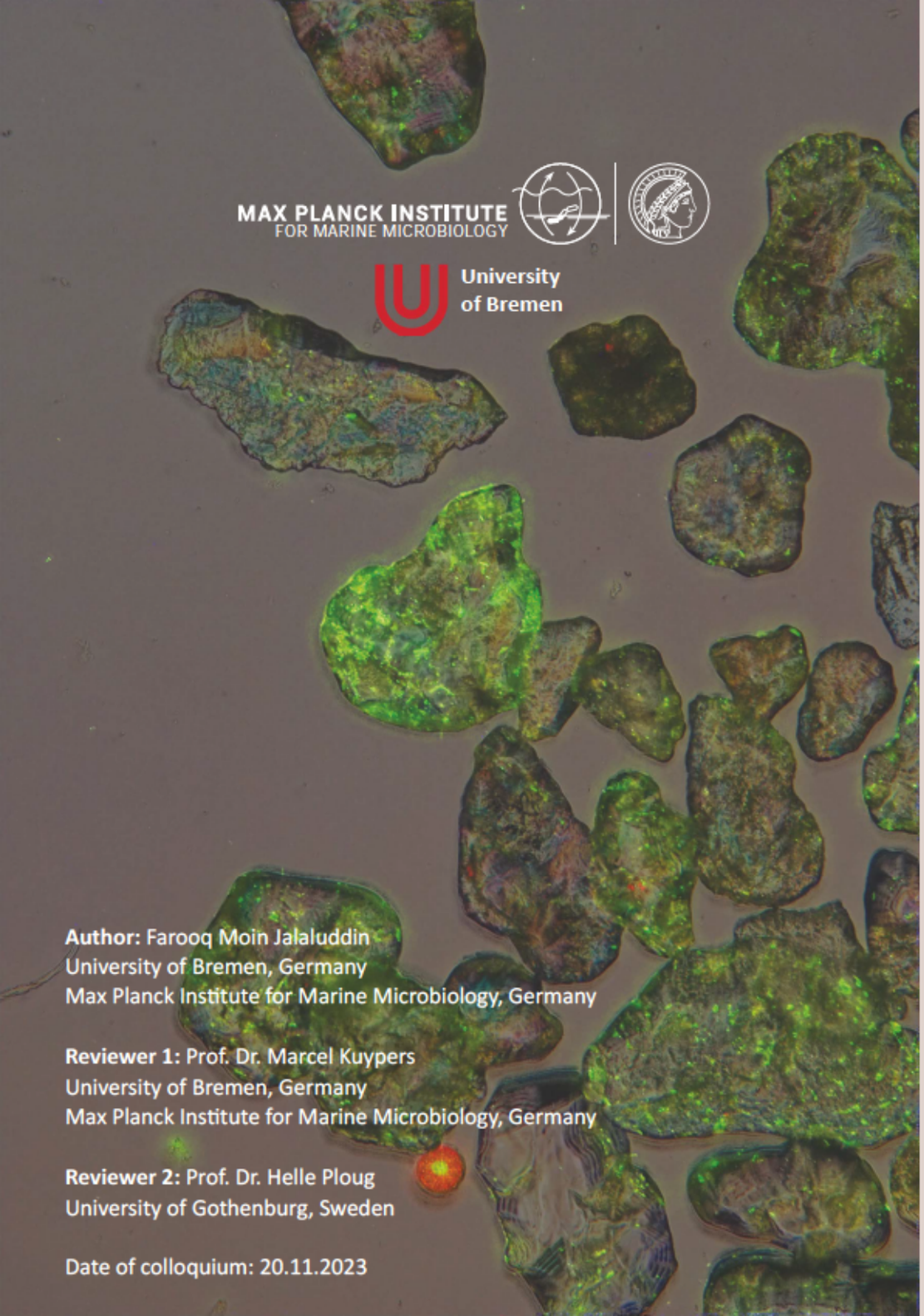

MAX PLANCK INSTITUTE
FOR MARINE MICROBIOLOGY

University
of Bremen

Author: Farooq Moin Jalaluddin
University of Bremen, Germany
Max Planck Institute for Marine Microbiology, Germany

Reviewer 1: Prof. Dr. Marcel Kuypers
University of Bremen, Germany
Max Planck Institute for Marine Microbiology, Germany

Reviewer 2: Prof. Dr. Helle Ploug
University of Gothenburg, Sweden

Date of colloquium: 20.11.2023

Microscale insights into marine biogeochemical cyling:
Linking microbial activity and mass transfer

Farooq Moin Jalaluddin

Microscale insights into marine biogeochemical cyling: Linking microbial activity and mass transfer

Farooq Moin Jalaluddin

Doctoral Thesis

Microscale insights into marine biogeochemical cycling: Linking microbial activity and mass transfer

Dissertation

zur Erlangung des Grades eines Doktors der Naturwissenschaften

- Dr. rer. nat. -

im Fachbereich Geowissenschaften

der Universität Bremen

Farooq Moin Jalaluddin

Bremen, Juli 2023

Diese Arbeit wurde in der Zeit vom März 2019 bis Juli 2023 im Rahmen des Programms „The International Max Planck Research School of Marine Microbiology“ (MarMic) angefertigt. Die Ergebnisse dieser Arbeit wurden am Max-Planck-Institut für Marine Mikrobiologie in der Abteilung Biogeochemie erarbeitet.

Autorin: **Farooq Moin Jalaluddin**

Universität Bremen

Max-Planck-Institut für Marine Mikrobiologie

Gutachter: **Prof. Dr. Marcel M. M. Kuypers**

Universität Bremen

Max-Planck-Institut für Marine Mikrobiologie

Zweitgutachter: **Prof. Dr. Helle Ploug**

Göteborgs Universitet, Göteborg

Table of contents

Acknowledgements

I would like to extend my heartfelt appreciation to all those who have supported me throughout these years. This encompasses both the professional aspects of my work and the personal aspects of my life, which have collectively made my time in Bremen truly enjoyable.

To begin with, I would like to thank **Marcel Kuypers** for the opportunity to do my doctoral research in the department of biogeochemistry. I really enjoyed the engaging and encouraging discussions with you. Thank you very much for the extensive scientific knowledge, innovative ideas, sharing the enthusiasm about science, and guiding me to the right direction.

A special thanks to **Helle Ploug**, for taking the time to review this thesis.

I am deeply appreciative to **Soeren Ahmerkamp** for trusting in me and guiding me through various aspects of research, such as coding, modeling, lander deployments, microfluidics, sediment and many more. Thank you so much for making sure that I was not getting lost in this journey and making sure that I was acquiring the necessary skills for a good research. I am also immensely grateful for your advices on general stuff during my good and otherwise situations, for staying patient with me, for all the fun during expeditions, for teaching me swimming in Elba, for keeping the office door open for my all types of questions. I am also thankful to you for keeping me enthusiastic and making science so much fun.

I want to thank **Hannah Marchant**, for introducing me to life in Bremen, helping me with label isotopic incubations and preparation for the cruises. I always enjoy our conversations and discussions during coffee break. I am thankful for all the fruitful discussions, for improving my scientific writing, checking on me during the pandemic, for bearing with me through many ups and downs, and for keeping the energy always positive. I appreciate all your help.

Another special thanks to **Klaus Koren**, for his valuable feedback during my thesis committee meetings and enlightening me so much about optical imaging and sensor particles.

Thank you to all the other members of my thesis committee meetings, **Arjun Chennu**, **Jana Milucka**, and **Frank Wenzhöfer**, for the interpretations of results and very helpful suggestions.

Thank you to **Daniela Tienken**, for teaching me Raman spectroscopy and always helping me in the laboratory. Thank you for magically finding the right thing that I needed for the experiments.

Another special thanks to **Jan von Arx** for sharing the office with me, from start till the end of our PhDs, for all the interesting scientific and non-science discussions, for the fun during conference, for changing gas bottles with me, for your trust in my farming skills. I really enjoyed the time with you.

Abiel and **Margaritha**, I would like to thank you for being with me, during the tough and fun times, for checking on me when I stayed late in the laboratory, for listening to my endless problems and for helping me. I enjoyed all the tea breaks and walks we had.

Bram, Sina, and **Wiebke** – Thank you for positively engaging in my off-science conversations and all the useful informations. **Boran,** Thank you for sharing your cheerful views on different aspects of life and for promoting my Egypt trip. **Tim, Gaute** – Thank you for enlightening me more about science. **Sten –** I really appreciate all the SEM measurements you did for me.

Thanks to all my present and former office mates, **Jan, Nadine, Sina, Margaritha, Abiel, Siqi,** and **Linus**, for letting the office environment have a spark. I always had something to look forward in the mornings.

Miriam, Nadine, Clarissa, Kathi, Inma, Niek, Julia, Margaritha – Thank you for always helping me out and answering all my queries, for the fun conversations during lunch and super helpful suggestions. Extended thanks to **Miriam** and **Nadine** for always listening to me so patiently and making sure that I am fine.

Paloma, Valeria, Fabian, Jördis, Carolin, Juliane and **Siqi** – Thank you for always keeping the office door open for me, for all sort of random conversations. I find great joy in our spontaneous discussions that seem not-very-scientific but are truly cherished moments.

Gabi, Kirsten, Swantje, Sandra, Nadine, Nina, and **Mandy** – Thank you all so much for your help and making things work on the right time always.

Ulrike – I really appreciate all the support and help in organizing meetings, small celebrations, conferences, and expeditions.

Thank you to all the biogeos, for making working her so much fun and for all your feedback

Volker, Paul, Fabian S., Benjamin, Tomas, and **Oliver** – Thank you for helping in the lander hall, 3D printing, licenses of the software, and finding innovative quick solutions to technical issues.

Paloma, Hagen, Grace, and Marion – It was super fun to be a PhD Representative with you all. **Marion, Grace, Ida, Asli, Cas, Judith, Hailey, Louison, Anna S., Anna W., Mertcan, Hanna, Qiong, Benny, Shengjie** – Thank you so much for all the good time we have spent together in Bremen and all the laughter

Fabian, Paloma, Siqi, Abiel and **Clarissa** – Thank you for proofreading the text for my thesis.

Thank you to **Fabian, Juliane, Aman, Carolin, Nina,** and **Andrea,** for all the time we have spent discussing microfluidics and working in the lab together. **Fabian,** I have a deep appreciation for all our discussions we had about sands, fluxes, microfluidics, humans, chess, and football games. **Juliane**, Thank you for being a part of the microfluidic facility from the beginning, for all our lively conversations during the walk breaks and for making working in the lab an enjoyable and fulfilling experience. I extend my heartfelt thanks to **Vipul** and **Chandni** for their unwavering presence and support.

Thank you for to my Hamburg-gang and Desi-gang for making life in Germany far from home so much fun – **Gayas, Umair, Shivam, Arina, Erina, Tomas, Sumbal, Hameed, Hashir, Ahraar, Farman, Nasif, Nabeel, Ayush, Christina, Amro, Karthik, Anzar, Hammad, Muskan, Ayesha, Fariha, Asad**… Special thanks to **Imran** for always listening to me and making time for me. People back home who made all this easy and possible, **Tarang, Prateekshah, Ali, Anas, Ashraf, Adnan, Nupur, Yaseen uncle**…

Abbu, **Ammi**, **Baji, Wasif bhai** and **Umar**, all this would had not been possible without you. Thank you so much for all the trust, support and blessings. I can never find right words to thank you enough. Al-Ḥamdu lillāh for everything.

Summary

Microbial transformations are fundamental drivers of biogeochemical cycling in marine environments. While larger-scale processes undoubtedly shape marine microbial communities, the life of individual microorganisms is intricately governed by processes occurring at a much smaller scale, ranging from micrometers to millimeters. At these scales, the solute concentration available to the microbial community is influenced by the interplay between transport processes and microbial metabolism. However, our current understanding of microbially mediated biogeochemical processes within such microenvironments is still limited. The aim of this thesis was to study the interplay of mass transfer and microbial reaction rates to determine how they govern biogeochemical cycling in microenvironments. To gain insights into these processes, microfluidic techniques were developed and combined with modeling studies to quantify and explore microscale transport processes.

The study in **chapter 2** aimed to assess the role of oxic sandy sediments in removing anthropogenic nitrogen inputs to the continental shelves by quantifying the contribution of anoxic microenvironments in nitrogen loss. We used oxygen-sensitive sensor particles in a microfluidic device to map oxygen production and consumption rates on the surface of individual sand grains. The results showed significant variability in oxygen production and consumption rates on individual sand grain surfaces, suggesting the formation of distinct microenvironments. Integration of microfluidic data into a two-dimensional single sand grain model revealed that the formation of anoxic microenvironments is controlled by solute supply and microbial oxygen production and consumption rates. Subsequently, a non-dimensional number derived from the model was used to estimate the volumes of anoxic microenvironments and calculate associated nitrogen loss. The

findings indicated that nitrogen loss in the North Sea could be underestimated by approximately 40%.

To further investigate the impact of flow on microscale transport processes and activity within microenvironments, we utilized oxygen-sensitive sensor particles in conjunction with advanced imaging techniques to simultaneously visualize oxygen concentrations and flow fields (**chapter 3**). The method proved highly effective in non-invasively visualizing the microscale transport processes in the boundary layer, allowing us to visualize oxygen concentrations within and around a model laboratory aggregate. We further show how this novel approach can be used in other marine microenvironments, examining the exchange processes facilitated by cilia on corals. The results show the importance of flow in determining oxygen concentrations and the potential for different microbial metabolisms in marine microenvironments.

The activity of microorganisms residing in distinct microenvironments was investigated in **chapter 4** using a newly developed microfluidic device for cultivating cells under well-defined solute concentrations. By cultivating marine bacteria under controlled oxic and anoxic conditions, we observed variable growth rates attributed to different energy yields from aerobic respiration and fermentation. Automated image segmentation revealed delayed morphological adaptations in response to changing oxygen concentrations. This study emphasizes the diversity within the microbial community residing in different microenvironments.

The combined findings from this thesis show that microbial activity and behavior within seemingly uniform environments are influenced by microscale gradients of solute resulting from mass transport and microbial reaction rates. The work presented in this thesis, through microfluidics, imaging techniques, and modeling

studies, highlights the intricate interplay of solute transport and microbial reaction rates, ultimately determining the solute availability in microenvironments. Microbial activity within these distinct microenvironments likely plays a key role in biogeochemical cycling in the oceans.

Zusammenfassung

Mikrobielle Umsatzraten sind fundamentale Treiber biogeochemischer Kreisläufe in marinen Systemen. Während großskalige Prozesse die marine mikrobielle Gemeinschaft formen, wird das Leben der einzelnen Organismen von mikroskaligen Prozessen, im Bereich von Mikrometern bis Millimetern, dominiert. Auf dieser Skala wird die Konzentration gelöster Stoffe, die der mikrobiellen Gemeinschaft zur Verfügung stehen, vom Wechselwirken zwischen Transportprozessen und Stoffwechsel beeinflusst. Unser gegenwärtiges Verständnis der mikrobiell gesteuerten biogeochemischen Prozesse innerhalb solcher Mikroumgebungen ist jedoch begrenzt. Das Ziel dieser Dissertation war es, das Zusammenspiel von Massentransfer und mikrobiellen Reaktionsraten zu untersuchen und zu verstehen, wie diese die Stoffkreisläufe in Mikronischen steuern. Um Einblicke in kleinskalige Transportprozesse zu gewinnen und diese zu quantifizieren, wurden Techniken der Mikrofluidik entwickelt und mit Modellierungsansätzen kombiniert.

Die Studie in Kapitel 2 beschäftigt sich damit, wie sauerstoffhaltiger Sand dazu beiträgt, anthropogen zugeführten Stickstoff auf Kontinentalschelfen zu entfernen. Hierzu wurde der Beitrag anoxischer Mikroumgebungen zum Stickstoffverlust quantifiziert. Wir verwendeten sauerstoffsensitive Sensorpartikel in einer mikrofluidischen Vorrichtung, um die Sauerstoffproduktions- und Sauerstoffverbrauchsraten auf der Oberfläche einzelner Sandkörner zu erfassen. Die Ergebnisse zeigten eine signifikante Variabilität der Sauerstoffproduktions- und Sauerstoffverbrauchsraten auf den Oberflächen einzelner Sandkörner, was auf die Bildung unterschiedlicher Mikroumgebungen hindeutete. Ein zweidimensionales Modell der mikrofluidischen Prozesse auf einem einzelnen Sandkorn zeigte, dass sich anoxische Mikroumgebungen bilden, abhängig von der Versorgung mit gelösten

Substanzen und der mikrobiellen Sauerstoffproduktions- und Sauerstoffverbrauchsraten. Anschließend wurde eine dimensionslose Kennzahl aus dem Model abgeleitet, um die Volumina anoxischer Mikroumgebungen zu schätzen und den damit verbundenen Stickstoffverlust zu berechnen. Die Ergebnisse deuten darauf hin, dass der Stickstoffverlust in der Nordsee nach aktuellen Berechnungen möglicherweise um etwa 40 % unterschätzt wird.

Um die Auswirkungen von Strömung auf mikroskalige Transportprozesse und die Aktivität innerhalb von Mikroumgebungen weiter zu untersuchen (Kapitel 3), verwendeten wir sauerstoffsensitive Sensorpartikel in Kombination mit hochentwickelten Bildgebungstechniken, um Sauerstoffkonzentrationen und Strömungsfelder gleichzeitig zu visualisieren. Die Methode erwies sich als äußerst effektiv darin, mikroskalige Transportprozesse in der Grenzschicht nicht-invasiv darzustellen und ermöglichte uns, die Sauerstoffkonzentrationen innerhalb und um ein Modellpartikel herum unter Laborbedingungen zu visualisieren. Wir zeigten auch, wie dieser neuartige Ansatz in anderen marinen Mikroumgebungen angewendet werden kann, indem wir den Austauschprozess, der durch Zilien an Korallen ermöglicht wird, untersuchten. Die Ergebnisse heben die Bedeutung der Strömung für Sauerstoffkonzentrationsmessungen und für verschiedene mikrobielle Stoffwechselprozesse in marinen Mikroumgebungen hervor.

Die Aktivität von Mikroorganismen, die in verschiedenen Umgebungen leben, wurde in Kapitel 4 mit einer neu entwickelten mikrofluidischen Technik untersucht, bei der Zellen unter definierten Stoffkonzentrationen kultiviert werden. Durch kontrollierte sauerstoffhaltige und sauerstofffreie Bedingungen beobachteten wir variable Wachstumsraten mariner Bakterien, die auf die unterschiedlichen Energieerträge aus aerobem Atmen und Fermentation zurückzuführen sind. Eine automatisierte Bildsegmentierung enthüllte verzögerte morphologische Anpassungen als Reaktion auf wechselnde

Sauerstoffkonzentrationen. Diese Studie illustriert die Vielfalt innerhalb der mikrobiellen Gemeinschaft, die in unterschiedlichen Milieus anzutreffen ist.

Die Erkenntnisse dieser Dissertation zeigen, dass die mikrobielle Aktivität und das Verhalten innerhalb scheinbar homogener Umgebungen von mikroskaligen Gradienten gelöster Stoffe beeinflusst werden, die aus dem Massentransport und mikrobiellen Reaktionsraten resultieren. Die in dieser Arbeit präsentierten Studien, unter Anwendung von Mikrofluidik, Bildgebungstechniken und Modellierungsansätzen, verdeutlichen das komplexe Zusammenspiel von Stofftransport und mikrobiellen Umsatzraten, das letztendlich die Verfügbarkeit gelöster Substanzen in Mikroumgebungen bestimmt. Die mikrobielle Aktivität innerhalb dieser unterschiedlichen Mikroumgebungen spielt vermutlich eine zentrale Rolle in den biogeochemischen Kreisläufen der Ozeane

Chapter 1

Introduction

Introduction

Marine microorganisms drive a vast range of chemical reactions by leveraging the thermodynamic imbalances created through the availability of different electron donors and acceptors (Falkowski et al., 2008; Hutchins & Fu, 2017). These reactions control large-scale biogeochemical cycles in the oceans, including carbon fixation, nitrogen cycling and the breakdown of the organic matter and thereby regulate the Earth system (Falkowski et al., 2008). On broad scales (meters to kilometers) biogeochemical processes are spatially separated within the oceans due to the availability of substrates such as oxygen and nitrate, and other factors such as light penetration (Azam et al., 1983; Ducklow et al., 1986). For example carbon fixation is mainly concentrated in the sunlit upper waters where photosynthesis can occur, while nitrogen cycling processes are partitioned across oxic and anoxic waters. However, the ocean is not only heterogeneous at large scales, but also over the micrometer to millimeter scales that are directly relevant to microbes (Azam, 1998; Stocker, 2012). In the last decades it has become clear that solute availability is patchy in the oceans at the microscale (Revsbech et al., 1980; Seymour & Stocker, 2018), and as a result microorganisms live in a sea of gradients (Azam & Long, 2001; Fenchel, 2002), which differ from the bulk concentrations observed using typical oceanography techniques. These solute-rich patches give rise to microscale zones known as microenvironments.

Microenvironments have distinct physical, chemical, and biological properties compared to the surrounding waters (Anderson & Meadows, 1978; Seymour & Stocker, 2018), leading to diverse microbial colonization and activity (Azam & Long, 2001; Falkowski et al., 2008). These microenvironments exist at various scales, ranging from millimeters around larger organisms like fishes (Sar & Rosenberg, 1987), sponges (M. W. Taylor et al., 2007), corals (Ochsenkühn et al., 2018; Pacherres et al., 2022), and macroalgae (Haas & Wild, 2010), to

micrometers within particles such as marine snow, aggregates, and sediments (Alldredge & Cohen, 1987; Anderson & Meadows, 1978; Kühl et al., 1996) encompassing individual marine microorganisms like phytoplankton and zooplankton with different biological metabolisms (Figure 01) (Abe et al., 2004; Elser et al., 1995). Traditional sampling methods that collect large volumes of water tend to average out the microscale microbial activity associated with microenvironments (Bork, 2005; Karsenti et al., 2011), limiting our understanding of their role in the oceans. Recent studies have demonstrated that microbial communities exposed to distinct microenvironments can exhibit variations in microbial activity within the community (Ackermann, 2015; Behrendt et al., 2020), significantly impacting overall biogeochemical processes. This highlights the importance of investigating microenvironments at microbially relevant resolutions to understand their role in microbial activity and controlling biogeochemical cycling.

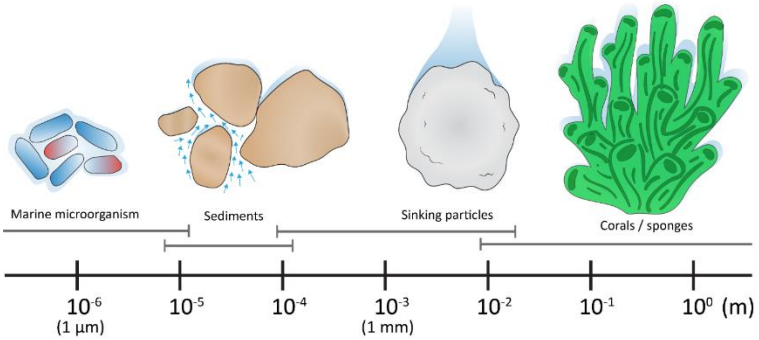

Figure 01: Microenvironments within marine systems of varying size. Microscale variation in marine environments, such as marine organisms, sediments, sinking particles, and corals/sponges displaying the diverse microenvironments influenced by advection, diffusion, and microbial reaction rates. The blue shading represents the diffusion-dominated boundary layer,

defining the concentration gradient, controlling the solute concentrations experienced by the microbial community. (Coral image modified from Freepik)

In the upcoming sections, I will introduce the key characteristics of marine microenvironments, showing how they are formed and maintained by the interplay between the microbial reaction rate and mass transfer, which combined leads to microscale concentration gradients. I will also introduce permeable sandy sediments as a key ecosystem in which microenvironments likely play an important role and discuss the technological limitations which have so far constrained our understanding of microenvironments.

1.1. Transport processes and microbial reactions at the microscale

The activity of microorganisms within a microenvironment can only be sustained if essential solutes such as carbon, oxygen and nutrients are available, and it is the interplay between diffusion, advection and microbial reaction rates that control the concentration of solute within the microenvironment (De Beer et al., 1996; Franklin et al., 2019; Stoodley et al., 1997). Transport of solute (mass transfer) at the microscale (micrometer to millimeter) occurs either by advection or diffusion, where advection is the rapid movement of water and solutes initiated due to pressure gradients and diffusion is the movement of solute along concentration gradients, from high to low (Einstein, 1905). Diffusion is therefore promoted if the microbial community within a microenvironment consumes a solute and elevates the concentration gradient (Stewart et al., 2016). The temporal change in substrate concentration within a microenvironment, considering the combined effects of diffusion, advection, and microbial reaction rates, can mathematically be expressed using the scalar-transport equation:

$$\frac{\partial C}{\partial t} = -\underbrace{\nabla \cdot \vec{J}}_{\substack{\text{Transport} \\ \text{fluxes}}} + \underbrace{R_C}_{\substack{\text{Microbial} \\ \text{reaction rate}}} \qquad \text{(equation 01)}$$

where $\partial C/\partial t$ is the change in concentration of solute (C) over time t, ∇ is the gradient operator, $\vec{J}$ are the areal fluxes which incorporate the diffusive and advective fluxes, and R_C is the microbial reaction rate for the production or consumption of a solute.

Transport fluxes or mass fluxes can be expressed as:

$$\text{Transport fluxes } (\nabla \cdot \vec{J}) = -\underbrace{D\nabla^2 C}_{\text{Diffusion}} + \underbrace{\vec{u} \cdot \nabla C}_{\text{Advection}} \qquad \text{(equation 02)}$$

here D is the diffusion coefficient, C is the concentration of solute, $\vec{u}$ is the velocity vector. A key dimensionless parameter that can be utilized to describe the relative importance of advective transport of solute over the diffusive transport is Peclet number (Pa). It is defined as the ratio of advection rate to diffusion rate as follows:

$$\mathrm{Pe} = \frac{\text{Advection rate}}{\text{Diffusion rate}} \qquad \text{(equation 03)}$$

For most biological systems Pe can be calculated using $(U \cdot L_c) / D$, where U is velocity magnitude, L_c is the characteristic length, D is diffusion coefficient. It becomes apparent that for microorganisms (L_c = O μm, U=O μm/s^{-1}) within microenvironments the Peclet number is much smaller (Pe << 1) than unity which indicates that diffusion dominates over advection, and the mass transfer of solutes is primarily driven by diffusive exchange. However, diffusion is not necessarily independent of advection and the relationship can be exemplified through diffusive boundary layers.

Boundary layers - an interplay of diffusion and advection

All surfaces in marine systems are surrounded by a so-called boundary layer, which forms when water adheres to the surface and when friction reduces the movement of water (Schlichting & Gersten, 2017). The diffusive boundary layer (DBL) acts as a partition between the processes of diffusion and advection. The DBL is a thin layer adjacent to a surface, the size of which is dependent on the flow velocity, the viscosity of water and the diffusion coefficient (Picioreanu et al., 2000). While outside the DBL transport is governed by advection, within the DBL diffusion dominates the transport towards microorganism (Schulz & Zabel, 2006). The relevant diffusive length scale within the DBL is the boundary layer thickness itself which is a function of the flow velocity. Therefore, despite the diffusive transport dominating, the concentration gradient within a DBL is a function of the advection and increased flow may result in diffusive uptake enhancement.

Microbial reaction rate

Solute concentrations within microenvironments are not only a function of transport, but are also intimately linked to the microbial reaction rates (Depetris et al., 2021). Microbial reaction rates pertain to the processes of solute production or consumption through metabolic or transformative activities. For a specific microbial community the microbial reaction rate for a solute is usually presented using Michaelis-Menten kinetics (Michaelis & Menten 1913):

$$\text{Microbial reaction rate } (R_c) = \frac{R_{max} \cdot C}{K_m + C} \qquad \text{(equation 04)}$$

Here Rmax is the maximum metabolic rate, and C is the concentration of solute, Km is the Michaelis-Menten constant and describes when half of the maximal metabolic rate is reached. A microorganism with a low Km exhibits a higher affinity for substrates, enabling effective utilization even at lower concentrations. The high substrate affinity is vital for maintaining minimal concentrations at the cell surface, thereby optimizing solute fluxes. Conversely, microorganisms with higher Km values experience reduced solute fluxes particularly at low concentrations. When studying enzymatic reactions of microorganisms Km values are typically in the range of tens to hundreds of nanomolar (Kovárová-Kova & Egli, 1998).

In the context of organic matter remineralization Berner (1980) & Jörgensen (1978) adapted the Michaelis-Menten kinetic and report apparent-Km values that have much lower affinities (higher Km values) than those expected from enzymatic reactions. This is related to the fact that bulk measurements of apparent-Km values often include solute limitations of the microenvironments in which microorganisms are located and multiple reactions are simultaneously measured (Jörgensen 1978; Boudreau, 1992; Button, 1985). Accurately resolving the chemical conditions within the microenvironments of microorganisms poses

a fundamental challenge and when resolved allows a clear distinction between the enzymatic kinetics and the apparent kinetics under varying environmental conditions.

The mathematical resemblance between Michaelis-Menten kinetics and the growth curves of microorganisms (Monod (1942, 1949)) is noteworthy. Monod's growth kinetics are crucial for understanding the growth of microorganisms under variable solute availabilities. Both, Michaelis-Menten kinetics and Monod growth curves, serve as foundational elements in mathematical modeling approaches used to study mass transfer at microscales (Jannasch & Egli 1993; Koch 1982).

Coupling transport process and microbial reaction rate

In order to assess the solute concentrations within a microenvironment, the degree of coupling between transport rates (mass transfer) and microbial reaction rates must be quantified. A key parameter which assists in this is the Damköhler number (Da), a dimensionless parameter which indicates the dominance in relative timescales of either the microbial reaction rate or the physical transport rate (Damköhler, 1936). The ratio of the timescales for microbial reaction rate and physical transport rate determines the Da as follows:

$$\mathrm{Da} = \frac{\text{Microbial reaction rate}}{\text{Transport rate}} \qquad \text{(equation 05)}$$

Here, microbial reaction rate (C/R_c) is the production or consumption of solute by the microbial community and transport rate is the movement of solute to or from the microenvironment. Transport rate can either be the diffusion (L_c^2 / D, diffusive rate) or advection (L_c / U, advective rate); L_c is the characteristic length, D is diffusion coefficient, and U is velocity magnitude. As the mass transfer in the

microenvironment of microorganisms is governed by diffusion, I will focus on the diffusion Damköhler number.

In a microbial ecosystem where the diffusive rate is higher than the microbial reaction rate (Da > 1) the supply of reactive solute from the vicinity is sufficient to support the microbial reaction (Figure 02). If the microbial reaction rate is higher than the solute supplied then Da <1, this indicates the complete depletion of the supplied solute due to microbial reactions such as respiration. The variability in the solute concentration within the microenvironment, either dominated by the transport process or microbial reaction rate, supports different microbial metabolism mediating different biogeochemical processes.

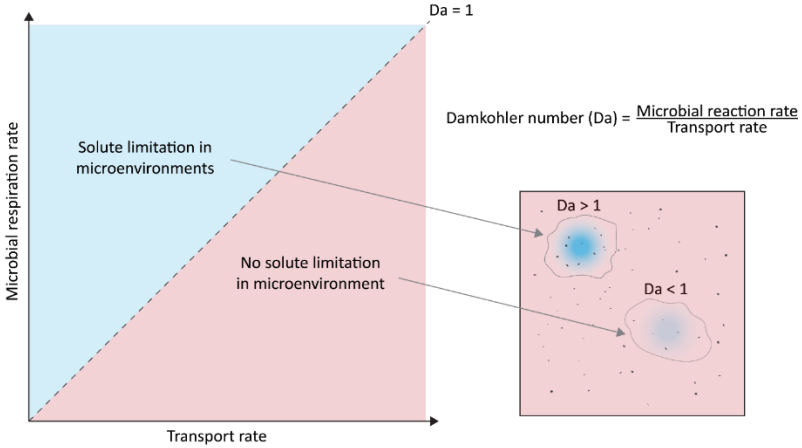

Figure 02: Illustration of the relative dominance of microbial reaction rates over the transport rates in marine ecosystems and vice versa, determined based on Damkoehler number (Da). High microbial reaction rates relative to the transport rate (Da >1, blue) suggests solute limitation within a microenvironment. The transport of solute due to high transport rate exceeding the microbial reaction rate (Da < 1, red) suggested adequate supply of solute to the microenvironment. Right panel represents the conceptual view of a solute limited microenvironment, due to microbial reaction rates (blue) exceeding the transport process.

1.2. Microscale solute availability in microenvironments - oxygen and nitrogen

Marine ecosystems can be broadly classified into oxic and anoxic environments, based on oxygen (O_2) availability. However, O_2 availability can also vary substantially within apparently oxic environments due to microenvironments, which can have a significant impact on the microbial metabolism. O_2 is the highest energy-yield electron acceptor, therefore it is generally the preferred electron acceptor for microorganisms in oxic waters, where it is used during the oxidation of organic (i.e. carbon rich organic matter) or inorganic electron donors to provide energy for growth (Falkowski et al., 2008). After O_2 depletion, organic matter is primarily respired by anaerobic respiration based on the recurrent sequence for the energy-yield from the electron acceptors - nitrate and nitrite, manganese oxides, sulfate and iron oxides (Froelich et al., 1979; Zakem et al., 2020). However, while many microorganisms respire O_2, its low solubility and slow diffusion constrain its availability at the microscale (Berg et al., 2022). The availability and utilization of O_2 at the microscale shapes the formation of distinct microenvironments influencing biogeochemical processes.

Generally it is assumed that the sequence in which electron acceptors are used is defined by the energy-yield associated with them. In nature however, there are an increasing number of exceptions to the utilization of electron acceptors based on energy-yield. For example, studies have revealed the presence of anaerobic metabolisms in well-oxygenated subsurface locations (Foster, 1988; Kuzyakov & Blagodatskaya, 2015; Védère et al., 2022), including simultaneous O_2, nitrate or sulfate respiration in various marine environments (Bourceau et al., 2023; Brandes & Devol, 1995; B. B. Jørgensen, 1977). Such overlap in the consumption of different electron acceptors thereby increases the volumes of marine environments where different electron acceptors can be used. The simultaneous

utilization of the different solutes could be explained due to the presence of microenvironments (Anderson & Meadows, 1978; Tankéré et al., 2002). For example, facultative anaerobic bacteria might switch between aerobic and anaerobic metabolism in apparently oxic waters due to differences in O_2 concentrations within the microenvironment compared to the surrounding water. Alternatively, anoxic microenvironments might host a different microbial community and allow the growth of anaerobic microorganisms that cannot grow in oxic waters. The co-occurrence of various solute utilization and diverse microbial communities could therefore be attributed to the presence of distinct microenvironments.

Nitrogen loss by denitrification

Once O_2 becomes limiting in an environment, nitrogen oxides (nitrate, nitrite, nitric oxide and nitrous oxide) become the favored electron acceptors. Microorganisms can respire these compounds either through anammox (anaerobic ammonium oxidation) or denitrification (Kuypers et al., 2018). Anammox is a microbial process that anaerobically converts ammonium and nitrite into nitrogen gas (N_2) (Strous et al., 1999; van de Graaf et al., 1995). While, denitrification is a stepwise microbial process that reduces nitrate to nitrite, nitric oxide, nitrous oxide, and eventually to N_2, utilizing a series of enzymatic reactions (Zumft, 1997). In contrast to anammox bacteria, all isolated denitrifiers are only facultative anaerobes and can also respire oxygen (Patureau et al., 2000). Although there is evidence that some strictly anaerobic denitrifiers exist, such as the ciliate symbiont (*Candidatus* Azoamicus ciliaticola, Graf et al., 2021) they generally appear to be rare. Therefore microorganisms with the capacity to carry out denitrification can almost always grow under oxic conditions.

Physiological, bioenergetic, and kinetic considerations indicate that denitrification is unlikely to occur in the presence of O_2 (Chen & Strous, 2013).

However, certain studies have shown co-occurring respiration of O_2 and nitrate in certain pure cultures (L. Robertson, 1995; L. A. Robertson & Kuenen, 1984) and oxic marine environments (Gao et al., 2010; Marchant et al., 2017). However, the observation of denitrification under oxic conditions could also be a result of technological limitations, as denitrification might take place in the anoxic microenvironments, surrounded by oxic waters that cannot be spatially differentiated. For example previously reported heterogeneities in subsurface environments were associated with variability in sediment distribution (de Beer et al., 2005; Tankéré et al., 2002), bioturbation/bioirrigation (Bertics & Ziebis, 2009; Meysman et al., 2006) or aggregates/fecal pellets (Bianchi et al., 2018; Ploug et al., 1997; Wolgast et al., 1998). So far however, it has been challenging to study whether similar patches of anoxia exist at microbially relevant scales in the form of microenvironments (see section 1.5).

1.3. Microenvironments in sandy sediments

Marine sediments host diverse microbial communities within a dynamic hydraulic environment. These conditions are particularly dynamic within permeable sandy sediments due to varying advective and diffusive transport of solutes, which creates heterogeneity within the sediment, making sands highly likely to contain microenvironments. By visualizing and understanding microenvironments in sediments, we can gain valuable insights into the functioning and responses of coastal ecosystems to anoxic conditions in the presence of oxygen.

Over the past century, anthropogenic activities have dramatically disrupted nitrogen cycling, resulting in a substantial increase in nitrogen inputs to coastal seas (Chua et al., 2022; Gihring et al., 2010). Microbial communities attached to sandy sediments (Figure 03a), which cover more than 50% of the continental shelves (Emery, 1968), contribute to the removal of anthropogenic nitrogen by denitrification (Marchant et al., 2016; Sokoll et al., 2016). Sandy sediments act as a buffer between the land and open ocean and therefore are important zones for organic matter degradation and anthropogenic nitrogen removal (Huettel et al., 2014; Jørgensen et al., 2022). Despite only occupying 6-8% of the ocean surface (Hall, 2002; Sverdrup et al., 1942), continental shelves are responsible for 20% of marine primary production (Jahnke, 2010). Due to the low organic matter content, sandy sediments were historically considered as biogeochemical deserts (Boudreau et al., 2001). Thus, most studies in the past have focused on muddy sediments, which are rich in organic carbon and characterized with high respiration rates (Canfield, 1993; Jørgensen, 1977). Yet, investigations over the last two decades have shown that the low organic matter content in sands is due to high mineralization rates (de Beer et al., 2005), and matches those recorded in organic-rich muddy sediments (D'Andrea et al., 2002).

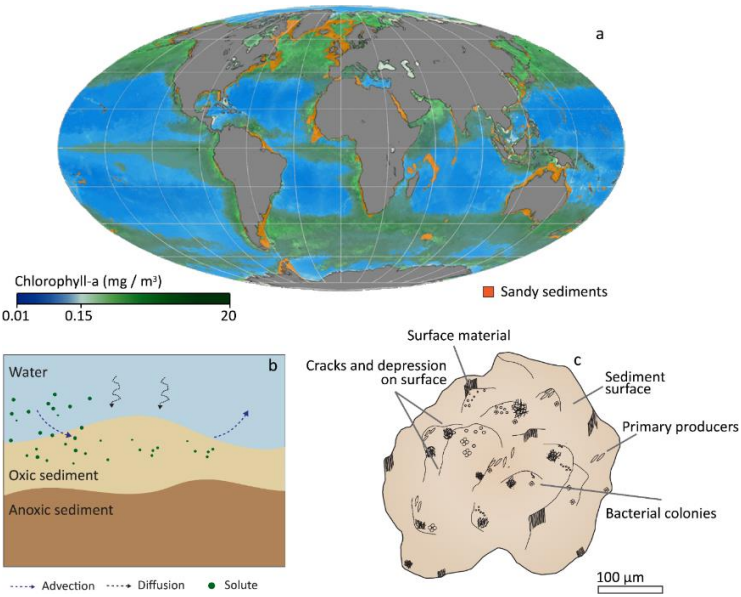

Figure 03: Distribution and characteristics of sandy sediments, highlighting the interplay of transport processes and microbial reactions across scales. a The world-map shows the distribution of sandy sediments (orange) and the chlorophyll concentration (green) indicating the overlap of high productivity within the continental shelves. (Data provided by Emodnet, Naval Office of Oceanography, NASA, map adapted from Ahmerkamp (unpublished)). **b** Transport of solute from the water column to sediments by advective and diffusive processes, resulting in zonation on sediments due to oxygen transport and microbial respiration, typically ranges from centimeter to millimeter (modified from Marchant et al., 2017). **c** Schematic representation of microbial colonization patterns on the sand grain surface, exhibiting localized distribution of microorganisms, surface materials (hatched), and bare surface. Microorganisms demonstrate behavioral preference towards shape irregularities and mineral staining on the sand surface (based on Anderson & Meadows, 1978).

Only a few studies have addressed the potential for microenvironment formation within sands either using experimental approaches (Brandes & Devol, 1995; Jørgensen, 1977) or within modeling studies (R. Jahnke, 1985; Kessler et al., 2014). Previously, the likely presence of distinct microenvironments within sandy sediments has been explained due to diffusion limitation, which has been observed in other systems where it is caused by extensive biofilm growth (Kurz et al., 2022; Stewart & Franklin, 2008), or pore space clogging by aggregates and streamers (Drescher et al., 2013; Lehto et al., 2014). However, research that focuses on the formation of anoxic microenvironments in sands which takes into account pore water movement and solute supply at microbially relevant scales is lacking. By quantifying microbial reaction rates under these conditions and taking microenvironments into account, we can better understand the role of sandy sediments in mediating aerobic and anaerobic processes in biogeochemical cycling.

Transport of solute on sandy sediments

The supply of solutes to sediments is primarily facilitated by transport processes (advection and diffusion) and bioturbation. The high permeability of sandy sediments allows transport of solute by advection, which in muds is limited to only diffusion (Figure 03b) (Thibodeaux & Boyle, 1987). Advective transport due to wind- and density-driven currents affects the movement and distribution of solutes from the water column to the pore space of the sand grains (Glud, 2008; Huettel et al., 2003). While advection primarily occurs due to the flow of water with solutes in the pore space, diffusion enables the supply of solute from the pore space to the microbial community (refer section 1.1). The microscale availability of solute is further enhanced by bioturbation, disturbances due to burrowing organisms (Bertics & Ziebis, 2009; Meysman et al., 2006). The net movement of sediments due to bioturbation creates channels facilitating diffusion of solutes resulting in areas with high and low concentrations in close proximity (Glud et al.,

1994; Revsbech et al., 1980). Diurnal variations in benthic photosynthesis driven by availability of sunlight leads to localized oxygenation of sediments creating spatial heterogeneity in the solute distribution (Jørgensen et al., 2022). Fluctuations in faunal activity and diurnal variations in benthic photosynthesis can lead to microscale patches of highly variable solute concentrations, creating microenvironments (Anderson & Meadows, 1978; Wenzhöfer & Glud, 2004). The combined effects of the transport processes, and faunal activity create a dynamic and interconnected environment that supports the growth and activity of the microbial communities in sandy sediments. Studying such complex transport processes in the laboratory is challenging, and modeling studies can be used to address this.

Modeling studies have become valuable tools to investigate the transport of solutes in sandy sediments, particularly due to the dynamic nature of pore water velocity (Ahmerkamp et al., 2017; Kessler et al., 2013; Molins et al., 2012). These studies typically involve the use of mathematical models that simulate the movement and behavior of solutes from the water column to pore space of the sediments. Studies have demonstrated that distribution and concentration of solutes available to the sediment exhibit even more pronounced variations over micrometer scale (Matyka et al., 2008). This, as well as the biofilm development at the grain level (Bartzke & Huhn, 2015), may result in gradients of O_2 and other dissolved chemicals, resulting in microenvironments with diverse microbial populations on sediments. These studies help to understand the complex interactions between physical processes, such as sediment structure and fluid flow, and biogeochemical processes like microbial activity and nutrient cycling.

Microbial colonization on sediments

Sandy sediments are characterized by highly abundant microbial colonization of 10^8-10^9 cells cm^{-3} (Musat et al., 2006), which is 10^4 times denser than the

microbial population in the water column (Azam et al., 1983). Interestingly, >99% of the benthic microbial community is attached to the sand grains within sandy sediments, with the remaining 1% present in the porewater (Rusch et al., 2006). Nevertheless, microscopic examination has revealed that significant portions of the grain surface remain bare, with the microorganisms and materials that adhere to the surface generally consigned to cracks and depressions (Figure 03c) (Ahmerkamp et al., 2020; Weise & Rheinheimer, 1977). This intermittent colonization, which is the characteristic feature of sandy sediments, can largely be explained by physical forcing during natural abrasion (Carrel et al., 2018; Yawata et al., 2016). In the past, studies have been conducted to study the attached microbial community and their colonization on sediments, but so far the potential formation of distinct microenvironments due to the patchy colonization and varying pore water velocity has not been studied.

Unknown microscale interplay of physical and biological processes

The patchy microbial colonization and heterogeneous microbial reaction rates, combined with varying solute supply, likely play a crucial role in shaping distinct microenvironments on sands. These microenvironments would theoretically exhibit varying solute concentrations compared to their surroundings, resulting in differential O_2 transport and uptake rates, which could facilitate both aerobic and anaerobic processes even when the surrounding pore waters contain O_2. However, due to technological limitations, research has been limited in studying the microscale heterogeneity in microbial reaction rates along with microscale transport processes, thereby hindering the quantification of anoxic microenvironment volumes.

1.4. Measurement and simulation of microenvironments

Microenvironments have been observed to exist within marine environments based on evidence from multiple studies (Stocker, 2012), although quantifying the

volumes of microenvironments presents challenges due to technological constraints. Investigating the properties of micro-scale variations is essential for comprehending the spatial and temporal distribution of these microenvironments. Oxygen, being the most abundant and energetically favorable electron acceptor, serves as a useful proxy for examining variable microbial respiration rates and quantifying oxic-anoxic microenvironments.

Oxygen sensing in microenvironments

A number of approaches have previously been utilized to measure O_2 concentrations in marine environments, such as microelectrodes (Clark et al., 1953), microsensors (Revsbech & Jørgensen, 1986), and optode sensors (Holst et al., 1995; Klimant et al., 1995; Morris et al., 1993). The advent of microsensors and optode sensors allowed for fast and accurate measurements of small-scale O_2 gradients (micrometers) for the first time (Figure 04). Further advancements in the technology mean that microsensors can also be used to detect changes in O_2 at high temporal resolutions (i.e. milliseconds). However, by their nature, microsensors are invasive and hinder or alter the flow field around them, largely restricting their application to static environments. Microsensors offer point measurements, by averaging the O_2 concentrations around the sensor-tip, in sub-micrometers range. Other work has utilized planar optodes (Glud et al., 1996) instead of microsensor point measurements to achieve a two dimensional O_2 measurements (micrometer to millimeter scale), however their spatial and temporal resolution is compromised as O_2 has to diffuse towards the planar optode (Koren & Zieger, 2021). Both techniques rely on diffusion of O_2 towards the sensor and interfere with the flow field, resolving only the diffusive fluxes in equation 02 (section 1.1) and missing out the advective fluxes. Even when utilized in non-static systems, they fail to provide direct measurements and flow information because the microsensor and planar optode act as wall for the flow field. Overall, the limitations associated with current methods of measuring O_2

constrain our comprehensive understanding of how the interplay between transport processes and O_2 respiration in microenvironments control biogeochemical cycling.

One recent advancement that may overcome this limitation is the introduction of sensor particles (Mistlberger et al., 2010). These particles, typically ranging in size from nanometers to micrometers, are embedded with O_2-sensitive dye and measurements are carried out by phosphorescence quenching of the dye (Moßhammer et al., 2019; Quaranta et al., 2012). Sensor particles, embedded with an O_2-sensitive dye that undergoes phosphorescence quenching dependent on the oxygen concentration in the surrounding environment (Koren et al., 2015; Murniati et al., 2016), enable non-invasive oxygen measurements with high spatial resolution (nanometers to micrometers). These particles can be directly coated on the sample surface, facilitating real-time and continuous monitoring of oxygen concentrations directly on the sample surface without relying solely on O_2 diffusion to the sensor. The non-invasive characteristic makes sensor particles well-suited for studying microscale oxygen variations in various environments, including dynamic systems like sediments. Unlike microsensors and planar optodes, sensor particles do not disrupt the flow field, resolving both the diffusive and advective fluxes in equation 02 (section 1.1) providing a more accurate oxygen dynamics at the microscale. They have been successfully employed to non-invasively measure O_2 concentrations in marine environments, such as corals (Koren et al., 2016) and in microorganisms (Kühl et al., 2020; Okkelman et al., 2020). However, while conducting O_2 measurements is feasible, accurately simulating the complex physicochemical conditions present in the environments remains challenging. The integration of microfluidics and modeling approaches alongside O_2 concentration measurements enables a more comprehensive understanding of the interplay of transport processes and microbial reaction rates in biogeochemical cycling.

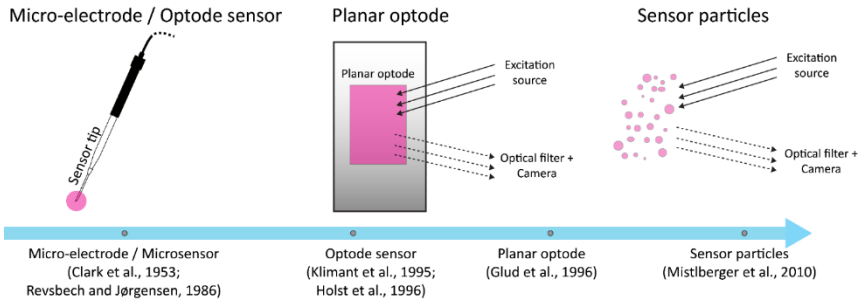

Figure 04: Technological developments in O_2 measurement. Micro-electrode, microsensor and optode sensor measure O_2 concentrations by averaging concentrations around the sensor-tip. Planar optode provides two dimensional information on the O_2 concentrations at micrometer to millimeter scales, while sensor particles offer higher spatial resolution to nanometer scales without hindering the flow field. (Optode sensor image adapted from *unisense.com*)

Microfluidic platforms and numerical models to simulate microenvironments

Microfluidic platforms allow investigation of transport and microbial processes under precisely controlled chemical and flow conditions, providing insights into the dynamic interactions between microorganisms and their vicinity. These platforms offer controlled transport mechanisms; mimicking and regulating the physico-chemical complexity associated with natural environments (Wessel et al., 2013; Zhang et al., 2022; Zhou et al., 2022). Model studies have also aimed to integrate microbial reaction rates with the complex flow conditions experienced by microorganisms in the ocean (Taylor & Stocker, 2012), which otherwise would be difficult to simulate. Microfluidic techniques combined with the model studies have been used to study the cell growth (Aufrecht et al., 2018; Kurz et al., 2022), biofilm distribution in pore space (Ceriotti et al., 2022; Coyte et al., 2017), and cell

response to different solute concentrations (Behrendt et al., 2020; Kasahara et al., 2023) in controlled flow conditions. The integration of microfluidic techniques with O_2 sensor particles holds great potential for studying the microscale O_2 spatial distribution in controlled systems (Li et al., 2019). Studies have employed this approach to study the O_2 concentrations within and around microorganisms (Tobita & Yoshihara, 2016; Zhdanov et al., 2015) in controlled flow conditions. Despite successful demonstrations of microfluidic platforms that expose microorganisms to controlled solute concentrations, there is a significant gap in studying single cells exposed to well-defined multiple solute concentrations. This is crucial for determining the threshold concentrations and affinity values (K_m value, refer section 1.2) of the microbial community for aerobic and anaerobic respiration. Microfluidic techniques can also be integrated with particle image velocimetry (PIV) to get information on the magnitudes and direction of the flow field (Raffel et al., 1998; Westerweel et al., 2013). However, current studies lack the ability to simultaneously study the microbial reaction rates and the transport processes.

The integration of recent advancements in O_2 sensing and microfluidic platforms with model simulations, offers exciting prospects for studying microenvironments in different marine environments. Further technological developments to directly study the spatial respiration and dynamics of O_2 have great potential to unravel the intricate interplay between transport processes and microbial respiration in the microenvironments. Moreover such platforms can further be developed to expose single cells to controlled microenvironments to enhance our understanding of the complex interactions occurring in marine environments at a microscale level.

1.5. Aim and Outline

In marine ecosystems, microenvironments can represent nutrient-rich, sheltered islands but ultimately their impact on biogeochemical cycles is controlled by the interplay between solute supply and microbial metabolism. As a result, the microbial activity within these microenvironments differs from the surrounding areas. Factors influencing the formation of microenvironments, such as transport rate and microbial reaction rate, are still poorly constrained due to technological limitations. Thus, the focus of this thesis was to develop methods to quantify and study the interplay of microscale transport processes and microbial reaction rates which could then be applied to environmental systems, such as sandy sediments. To achieve this, we worked on developing different microscale techniques by combining microfluidics, oxygen-sensitive sensor particles, and imaging techniques with mathematical models.

The main objectives of this thesis were to study i) the interplay of varying flow and variable microbial respiration rate in the formation of anoxic microenvironments on individual sand grains leading to nitrogen-loss in oxic sediments (**Chapter 2**), ii) the effect of solute exchange in transport of solutes to the microbial community residing in the microenvironments (**Chapter 3**), and iii) the behavioral adaptations of the microbial community towards distinct microenvironments (**Chapter 4**). A brief résumé of the research approaches and outcomes reported in **chapter 2-4** are as follows:

Sandy sediments are considered a major sink for anthropogenic nitrogen via denitrification, a process typically restricted to anoxic or low oxygen environments. In **Chapter 2**, we investigated whether anoxic microenvironments form on individual sand grains, allowing denitrification to occur in otherwise oxic sediments. Sandy sediments were collected from sand flats in the North Sea and were coated with oxygen-sensitive sensor particles, using a newly developed

microfluidic device, to study the aerobic respiration rates on individual sand grains. DNA staining was performed and combined with respiration rates to co-relate aerobic respiration with oxygen consuming and producing microorganisms which colonized the sand grains in a patchy manner. Subsequently, a two-dimensional single sand grain model was developed based on the microfluidic results in order to estimate how the interaction of transport processes and microbial respiration controlled the formation of anoxic microenvironments. Further a non-dimensional number was derived which can be integrated into environmental reaction-transport models aimed at estimating N-loss in sandy sediments.

Microbial communities residing in the microenvironments within structured microbial habitats, such as interfaces with surface, biofilms, or sediment, are exposed to different solute concentrations compared to the surrounding waters. To study the transport processes at microscale with high temporal and spatial resolutions (**chapter 3**), we combined latest developments in imaging techniques, with oxygen-sensitive sensor particles, to simultaneously visualize oxygen concentrations and flow fields without hindering the flow. We applied the newly developed method to a model laboratory aggregates and corals investigating the exchange processes in and around the microenvironments.

To study the response of cultured microorganisms to microenvironments with different solute concentrations (**chapter 4)**, we developed a microfluidic device where bacterial cells can be exposed to multiple well-defined gas and solute concentrations. We used sensPIV particles and developed a two-dimensional model to accurately measure and predict the oxygen concentrations and diffusion timescales within the microfluidic chip. *Photobacterium aquimaris*, a marine bacterium, was cultivated in the microfluidic device as a model organism to study the biological responses towards changing oxygen concentrations in

microenvironments. Automated image segmentation was used to track cells to estimate growth rates and morphological changes of the cells.

The results from **chapter 2-4** are discussed in **chapter 5** which explores the relevance and impact of microenvironments in marine systems and suggests future research implications that would advance our understanding for the global biogeochemical cycling.

Bibliography

Abe, S., Okamoto, K., & Madarame, H. (2004). The development of PIV–PSP hybrid system using pressure sensitive particles. *Measurement Science and Technology*, *15*(6), 1153–1157. https://doi.org/10.1088/0957-0233/15/6/016

Ackermann, M. (2015). A functional perspective on phenotypic heterogeneity in microorganisms. *Nature Reviews Microbiology*, *13*(8), 497–508. https://doi.org/10.1038/nrmicro3491

Ahmerkamp, S., Marchant, H. K., Peng, C., Probandt, D., Littmann, S., Kuypers, M. M. M., & Holtappels, M. (2020). The effect of sediment grain properties and porewater flow on microbial abundance and respiration in permeable sediments. *Scientific Reports*, *10*(1), 1–12. https://doi.org/10.1038/s41598-020-60557-7

Ahmerkamp, S., Winter, C., Krämer, K., Beer, D. de, Janssen, F., Friedrich, J., Kuypers, M. M. M., & Holtappels, M. (2017). Regulation of benthic oxygen fluxes in permeable sediments of the coastal ocean. *Limnology and Oceanography*, *62*(5), 1935–1954. https://doi.org/10.1002/lno.10544

Alldredge, A. L., & Cohen, Y. (1987). Can Microscale Chemical Patches Persist in the Sea? Microelectrode Study of Marine Snow, Fecal Pellets. *Science*, *235*(4789), 689–691. https://doi.org/10.1126/science.235.4789.689

Anderson, J. G., & Meadows, P. S. (1978). Microenvironments in marine sediments. *Proceedings of the Royal Society of Edinburgh. Section B. Biological Sciences*, *76*(1–3), 1–16. https://doi.org/10.1017/S0269727000002761

Aufrecht, J. A., Fowlkes, J. D., Bible, A. N., Morrell-Falvey, J., Doktycz, M. J., & Retterer, S. T. (2018). Pore-scale hydrodynamics influence the spatial evolution of bacterial biofilms in a microfluidic porous network. *PLoS ONE*, *14*(6), 1–17. https://doi.org/10.1371/journal.pone.0218316

Azam, F, Fenchel, T., Field, J., Gray, J., Meyer-Reil, L., & Thingstad, F. (1983). The Ecological Role of Water-Column Microbes in the Sea. *Marine Ecology Progress Series*, *10*(13), 257–263. https://doi.org/10.3354/meps010257

Azam, Farooq. (1998). Microbial Control of Oceanic Carbon Flux: The Plot Thickens. *Science*, *280*(5364), 694–696. https://doi.org/10.1126/science.280.5364.694

Azam, Farooq, & Long, R. A. (2001). Sea snow microcosms. *Nature*, *414*(6863), 495–498. https://doi.org/10.1038/35107174

Bartzke, G., & Huhn, K. (2015). A conceptual model of pore-space blockage in mixed sediments using a new numerical approach, with implications for sediment bed stabilization. *Geo-Marine Letters*, *35*(3), 189–202. https://doi.org/10.1007/s00367-015-0399-1

Behrendt, L., Salek, M. M., Trampe, E. L., Fernandez, V. I., Lee, K. S., Kühl, M., & Stocker, R. (2020). PhenoChip: A single-cell phenomic platform for high-throughput photophysiological analyses of microalgae. *Science Advances*, *6*(36). https://doi.org/10.1126/sciadv.abb2754

Berg, J. S., Ahmerkamp, S., Pjevac, P., Hausmann, B., Milucka, J., & Kuypers, M. M. M. (2022). How low can they go? Aerobic respiration by microorganisms under apparent anoxia. *FEMS Microbiology Reviews*, *46*(3), 1–14. https://doi.org/10.1093/femsre/fuac006

Berner, R.A. (1980). A rate model for organic matter decomposition during bacterial sulfate reduction in marine sediments. *In Biogéochimie de la matière organique à l'interface eau-sédiment marin.* C.N.R.S. No. 293, 35-44

Bertics, V. J., & Ziebis, W. (2009). Biodiversity of benthic microbial communities in bioturbated coastal sediments is controlled by geochemical microniches. *ISME Journal*, *3*(11), 1269–1285. https://doi.org/10.1038/ismej.2009.62

Bianchi, D., Weber, T. S., Kiko, R., & Deutsch, C. (2018). Global niche of marine anaerobic metabolisms expanded by particle microenvironments. *Nature Geoscience*, *11*(4), 263–268. https://doi.org/10.1038/s41561-018-0081-0

Bork, P. (2005). Is there biological research beyond Systems Biology? A comparative analysis of terms. *Molecular Systems Biology*, *1*(1). https://doi.org/10.1038/msb4100016

Boudreau, B. P. (1992). A kinetic model for microbic organic-matter decomposition in marine sediments. *FEMS Microbiology Letters*, *102*(1), 1–14. https://doi.org/10.1016/0378-1097(92)90107-Y

Boudreau, B. P., Huettel, M., Forster, S., Jahnke, R. A., McLachlan, A., Middelburg, J. J., Nielsen, P., Sansone, F., Taghon, G., Van Raaphorst, W., Webster, I., Weslawski, J. M., Wiberg, P., & Sundby, B. (2001). Permeable marine sediments: Overturning an old paradigm. *Eos*, *82*(11), 133–136. https://doi.org/10.1029/EO082i011p00133-01

Bourceau, O. M., Ferdelman, T., Lavik, G., Mussmann, M., Kuypers, M. M. M., & Marchant, H. K. (2023). Simultaneous sulfate and nitrate reduction in coastal sediments. *ISME Communications*, *3*(1), 37–40.

https://doi.org/10.1038/s43705-023-00222-y

Brandes, J. A., & Devol, A. H. (1995). Simultaneous nitrate and oxygen respiration in coastal sediments: evidence for discrete diagenesis. *Journal of Marine Research*, *53*(5), 771–797. https://doi.org/10.1357/0022240953213034

Button, D. K. (1985). Kinetics of nutrient-limited transport and microbial growth. *Microbiological Reviews, 49(3),* 270–297

Canfield, D. E. (1993). Organic Matter Oxidation in Marine Sediments. In *Interactions of C, N, P and S Biogeochemical Cycles and Global Change* (Issue Mi, pp. 333–363). Springer Berlin Heidelberg. https://doi.org/10.1007/978-3-642-76064-8_14

Carrel, M., Morales, V. L., Beltran, M. A., Derlon, N., Kaufmann, R., Morgenroth, E., & Holzner, M. (2018). Biofilms in 3D porous media: Delineating the influence of the pore network geometry, flow and mass transfer on biofilm development. *Water Research*, *134*, 280–291. https://doi.org/10.1016/j.watres.2018.01.059

Ceriotti, G., Borisov, S. M., Berg, J. S., & De Anna, P. (2022). Morphology and Size of Bacterial Colonies Control Anoxic Microenvironment Formation in Porous Media. *Environmental Science and Technology*, *56*(23), 17471–17480. https://doi.org/10.1021/acs.est.2c05842

Chen, J., & Strous, M. (2013). Denitrification and aerobic respiration, hybrid electron transport chains and co-evolution. *Biochimica et Biophysica Acta - Bioenergetics*, *1827*(2), 136–144. https://doi.org/10.1016/j.bbabio.2012.10.002

Chua, E. J., Huettel, M., Fennel, K., & Fulweiler, R. W. (2022). A case for addressing the unresolved role of permeable shelf sediments in ocean denitrification. *Limnology And Oceanography Letters*, *7*(1), 11–25. https://doi.org/10.1002/lol2.10218

Chubukov, V., Gerosa, L., Kochanowski, K., & Sauer, U. (2014). Coordination of microbial metabolism. *Nature Reviews Microbiology*, *12*(5), 327–340. https://doi.org/10.1038/nrmicro3238

Clark, L. C., Wolf, R., Granger, D., & Taylor, Z. (1953). Continuous Recording of Blood Oxygen Tensions by Polarography. *Journal of Applied Physiology*, *6*(3), 189–193. https://doi.org/10.1152/jappl.1953.6.3.189

Coyte, K. Z., Tabuteau, H., Gaffney, E. A., Fostera, K. R., & Durham, W. M. (2017). Microbial competition in porous environments can select against rapid biofilm growth. *Proceedings of the National Academy of Sciences of the United States of America*, *114*(2), E161–E170. https://doi.org/10.1073/pnas.1525228113

D'Andrea, A. F., Aller, R. C., & Lopez, G. R. (2002). Organic matter flux and reactivity on a South Carolina sandflat: The impacts of porewater advection and macrobiological structures. *Limnology and Oceanography*, *47*(4), 1056–1070. https://doi.org/10.4319/lo.2002.47.4.1056

Damköhler, G. (1936). Einflüsse der Strömung, Diffusion und des Wärmeüberganges auf die Leistung von Reaktionsöfen.: I. Allgemeine Gesichtspunkte für die Übertragung eines chemischen Prozesses aus dem Kleinen ins Große. *Zeitschrift Für Elektrochemie Und Angewandte Physikalische Chemie*, *42*(12), 846–862. https://doi.org/https://doi.org/10.1002/bbpc.19360421203

De Beer, D., Stoodley, P., & Lewandowski, Z. (1996). Liquid flow and mass transport in heterogeneous biofilms. *Water Research*, *30*(11), 2761–2765. https://doi.org/10.1016/S0043-1354(96)00141-8

de Beer, D., Wenzhöfer, F., Ferdelman, T. G., Boehme, S. E., Huettel, M., van Beusekom, J. E. E., Böttcher, M. E., Musat, N., & Dubilier, N. (2005). Transport and mineralization rates in North Sea sandy intertidal sediments, Sylt-Rømø Basin, Wadden Sea. *Limnology and Oceanography*, *50*(1), 113–127. https://doi.org/10.4319/lo.2005.50.1.0113

Depetris, A., Peter, H., Bordoloi, A. D., Bernard, H., Niayifar, A., Kühl, M., de Anna, P., & Battin, T. J. (2021). Morphogenesis and oxygen dynamics in phototrophic biofilms growing across a gradient of hydraulic conditions. *IScience*, *24*(2), 102067. https://doi.org/10.1016/j.isci.2021.102067

Drescher, K., Shen, Y., Bassler, B. L., & Stone, H. A. (2013). Biofilm streamers cause catastrophic disruption of flow with consequences for environmental and medical systems. *Proceedings of the National Academy of Sciences of the United States of America*, *110*(11), 4345–4350. https://doi.org/10.1073/pnas.1300321110

Ducklow, H. W., Purdie, D. A., Williams, P. J. L. L., & Davies, J. M. (1986). Bacterioplankton: A Sink for Carbon in a Coastal Marine Plankton Community. *Science*, *232*(4752), 865–867. https://doi.org/10.1126/science.232.4752.865

Einstein, A. (1905). Über die von der molekularkinetischen Theorie der Wärme geforderte Bewegung von in ruhenden Flüssigkeiten suspendierten Teilchen. *Annalen Der Physik*, *322*(8), 549–560. https://doi.org/10.1002/andp.19053220806

Elser, J. J., Foster, D. K., & Hecky, R. E. (1995). Effects of zooplankton on sedimentation in pelagic ecosystems: Theory and test in two lakes of the Canadian shield. *Biogeochemistry*, *30*(3), 143–170. https://doi.org/10.1007/BF02186411

Emery, K. O. (1968). Relict sediments on continental shelves of world. *AAPG Bulletin*, *52*(3), 445–464. https://doi.org/https://doi.org/10.1306/5D25C2E7-16C1s-11D7-8645000102C1865D

Falkowski, P. G., Fenchel, T., & Delong, E. F. (2008). The microbial engines that drive earth's biogeochemical cycles. *Science*, *320*(5879), 1034–1039. https://doi.org/10.1126/science.1153213

Fenchel, T. (2002). Microbial Behavior in a Heterogeneous World. *Science*, *296*(5570), 1068–1071. https://doi.org/10.1126/science.1070118

Foster, R. C. (1988). Microenvironments of soil microorganisms. *Biology and Fertility of Soils*, *6*(3), 189–203. https://doi.org/10.1007/BF00260816

Franklin, S., Vasilas, B., & Jin, Y. (2019). More than Meets the Dye: Evaluating Preferential Flow Paths as Microbial Hotspots. *Vadose Zone Journal*, *18*(1), 1–8. https://doi.org/10.2136/vzj2019.03.0024

Froelich, P. N., Klinkhammer, G. P., Bender, M. L., Luedtke, N. A., Heath, G. R., Cullen, D., Dauphin, P., Hammond, D., Hartman, B., & Maynard, V. (1979). Early oxidation of organic matter in pelagic sediments of the eastern equatorial Atlantic: suboxic diagenesis. *Geochimica et Cosmochimica Acta*, *43*(7), 1075–1090. https://doi.org/10.1016/0016-7037(79)90095-4

Gao, H., Schreiber, F., Collins, G., Jensen, M. M., Kostka, J. E., Lavik, G., De Beer, D., Zhou, H. Y., & Kuypers, M. M. M. (2010). Aerobic denitrification in permeable Wadden Sea sediments. *ISME Journal*, *4*(3), 417–426. https://doi.org/10.1038/ismej.2009.127

Gihring, T. M., Lavik, G., Kuypers, M. M. M., & Kostka, J. E. (2010). Direct determination of nitrogen cycling rates and pathways in Arctic fjord sediments (Svalbard, Norway). *Limnology and Oceanography*, *55*(2), 740–752. https://doi.org/10.4319/lo.2009.55.2.0740

Glud, Ronnie N. (2008). Oxygen dynamics of marine sediments. *Marine Biology Research*, *4*(4), 243–289. https://doi.org/10.1080/17451000801888726

Glud, Ronnie Nøhr, Ramsing, N. B., Gundersen, J. K., & Klimant, I. (1996). Planar optrodes: A new tool for fine scale measurements of two- dimensional O2 distribution in benthic communities. *Marine Ecology Progress Series*, *140*(1–3), 217–226. https://doi.org/10.3354/meps140217

Graf, J. S., Schorn, S., Kitzinger, K., Ahmerkamp, S., Woehle, C., Huettel, B., Schubert, C. J., Kuypers, M. M. M., & Milucka, J. (2021). Anaerobic endosymbiont generates energy for ciliate host by denitrification. *Nature*, *591*(7850), 445–450. https://doi.org/10.1038/s41586-021-03297-6

Haas, A. F., & Wild, C. (2010). Composition analysis of organic matter released by cosmopolitan coral reef-associated green algae. *Aquatic Biology*, *10*(2), 131–138. https://doi.org/10.3354/ab00271

Hall, S. J. (2002). The continental shelf benthic ecosystem: Current status, agents for change and future prospects. *Environmental Conservation*, *29*(3), 350–374. https://doi.org/10.1017/S0376892902000243

Holst, G. A., Kuehl, M., & Klimant, I. (1995). <title>Novel measuring system for oxygen micro-optodes based on a phase modulation technique</title>. *Chemical, Biochemical, and Environmental Fiber Sensors VII*, *2508*(September 1995), 387–398. https://doi.org/10.1117/12.221754

Huettel, M., Berg, P., & Kostka, J. E. (2014). Benthic Exchange and Biogeochemical Cycling in Permeable Sediments. *Annual Review of Marine Science*, *6*(1), 23–51. https://doi.org/10.1146/annurev-marine-051413-012706

Huettel, M., Røy, H., Precht, E., & Ehrenhauss, S. (2003). Hydrodynamical impact on biogeochemical processes in aquatic sediments. *Hydrobiologia*, *494*(1–3), 231–236. https://doi.org/10.1023/A:1025426601773

Hutchins, D. A., & Fu, F. (2017). Microorganisms and ocean global change. *Nature Microbiology*, *2*(May). https://doi.org/10.1038/nmicrobiol.2017.58

Jahnke, R. (1985). A model of microenvironments in deep-sea sediments: Formation and effects on porewater profiles. *Limnology and Oceanography*, *30*(5), 966–971. https://doi.org/10.4319/lo.1985.30.5.0956

Jahnke, R. A. (2010). *Global Synthesis*. 597–615. https://doi.org/10.1007/978-3-540-92735-8_16

Jannasch, H. W., & Egli, T. (1993). Microbial growth kinetics: a historical perspective. *Antonie van Leeuwenhoek, 63(3–4),* 213–224

Johnston, C., Martin, B., Fichant, G., Polard, P., & Claverys, J. P. (2014). Bacterial transformation: Distribution, shared mechanisms and divergent control. *Nature Reviews Microbiology*, *12*(3), 181–196. https://doi.org/10.1038/nrmicro3199

Jørgensen, B. B. (1977). Bacterial sulfate reduction within reduced microniches of oxidized marine sediments. *Marine Biology*, *41*(1), 7–17. https://doi.org/10.1007/BF00390576

Jorgensen, B.B. (1978). A comparison of methods for the quantification of bacterial sulfate reduction in coastal marine sediments. II. Calculations from mathematical models. *Geomicrobiol.* J. 1, 29-47

Jørgensen, Bo Barker, Wenzhöfer, F., Egger, M., & Glud, R. N. (2022). Sediment oxygen consumption: Role in the global marine carbon cycle. *Earth-Science Reviews*, *228*(February). https://doi.org/10.1016/j.earscirev.2022.103987

Karsenti, E., Acinas, S. G., Bork, P., Bowler, C., de Vargas, C., Raes, J., Sullivan, M., Arendt, D., Benzoni, F., Claverie, J. M., Follows, M., Gorsky, G., Hingamp, P., Iudicone, D., Jaillon, O., Kandels-Lewis, S., Krzic, U., Not, F., Ogata, H., … Zingone, A. (2011). A holistic approach to marine Eco-systems biology. *PLoS Biology*, *9*(10), 7–11. https://doi.org/10.1371/journal.pbio.1001177

Kasahara, K., Leygeber, M., Seiffarth, J., Ruzaeva, K., Drepper, T., Nöh, K., & Kohlheyer, D. (2023). Enabling oxygen-controlled microfluidic cultures for spatiotemporal microbial single-cell analysis. *Frontiers in Microbiology*, *14*. https://doi.org/10.3389/fmicb.2023.1198170

Kessler, A. J., Cardenas, M. B., Santos, I. R., & Cook, P. L. M. (2014). Enhancement of denitrification in permeable carbonate sediment due to intra-granular porosity: A multi-scale modelling analysis. *Geochimica et Cosmochimica Acta*, *141*, 440–453. https://doi.org/10.1016/j.gca.2014.06.028

Kessler, A. J., Glud, R. N., Cardenas, M. B., & Cook, P. L. M. (2013). Transport zonation limits coupled nitrification-denitrification in permeable

sediments. *Environmental Science and Technology*, *47*(23), 13404–13411. https://doi.org/10.1021/es403318x

Klimant, I., Meyer, V., & Kühl, M. (1995). Fiber-optic oxygen microsensors, a new tool in aquatic biology. *Limnology and Oceanography*, *40*(6), 1159–1165. https://doi.org/10.4319/lo.1995.40.6.1159

Koch, A. L. (1982). Multistep kinetics: Choice of models for the growth of bacteria. *Journal of Theoretical Biology, 98(3)*, 401–417

Koren, K., Brodersen, K. E., Jakobsen, S. L., & Kühl, M. (2015). Optical sensor nanoparticles in artificial sediments-a new tool to visualize O2 dynamics around the rhizome and roots of seagrasses. *Environmental Science and Technology*, *49*(4), 2286–2292. https://doi.org/10.1021/es505734b

Koren, K., Jakobsen, S. L., & Kühl, M. (2016). In-vivo imaging of O2 dynamics on coral surfaces spray-painted with sensor nanoparticles. *Sensors and Actuators B: Chemical*, *237*, 1095–1101. https://doi.org/10.1016/j.snb.2016.05.147

Koren, K., & Zieger, S. E. (2021). Optode Based Chemical Imaging - Possibilities, Challenges, and New Avenues in Multidimensional Optical Sensing. *ACS Sensors*, *6*(5), 1671–1680. https://doi.org/10.1021/acssensors.1c00480

Kovárová-Kovar, K., & Egli, T. (1998). Growth Kinetics of Suspended Microbial Cells: From Single-Substrate-Controlled Growth to Mixed-Substrate Kinetics. *Microbiology and Molecular Biology Reviews, 62(3)*, 646–666.

Kühl, M., Glud, R. N., Ploug, H., & Ramsing, N. B. (1996). Photosynthesis-Coupled Respiration in an. *Journal of Phycology*, *32*, 799–812.

Kühl, M., Trampe, E., Mosshammer, M., Johnson, M., Larkum, A. W., Frigaard, N.-U., & Koren, K. (2020). Substantial near-infrared radiation-driven photosynthesis of chlorophyll f-containing cyanobacteria in a natural habitat. *ELife*, *9*. https://doi.org/10.7554/eLife.50871

Kurz, D. L., Secchi, E., Stocker, R., & Jimenez-Martinez, J. (2022). Morphogenesis of Biofilms in Porous Media and Control on Hydrodynamics. *Environmental Science and Technology*. https://doi.org/10.1021/acs.est.2c08890

Kuypers, M. M. M., Marchant, H. K., & Kartal, B. (2018). The microbial nitrogen-cycling network. *Nature Reviews Microbiology*, *16*(5), 263–276. https://doi.org/10.1038/nrmicro.2018.9

Kuzyakov, Y., & Blagodatskaya, E. (2015). Microbial hotspots and hot moments in soil: Concept & review. *Soil Biology and Biochemistry*, *83*, 184–199. https://doi.org/10.1016/j.soilbio.2015.01.025

Lehto, N., Glud, R. N., á Nordi, G., Zhang, H., & Davison, W. (2014). Anoxic microniches in marine sediments induced by aggregate settlement: Biogeochemical dynamics and implications. *Biogeochemistry*, *119*(1–3), 307–327. https://doi.org/10.1007/s10533-014-9967-0

Li, C., Ding, S., Yang, L., Zhu, Q., Chen, M., Tsang, D. C. W., Cai, G., Feng, C., Wang, Y., & Zhang, C. (2019). Planar optode: A two-dimensional imaging technique for studying spatial-temporal dynamics of solutes in sediment and soil. *Earth-Science Reviews*, *197*(July), 102916. https://doi.org/10.1016/j.earscirev.2019.102916

Marchant, H. K., Ahmerkamp, S., Lavik, G., Tegetmeyer, H. E., Graf, J., Klatt, J. M., Holtappels, M., Walpersdorf, E., & Kuypers, M. M. M. (2017). Denitrifying community in coastal sediments performs aerobic and anaerobic respiration simultaneously. *ISME Journal*, *11*(8), 1799–1812. https://doi.org/10.1038/ismej.2017.51

Marchant, H. K., Holtappels, M., Lavik, G., Ahmerkamp, S., Winter, C., & Kuypers, M. M. M. (2016). Coupled nitrification-denitrification leads to extensive N loss in subtidal permeable sediments. *Limnology and Oceanography*, *61*(3), 1033–1048. https://doi.org/10.1002/lno.10271

Matyka, M., Khalili, A., & Koza, Z. (2008). Tortuosity-porosity relation in porous media flow. *Physical Review E - Statistical, Nonlinear, and Soft Matter Physics*, *78*(2), 1–8. https://doi.org/10.1103/PhysRevE.78.026306

Meysman, F. J. R., Galaktionov, O. S., Gribsholt, B., & Middelburg, J. J. (2006). Bioirrigation in permeable sediments: Advective pore-water transport induced by burrow ventilation. *Limnology and Oceanography*, *51*(1 I), 142–156. https://doi.org/10.4319/lo.2006.51.1.0142

Michaelis, L.; Menten, M.L. (1913). "Die Kinetik der Invertinwirkung". Biochem Z. 49: 333–369.

Mistlberger, G., Koren, K., Scheucher, E., Aigner, D., Borisov, S. M., Zankel, A., Pölt, P., & Klimant, I. (2010). Multifunctional Magnetic Optical Sensor Particles with Tunable Sizes for Monitoring Metabolic Parameters and as a Basis for Nanotherapeutics. *Advanced Functional Materials*, *20*(11), 1842–1851. https://doi.org/10.1002/adfm.201000321

Molins, S., Trebotich, D., Steefel, C. I., & Shen, C. (2012). An investigation of the

effect of pore scale flow on average geochemical reaction rates using direct numerical simulation. *Water Resources Research*, *48*(3), 1–11. https://doi.org/10.1029/2011WR011404

Monod, J. (1942). Recherches sur la croissance des cultures bactériennes. Paris: Hermann & cie.

Monod, J. (1949). The growth of bacterial cultures. Annual Review of Microbiology, 3(1), 371–394. https://doi.org/10.1146/annurev.mi.03.100149.002103

Morris, M. J., Donovan, J. F., Kegelman, J. T., Schwab, S. D., Levy, R. L., & Crites, R. C. (1993). Aerodynamic applications of pressure sensitive paint. *AIAA Journal*, *31*(3), 419–425. https://doi.org/10.2514/3.11346

Moßhammer, M., Brodersen, K. E., Kühl, M., & Koren, K. (2019). Nanoparticle- and microparticle-based luminescence imaging of chemical species and temperature in aquatic systems: a review. *Microchimica Acta*, *186*(2), 126. https://doi.org/10.1007/s00604-018-3202-y

Murniati, E., Gross, D., Herlina, H., Hancke, K., Glud, R. N., & Lorke, A. (2016). Oxygen imaging at the sediment-water interface using lifetime-based laser induced fluorescence (τLIF) of nano-sized particles. *Limnology and Oceanography: Methods*, *14*(8), 506–517. https://doi.org/10.1002/lom3.10108

Musat, N., Werner, U., Knittel, K., Kolb, S., Dodenhof, T., van Beusekom, J. E. E., de Beer, D., Dubilier, N., & Amann, R. (2006). Microbial community structure of sandy intertidal sediments in the North Sea, Sylt-Rømø Basin, Wadden Sea. *Systematic and Applied Microbiology*, *29*(4), 333–348.

https://doi.org/10.1016/j.syapm.2005.12.006

Nøhr Glud, R., Gundersen, J. K., Barker Jørgensen, B., Revsbech, N. P., & Schulz, H. D. (1994). Diffusive and total oxygen uptake of deep-sea sediments in the eastern South Atlantic Ocean:in situ and laboratory measurements. *Deep Sea Research Part I: Oceanographic Research Papers*, *41*(11–12), 1767–1788. https://doi.org/10.1016/0967-0637(94)90072-8

Ochsenkühn, M. A., Schmitt-Kopplin, P., Harir, M., & Amin, S. A. (2018). Coral metabolite gradients affect microbial community structures and act as a disease cue. *Communications Biology*, *1*(1), 184. https://doi.org/10.1038/s42003-018-0189-1

Okkelman, I. A., Neto, N., Papkovsky, D. B., Monaghan, M. G., & Dmitriev, R. I. (2020). A deeper understanding of intestinal organoid metabolism revealed by combining fluorescence lifetime imaging microscopy (FLIM) and extracellular flux analyses. *Redox Biology*, *30*, 101420. https://doi.org/10.1016/j.redox.2019.101420

Pacherres, C. O., Ahmerkamp, S., Koren, K., Richter, C., & Holtappels, M. (2022). Ciliary flows in corals ventilate target areas of high photosynthetic oxygen production. *Current Biology*, *32*(19), 4150-4158.e3. https://doi.org/10.1016/j.cub.2022.07.071

Patureau, D., Zumstein, E., Delgenes, J. P., & Moletta, R. (2000). Aerobic denitrifiers isolated from diverse natural and managed ecosystems. *Microbial Ecology*, *39*(2), 145–152. https://doi.org/10.1007/s002480000009

Picioreanu, C., Van Loosdrecht, M. C. M., & Heijnen, J. J. (2000). A theoretical study

on the effect of surface roughness on mass transport and transformation in biofilms. *Biotechnology and Bioengineering*, *68*(4), 355–369. https://doi.org/10.1002/(SICI)1097-0290(20000520)68:4<355::AID-BIT1>3.0.CO;2-A

Ploug, H., Kühl, M., Buchholz-Cleven, B., & Jørgensen, B. B. (1997). Anoxic aggregates - An ephemeral phenomenon in the pelagic environment? *Aquatic Microbial Ecology*, *13*(3), 285–294. https://doi.org/10.3354/ame013285

Quaranta, M., Borisov, S. M., & Klimant, I. (2012). Indicators for optical oxygen sensors. *Bioanalytical Reviews*, *4*(2–4), 115–157. https://doi.org/10.1007/s12566-012-0032-y

Raffel, M., Willert, C. E., & Kompenhans, J. (1998). Particle Image Velocimetry: A Practical Guide, 2. In *Springer*.

Revsbech, N.P., & Jørgensen, B. B. (1986). Microelectrodes: their use in microbial ecology. In *Advances in Microbial Ecology* (pp. 293–352). https://doi.org/10.1007/978-1-4757-0611-6_5

Revsbech, Niels Peter, Jørgensen, B. B., & Blackburn, T. H. (1980). Oxygen in the Sea Bottom Measured with a Microelectrode. *Science*, *207*(4437), 1355–1356. https://doi.org/10.1126/science.207.4437.1355

Robertson, L. (1995). Confirmation of "aerobic denitrification" in batch cultures, using gas chromatography and 15N mass spectrometry. *FEMS Microbiology Ecology*, *18*(2), 113–119. https://doi.org/10.1016/0168-6496(95)00047-E

Robertson, L. A., & Kuenen, J. G. (1984). Aerobic denitrification — old wine in new bottles? *Antonie van Leeuwenhoek*, *50*(5–6), 525–544. https://doi.org/10.1007/BF02386224

Rusch, A., Huettel, M., Wild, C., & Reimers, C. E. (2006). Benthic oxygen consumption and organic matter turnover in organic-poor, permeable shelf sands. *Aquatic Geochemistry*, *12*(1), 1–19. https://doi.org/10.1007/s10498-005-0784-x

Sar, N., & Rosenberg, E. (1987). *Sar N 1987 Fish skin bacteria.pdf*. 193–202.

Schlichting, H., & Gersten, K. (2017). *Boundary-Layer Theory*. Springer Berlin Heidelberg. https://doi.org/10.1007/978-3-662-52919-5

Schulz, H. D., & Zabel, M. (2006). *Marine Geochemistry* (H. D. Schulz & M. Zabel (eds.)). Springer-Verlag. https://doi.org/10.1007/3-540-32144-6

Seymour, J. R., & Stocker, R. (2018). The ocean's microscale: A microbe's view on the sea. In *Microbial Ecology of the Oceans* (pp. 289–344).

Sokoll, S., Lavik, G., Sommer, S., Goldhammer, T., Kuypers, M. M. M., & Holtappels, M. (2016). Extensive nitrogen loss from permeable sediments off North-West Africa. *Journal of Geophysical Research: Biogeosciences*, *121*(4), 1144–1157. https://doi.org/10.1002/2015JG003298

Stewart, P. S., & Franklin, M. J. (2008). Physiological heterogeneity in biofilms. *Nature Reviews Microbiology*, *6*(3), 199–210. https://doi.org/10.1038/nrmicro1838

Stewart, P. S., Zhang, T., Xu, R., Pitts, B., Walters, M. C., Roe, F., Kikhney, J., & Moter,

A. (2016). Reaction-diffusion theory explains hypoxia and heterogeneous growth within microbial biofilms associated with chronic infections. *Npj Biofilms and Microbiomes*, *2*(April), 1–8. https://doi.org/10.1038/npjbiofilms.2016.12

Stocker, R. (2012). Marine Microbes See a Sea of Gradients. *Science*, *338*(6107), 628–633. https://doi.org/10.1126/science.1208929

Stoodley, P., Yang, S., Lappin-scott, H., & Lewandowski, Z. (1997). Heterogenous Biofilms Using Microelectrodes and Confocal Microscopy. *Biotechnology*.

Strous, M., Kuenen, J. G., & Jetten, M. S. M. (1999). Key Physiology of Anaerobic Ammonium Oxidation. *Applied and Environmental Microbiology*, *65*(7), 3248–3250. https://doi.org/10.1128/AEM.65.7.3248-3250.1999

Sverdrup, H. U., Johnson, W., & Fleming., R. H. (1942). *The oceans: Their physics, chemistry, and general biology* (v. 7). Prentice-Hall.

Tankéré, S. P. C., Bourne, D. G., Muller, F. L. L., & Torsvik, V. (2002). Microenvironments and microbial community structure in sediments. *Environmental Microbiology*, *4*(2), 97–105. https://doi.org/10.1046/j.1462-2920.2002.00274.x

Taylor, J. R., & Stocker, R. (2012). Trade-Offs of Chemotactic Foraging in Turbulent Water. *Science*, *338*(6107), 675–679. https://doi.org/10.1126/science.1219417

Taylor, M. W., Radax, R., Steger, D., & Wagner, M. (2007). Sponge-Associated Microorganisms: Evolution, Ecology, and Biotechnological Potential. *Microbiology and Molecular Biology Reviews*, *71*(2), 295–347.

https://doi.org/10.1128/mmbr.00040-06

Thibodeaux, L. J., & Boyle, J. D. (1987). Bedform-generated convective transport in bottom sediment. *Nature*, *325*(6102), 341–343. https://doi.org/10.1038/325341a0

Tobita, S., & Yoshihara, T. (2016). Intracellular and in vivo oxygen sensing using phosphorescent iridium(III) complexes. *Current Opinion in Chemical Biology*, *33*, 39–45. https://doi.org/10.1016/j.cbpa.2016.05.017

van de Graaf, A. A., Mulder, A., de Bruijn, P., Jetten, M. S. M., Robertson, L. A., & Kuenen, J. G. (1995). Anaerobic oxidation of ammonium is a biologically mediated process. *Applied and Environmental Microbiology*, *61*(4), 1246–1251. https://doi.org/10.1128/aem.61.4.1246-1251.1995

Védère, C., Vieublé Gonod, L., Nunan, N., & Chenu, C. (2022). Opportunities and limits in imaging microorganisms and their activities in soil microhabitats. *Soil Biology and Biochemistry*, *174*, 108807. https://doi.org/10.1016/j.soilbio.2022.108807

Weise, W., & Rheinheimer, G. (1977). Scanning electron microscopy and epifluorescence investigation of bacterial colonization of marine sand sediments. *Microbial Ecology*, *4*(3), 175–188. https://doi.org/10.1007/BF02015075

Wenzhöfer, F., & Glud, R. N. (2004). Small-scale spatial and temporal variability in coastal benthic O 2 dynamics: Effects of fauna activity. *Limnology and Oceanography*, *49*(5), 1471–1481. https://doi.org/10.4319/lo.2004.49.5.1471

Wessel, A. K., Hmelo, L., Parsek, M. R., & Whiteley, M. (2013). Going local: Technologies for exploring bacterial microenvironments. *Nature Reviews Microbiology*, *11*(5), 337–348. https://doi.org/10.1038/nrmicro3010

Westerweel, J., Elsinga, G. E., & Adrian, R. J. (2013). Particle Image Velocimetry for Complex and Turbulent Flows. *Annual Review of Fluid Mechanics*, *45*(1), 409–436. https://doi.org/10.1146/annurev-fluid-120710-101204

Wolgast, D. M., Carlucci, A. F., & Bauer, J. E. (1998). Nitrate respiration associated with detrital aggregates in aerobic bottom waters of the abyssal NE Pacific. *Deep-Sea Research Part II: Topical Studies in Oceanography*, *45*(4–5), 881–892. https://doi.org/10.1016/S0967-0645(98)00006-X

Yawata, Y., Nguyen, J., Stocker, R., & Rusconi, R. (2016). Microfluidic studies of biofilm formation in dynamic environments. *Journal of Bacteriology*, *198*(19), 2589–2595. https://doi.org/10.1128/JB.00118-16

Zakem, E. J., Polz, M. F., & Follows, M. J. (2020). Redox-informed models of global biogeochemical cycles. *Nature Communications*, *11*(1), 1–10. https://doi.org/10.1038/s41467-020-19454-w

Zhang, X., Wu, S., Sun, X., Mortimer, M., Wu, Y., Zhang, M., Huang, Q., & Cai, P. (2022). Zooming in to acquire micro-reaction: Application of microfluidics on soil microbiome. *Soil Ecology Letters*, *4*(3), 213–223. https://doi.org/10.1007/s42832-021-0073-7

Zhdanov, A. V., Golubeva, A. V., Okkelman, I. A., Cryan, J. F., & Papkovsky, D. B. (2015). Imaging of oxygen gradients in giant umbrella cells: an ex vivo PLIM study. *American Journal of Physiology-Cell Physiology*, *309*(7), C501–C509. https://doi.org/10.1152/ajpcell.00121.2015

Zhou, P., He, H., Ma, H., Wang, S., & Hu, S. (2022). A Review of Optical Imaging Technologies for Microfluidics. *Micromachines*, *13*(2). https://doi.org/10.3390/mi13020274

Zumft, W. G. (1997). Cell biology and molecular basis of denitrification. *Microbiology and Molecular Biology Reviews*, *61*(4), 533–616. https://doi.org/10.1128/mmbr.61.4.533-

Chapter 2

Microenvironments on individual sand grains enhance nitrogen loss in coastal sediments

---

Farooq Moin Jalaluddin[1], Soeren Ahmerkamp[1], Hannah K. Marchant[1,2], Volker Meyer[1], Klaus Koren[3], Marcel MM Kuypers[1]

Authors Affiliations

[1] Max Planck Institute for Marine Microbiology, 28359 Bremen, Germany

[2] MARUM – Center for Marine Environmental Sciences, University of Bremen,28359 Bremen, Germany

[3] Aarhus University Centre for Water Technology, Department of Biology, Aarhus University, 8000 Aarhus, Denmark

Corresponding author: Soeren Ahmerkamp (sahmerka@mpi-bremen.de)

Manuscript under review in Proceedings of the National Academy of Sciences of the United States of America (PNAS)

Significance Statement

Anthropogenic activity has dramatically increased nitrogen-inputs to coastal seas. A large amount of this human derived-nitrogen is removed by microbially-mediated denitrification in the sands that blanket the coastlines. Generally, denitrification only occurs when no oxygen is present, however it also seems happen in oxygenated sands, and so far the mechanism is unclear. We used sensor-particles to measure oxygen respiration on individual sand-grains. This revealed that patches of microbes on the sand-grain surface respire so much oxygen that oxygen-free patches develop; therefore denitrification occurs when the surrounding waters contain oxygen. By combining these results with a model we found that 70% of denitrification in oxygenated sands occurs within these anoxic microenvironments. Consequently, these oxygen-free patches are crucial in removing anthropogenic nitrogen-inputs.

Abstract

The permeable sandy sediments which cover more than 50% of the continental shelves are a major, but poorly constrained sink for the vast amount of anthropogenic nitrogen (N) that enters the ocean. Surface-attached microbial communities on sand-grains remove fixed-N via denitrification, a process generally restricted to anoxic or low oxygen (O_2) environments. Yet, in sands, denitrification also occurs in the centimeters thick well-oxygenated surface layer, which leads to additional and substantial N-loss. So far however, the underlying mechanisms that drive oxic denitrification are poorly resolved. In this study, we applied a non-invasive microfluidic technique to observe and quantify how sediment-attached microorganisms shape O_2 availability on the surface of sand-grains. This revealed a remarkable heterogeneity in rates; with patches of O_2 consuming and producing microorganisms situated within micrometers of each other. Two-dimensional multiphysics modelling showed that the high rates of O_2 consumption within the patches on the sand-grain surface outpace O_2 supply from the surrounding pore water. As a result anoxic microenvironments develop on the sand-grain surface, which so far have been invisible to conventional techniques. Our results suggest that ~70% of N-loss previously observed in oxic sandy sediments occurs within these anoxic microenvironments. Our model results indicate that anaerobic denitrification in these anoxic microenvironments can be responsible for ~40% of total N-loss that occurs in silicate shelf sands. Consequently, denitrification in these anoxic microenvironments drives substantial anthropogenic-N removal from continental silicate shelf sands.

Introduction

Permeable sands cover more than half of the continental shelf seafloor where they function as biocatalytic filters (Huettel et al., 2014), removing vast amounts of the anthropogenically derived nitrogen (N) that reaches coastal seas via riverine and groundwater discharge (Chua et al., 2022; Gihring et al., 2010; Marchant et al., 2016; Sokoll et al., 2016). The extensive N-loss that occurs in sands is driven by highly active sediment-attached microorganisms which are constantly re-supplied with substrate (i.e. nitrate and organic matter) due to the advective flow of seawater through the pore space between individual sand grains (Gao et al., 2012; Marchant et al., 2016). These microbial communities remove fixed-N from the environment via denitrification, a process which is typically restricted to anoxic or low oxygen (O_2) environments (Chen & Strous, 2013; Zumft, 1997). Yet, in sands denitrification also seems to occur when O_2 concentrations are high (Gao et al., 2010; Marchant et al., 2017; Rao et al., 2007). This so-called aerobic denitrification has the potential to greatly enhance the volume of sediment in which N-loss can occur, as O_2 can penetrate centimeters deep into sandy sediments dependent on pore water flow velocity (Ahmerkamp et al., 2017; Markus Huettel et al., 2003). Yet, despite the potential importance of aerobic denitrification, so far the underlying mechanisms that drive it are still not understood.

Previously, aerobic denitrification in sandy sediments has been attributed to denitrifying communities performing aerobic and anaerobic respiration at the same time in response to the rapidly changing availability of O_2 (Marchant et al., 2017). Additionally, the presence of anaerobic microbial activity in seemingly oxic environments can be a result of the formation of anoxic microenvironments due to biofilm formation (Aufrecht et al., 2018; Rani et al., 2007). When bacteria colonize surfaces in thick layers (i.e. biofilms), their respiratory activity can lead

to the establishment of O_2 gradients, allowing anaerobic processes to occur even when they are surrounded by well oxygenated waters (de Anna et al., 2021; Franklin et al., 2019; Stewart & Franklin, 2008). This can be exacerbated in soils and sandy sediments, where the pore spaces through which water flows can be clogged by biological processes such as extensive biofilm growth (Kurz et al., 2022), trapping of aggregates (Lehto et al., 2014), streamers (Drescher et al., 2013; Scheidweiler et al., 2019), and tortuosity effects (Matyka et al., 2008). However, microbial colonization on marine sand grains seems to be typically limited to monolayers of microorganisms, which are restricted to cracks and depressions on the sand grain surface (Anderson & Meadows, 1978; Miller, 1989; Probandt et al., 2017). Within these patchy monolayers diffusion-limitation and the formation of anoxic microenvironments were hypothesized to develop (Ahmerkamp et al., 2020) but not reported. This might be a direct consequence of the fact that the techniques frequently applied to study O_2 dynamics in biofilms are unable to resolve O_2 gradients which occur within the diffusive boundary layer (DBL) surrounding single sand grain surfaces. Thus, we have been unable to gain a mechanistic understanding of how sand grain attached microorganisms shape the microenvironment around them and control the potential for anaerobic processes to occur.

Here, we visualized the microbial distribution and volumetric O_2 consumption/production rates on the surface of single sand grains for the first time, using phosphorescent O_2 sensitive nanoparticles. This allowed us to gain new insights into how the activity of sediment-attached microorganisms shapes O_2 availability on the surface of the sand grains. Subsequently, we developed a two-dimensional multiphysics model to show when microbial activity leads to the development of anoxic microenvironments within the DBL of sand grains, even when surrounding pore waters were oxic. By applying a scaling law derived from the model to data obtained previously from coastal sands, we could separate the

relative contribution of aerobic denitrification and denitrification in anoxic microenvironments to N-loss. Our combined results revealed that N-loss in these previously unknown and difficult to resolve microenvironments is an overlooked but substantial sink of nitrogen on the continental shelves.

Results

Patchy co-colonization of sand grain surfaces by phototrophs and heterotrophs

Using fluorescence microscopy and SYBR Green I staining, we visualized and quantified the distribution of DNA containing microorganisms on the surface of single sand grains collected from an intertidal region characterized by high microbial O_2 respiration and N-loss rates. Microscopic imaging of cells revealed a colonization of around $1.3 \cdot 10^8$ cells cm^{-3} ($\pm 0.4 \cdot 10^8$ cells cm^{-3}), which occurred in patches of thin monolayers (Figure 01a and Figure S02). Combined with an estimated sand grain surface area based on the sediment distribution ($0.2 \cdot 10^{-3}$ m^2 cm^{-3} (25^{th} percentile) to $0.5 \cdot 10^{-2}$ m^2 cm^{-3} (75^{th} percentile), with a median $1.5 \cdot 10^{-2}$ m^2 cm^{-3}), this would indicate a characteristic distance between the cells of 10.8 µm. However, as cells were heterogeneously distributed, we found that the cell-cell footprint was actually around 5.1 µm (±1.7 µm).

To distinguish between potential primary producers and other heterotrophic organisms on the sand surface we also imaged the autofluorescence (exc.: 469/35 nm, em.: > 590 nm) from chlorophyll-*a* containing microorganisms, i.e. microphytobenthos (Hense et al., 2008; Lichtenthaler & Buschmann, 2001; Nelson et al., 1999). Correlative imaging with SYBR Green I staining showed that individual sand grains were diversely co-colonized by primary producers and other non-chlorophyll containing organisms, likely heterotrophic organisms (Figure 01; Figure 02b). Overall, cell numbers of primary producers were substantially lower than those of other organisms ($3.5 \cdot 10^6$ cells cm^{-3} compared to

$1.3 \cdot 10^8$ cells cm^{-3}). The morphology of the autofluorescent microorganisms indicated that the primary producers were likely cyanobacteria with typical sizes of <1 µm as well as coccoid and disc-shaped diatoms which were approx. 80 µm large. Taken together the microscopic imaging showed a highly heterogeneous colonization on the surface of individual sand surfaces.

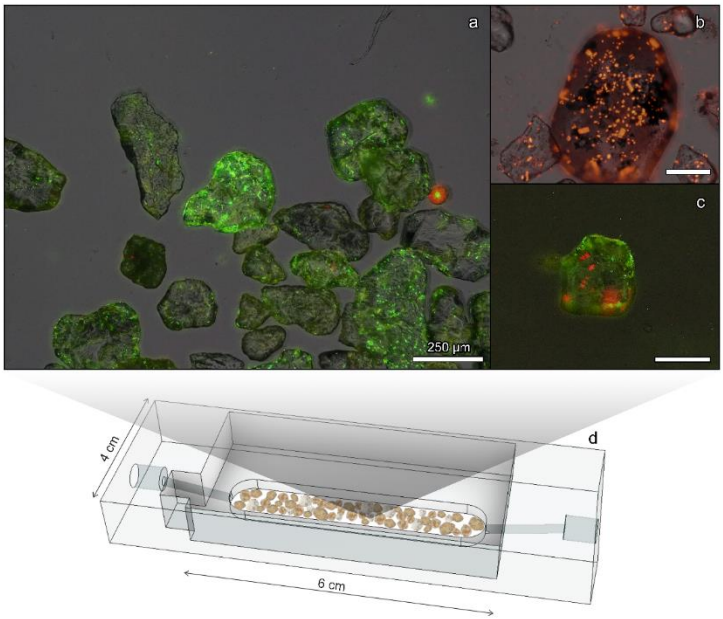

Figure 01. Micrographs indicating the colonization of single sand grains by microorganisms. a dsDNA staining (SYBR Green I, green, exc.:469/35 nm, em.: 510/42 nm) overlaid with RGB image of sand grains reveals the heterogeneous and patchy microbial colonization on individual sand grains, **b** autofluorescence image (red) reveals colonization of microphytobenthos (exc.: ~450 nm, em.: >620 nm), **c** overlay of dsDNA staining (green) and autofluorescence image (red) reveals co-colonization of microphytobenthos and other microorganisms on the sand grains. **d** Conceptual view of the acrylic microfluidic device filled with sand grains to conduct the incubations (see also Figure S01 and S02).

Co-occurring O_2 consumption and production on individual sand grains

To determine the activity of the surface-attached microorganisms (Figure 01a-c), we developed a new microfluidic-based imaging technology (Figure 01 d). Briefly, we coated sand grains with phosphorescent O_2-sensitive nanoparticles and determined volumetric O_2 rate heterogeneities on micrometer scales (1-10 µm) through ratiometric microscopic imaging (see methods for details). Net median volumetric O_2 rates were approx. -20 µmol O_2 L^{-1} h^{-1} but varied strongly from -46 µmol O_2 L^{-1} h^{-1} (25% percentile) to 12 µmol O_2 L^{-1} h^{-1} (75% percentile) (Figure 02d, grey). The imaged map of volumetric O_2 rates therefore showed high heterogeneity with alternating patterns of O_2 consumption and production across the surface of single sand grains. In order to relate the volumetric O_2 consumption and production rates to the microorganisms colonizing the sand grain surfaces, we determined the areas colonized with primary producers through the chlorophyll-a characteristic auto-fluorescence and used this as a mask to extract volumetric O_2 rates associated with the primary producers (Figure 02d, red). In these areas we found net O_2 production rates of 20 µmol O_2 L^{-1} h^{-1} (Figure 02d, red). For the remaining regions we calculated a net O_2 consumption rate of -26 µmol O_2 L^{-1} h^{-1} (Figure 02d, blue) which is larger than the average of the entire rate matrix (-20 µmol O_2 L^{-1} h^{-1}; median-field value). However, both the net consumption and production values represent a conservative estimate as we observed O_2 consumption in some of the masked areas containing primary producers and vice versa, O_2 production in areas containing non-autofluorescent microorganisms. These regions were not abundant and are likely due to the integration of excitation and emission signals from the sand grains due to their 3D structure and reflections.

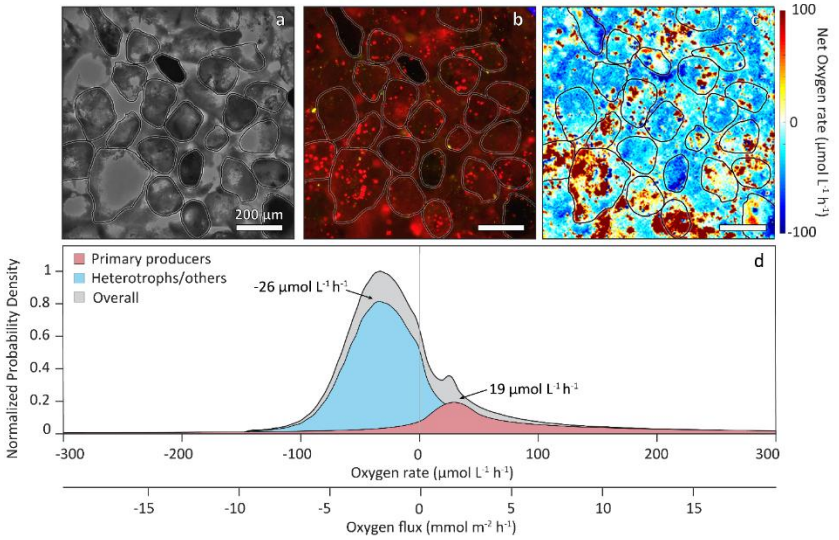

Figure 02. Microbial colonization of sand grain surface leads to co-occurring zones of O_2 production and consumption resulting in highly heterogeneous microenvironments on the sand surface. a Grey-scale image of the sediment sand grains from the incubation, **b** auto-fluorescence image (exc.: ~450 nm, em.: >620 nm) shows abundance of primary producers on sand grains (same field of view as in a), **c** microfluidic incubation reveals O_2 production and consumption occurring simultaneously (blue color indicates O_2 consumption rate and red color indicates O_2 production rate, same field of view as in a and b). **d** Normalized density distribution of the O_2 rate for microenvironments, depicted in grey. The microenvironments are classified based on the presence of primary producers, with net production highlighted in red, and other microenvironments showing net consumption, indicated in blue.

Microenvironments within the diffusive boundary layer of sand grains

To further investigate the role of the intermittent microbial colonization and concurrent O_2 consumption and production on the sand grains, we derived a new single sand grain multiphysics model. The modeled sand grain was populated with a patchy distribution of O_2 consumption and production zones, based on the calculated O_2 fluxes from the microfluidic incubations (Figure 03a, Figure S06). The measured sand surface fluxes ranged between -71 mmol O_2 m^{-2} d^{-1} (25^{th} percentile) and 19 mmol O_2 m^{-2} d^{-1} (75^{th} percentile) and were incorporated into the model through a sinusoidal surface rate distribution with an amplitude (highest rate) of -115 mmol O_2 m^{-2} d^{-1} for O_2 consumption and reduced amplitude of 80 mmol O_2 m^{-2} d^{-1} for O_2 production (ratio ⅓ as inferred from the experimental results). The wavelength of the sinusoidal rate distribution was adjusted to represent the characteristic size (approx. 60 µm) of colonized patches. In a total of 160 model runs we varied bulk O_2 concentrations between 1 to 100 µmol L^{-1} and pore water flow velocities from no-flow to 1000 µm s^{-1}, thereby covering the range typically measured in aquatic environments (Ahmerkamp et al., 2017; Reimers et al., 2004; Savant et al., 1987; Wörman, 1998) (see table S1 for summary of all parameters). The model results showed that O_2 rate heterogeneity along the sand surface propagates into the diffusive boundary layer (DBL) around the sand grain, and then rapidly disappears in the bulk pore water (Figure 03a). The sand grain specific microenvironments caused by microbial activity could extend 40-145 µm into the DBL surrounding the sand grain dependent on pore water velocity.

At low-flow velocities with high bulk O_2 concentrations we observed that respiration rates could outpace the diffusion of O_2 into the boundary layer, leading to the formation of anoxic microenvironments within the sand DBL; despite the close proximity of zones with net O_2 consumption and production. To mechanistically constrain and quantify the formation of anoxic microenvironments, we calculated the total volume of colonized patches which

were potentially anoxic (O_2 concentration < 1 µmol L^{-1}). We observed that 20-100 % of the reactive volumes were anoxic when bulk O_2 concentrations are below 50 µmol L^{-1} or when pore water velocities were lower than 100 µm s^{-1} (Figure 03c), velocities typically found in aquatic environments. Based on these relationships we derived a new non-dimensional number ($Sand_{DBL}$) representing the ratio of diffusive supply through the boundary layer (diffusive time scale) to volumetric rate on the surface (reaction rate, see methods). We found a direct relationship between the $Sand_{DBL}$ number and the volume of anoxic microenvironments that is valid for the entire range of model runs, irrespective of the presence or absence of the primary producers (Figure S07). For $Sand_{DBL}$ < 10 all reactive zones were anoxic and for $Sand_{DBL}$ > 1000 all reactive zones were oxic. In the transition regime we found the best scaling for $Sand_{DBL}$ with the percentage of microenvironments as $1\text{-}1.87 \cdot Sand_{DBL}^{(-0.26)}$. Furthermore, for $Sand_{DBL}$ < 30 best fit was found for $5.0 \cdot 10^{-5} \cdot Sand_{DBL}^{(2.5)}$ and for $Sand_{DBL}$ > 30 best fit was found for $0.18 \cdot Sand_{DBL}^{(0.25)}$. The derived non-dimensional number ($Sand_{DBL}$) includes the effect of varying environmental conditions that can readily be applied to quantify the volume of anoxic microenvironments in sands where anaerobic processes could take place despite O_2 being present in the surrounding pore waters.

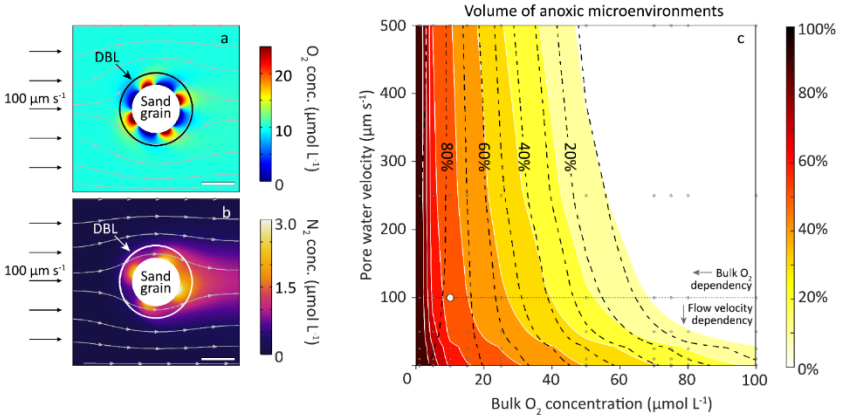

Figure 03. Multiphysics model confirms that the patchy microbial colonization results in heterogeneous microenvironments within the boundary layer of a sand grain. a Patchy distribution of oxygen (O_2) producing and consuming microenvironments within the diffusive boundary layer (DBL) indicate the fast cycling of O_2 on micrometer scales and the formation of anoxic microenvironments on the sand surface, despite the presence of bulk ambient O_2. **b** Even though zones of production and consumption are in direct proximity, anoxic microenvironments are formed in the presence of O_2 resulting in the production of nitrogen (N_2) through denitrification. Streamlines indicate the flow field (scale bar represents 100 µm). **c** Phase diagram indicating the anoxic volume (in which rates are taking place) in dependence to pore water velocities and inflow oxygen concentrations (based on 160 model runs indicated through gray dots, white dot indicates model run depicted in **a+b**). At low flow velocities the anoxic volumes (below 100 µm s^{-1}) are strongly dependent on the flow velocities through which the boundary layer thickness (diffusive length scale) is determined. At high flow velocities (above 100 µm s^{-1}) the anoxic volumes mainly depend on inflow O_2 concentrations, determining the difference of O_2 concentration between the boundary layer and the pore space. Dashed contour lines indicate model results

with O_2 production and O_2 consumption, filled contour lines indicate results with only O_2 consumption.

Nitrogen loss within anoxic microenvironments on single sand gains

We included a denitrification parametrization within the model in order to test the potential denitrification rates that might occur associated with the anoxic portion of the sand grain surface. By assuming a constant ratio of volumetric O_2 consumption rates to denitrification rates (ratio of 0.1 adopted from (Marchant et al., 2017)), we observed substantial N_2 production within the boundary layer (Figure 03b). To gain further insights into how denitrification within anoxic microenvironments might have influenced previous N-loss measurements within bulk oxic sands, we integrated the model results from this study into previously published data on aerobic denitrification (data used from Marchant et al., 2017). The measured O_2 concentrations (Marchant et al., 2017) were used as a chemical boundary condition for the calculation of the SandDBL number to estimate the relative contribution of N_2 production by denitrification from anoxic microenvironments to total N_2 produced. Results revealed simultaneous O_2 consumption and production of N_2 through denitrification under anoxic conditions starting at ambient pore water O_2 concentrations of 80 µmol L^{-1}. Comparison of the experimental data with the scaling-law based modeling, revealed that the N_2 production from the anoxic microenvironments explained 70% of the total N_2 production in the original data (Figure 04a and Figure S08). Further, we integrated the here-derived scaling law with the Elliott & Brooks, (1997) model to calculate the contribution of the N-loss in sandy sediments in the German Bight, concluding an underestimation of ~40% in the N-loss (supplementary information text).

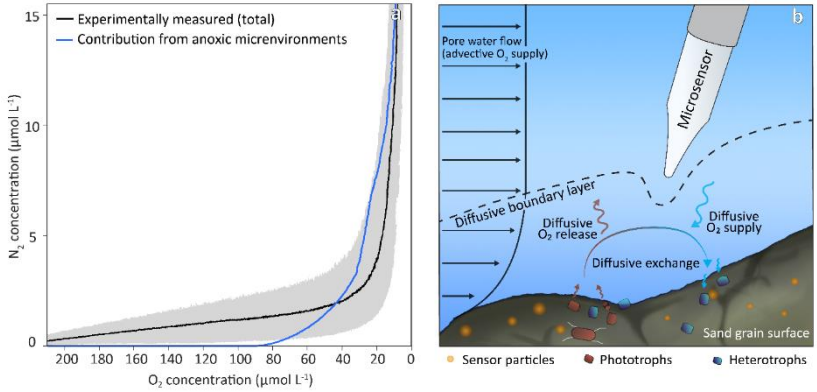

Figure 04. Occurrence of denitrification within anoxic microenvironments within the sand boundary layer when bulk pore waters contain oxygen (O_2). **a** The scaling law derived from the modeling outputs was applied to a previously published dataset (Marchant et al., 2017) where N_2 production was measured simultaneously to oxygen respiration in sandy sediments (mean concentration as solid line and gray shaded area represents the concentration range from different experiments). This allowed an estimation of the proportion of sand grain surfaces which were anoxic for the given oxygen concentration; subsequently N_2 production was calculated within these microenvironments based on the maximal anoxic rate of denitrification measured in the same incubation (blue solid line). Anoxic microenvironments started accumulating within the sediment even when bulk pore water still had an O_2 concentration of 80 µmol L^{-1}. The remaining N_2 production could not be attributed to anoxic microenvironments and was likely produced in the presence of oxygen (data used can be found in Figure S08). **b** Reduction of porewater velocity around sand grains leads to a limited supply of substrate due to the formation of a diffusive boundary layer (DBL). When microbial respiration rates within the boundary layer exceed diffusion of O_2 into the DBL, local spots of anoxia can form, even when oxygen is produced nearby by

oxygen producing microorganisms. Conventional techniques such as micro-sensors would not be able to resolve these micrometer scale patches of anoxia as they disrupt the DBL which leads to mixing between the anoxic and oxic microenvironments as well as the surrounding waters.

Discussion

By applying a newly developed microfluidic-based imaging technology we were able to observe oxygen (O_2) dynamics on individual sand grains for the first time; thereby gaining new insights into the chemical environments encountered by the microorganisms which colonize them. The sand grains were collected from an intertidal flat in a region which is characterized by high net O_2 respiration (e.g. de Beer et al., 2005). In line with this, we observed a similar net O_2 consumption as previous studies (~26 μmol L^{-1} h^{-1}; Gao et al., 2012; Polerecky et al., 2005). However, our analysis showed that there was a remarkable heterogeneity in respiration and photosynthesis rates at the single sand grain level; revealing a mosaic of O_2 consuming and producing patches situated within micrometers of each other on the sand grain surface (Figure 02c). The patches of O_2 consumption and production directly correlated to areas colonized by non-phototrophic O_2-consuming and phototrophic O_2-producing microorganisms, respectively (Figure 02d). Both these functional groups of microorganisms are known to colonize sand grains (Kuriyama et al., 2021; Paterson D. M., 1995; Zetsche et al., 2011), however their ability to noticeably affect O_2 gradients over such small scales has not been reported before.

Although our visualization revealed that microorganisms tended to colonize the sand grain surface in patches, they also showed that microorganisms did not form 3D-structured thick biofilms, which can lead to diffusion limitation (Ceriotti et al., 2022; Costerton et al., 1994; de Beer et al., 1994; Stewart, 2003), pore-space

clogging (Aufrecht et al., 2018; Coyte et al., 2017) and the formation of large anoxic microniches. However, the high local rates of O_2 consumption that we observed using O_2-sensitive nanoparticles indicated that there was the potential for anoxia to occur on the sand grain surface, despite ventilation of the surrounding pore space due to porewater flow. Until now, these anoxic "microenvironments" had not been observed, because they are too small to resolve using more conventional instruments like microsensors (Revsbech & Jørgensen, 1986), which also disturb any potential diffusive boundary layer around sand grains (Ahmerkamp et al., 2022; Glud et al., 1994). Therefore to investigate the mechanisms and controlling factors which would lead to the formation of the observed oxic and anoxic patches on the sand grain surfaces under realistic conditions of pore water flow (thereby allowing the co-occurrence of aerobic and anaerobic microbial metabolisms), we derived a multiphysics model consisting of a single spherical sand grain with a patchy distribution of O_2 consumption and production.

The model results revealed that the diffusive boundary layer (DBL) around individual sand grains had O_2 concentrations which differed greatly from the surrounding pore waters (Figure 03a), even when the pore waters were extremely well ventilated (i.e at pore water velocities of 1000 μm s^{-1}). Within the boundary layer, the high rates of microbially driven O_2 consumption and production outpaced the diffusion limited mass transport of O_2 from the surrounding water. This resulted in a visible propagation of microbially driven changes in O_2 concentrations into the DBL (40-145 μm thick). However, this signal rapidly disappeared in the surrounding pore water, and consequently would be hidden from the conventional techniques used to determine the chemical environment within sands (Figure 04b). Importantly, the model also revealed that fully anoxic microenvironments could form within the DBL, even when the patches of O_2 consumption were in close proximity to patches of net O_2 production. Therefore, we show an entirely new mechanism by which aerobic and anaerobic microbial

metabolisms can occur simultaneously on the surface of single sand grains in the environment. A major implication of these findings is that anaerobic microbial activity within these previously unseen anoxic microenvironments could be a significant driver of N-loss via denitrification within the "oxic" zone of sandy sediments (Figure 03b).

Previously, the occurrence of aerobic denitrification in oxic sands collected from the same region as this study was fully attributed to microorganisms simultaneously respiring oxygen and nitrate (Marchant et al., 2017). To investigate whether anoxic microenvironments on single sand grain surfaces could explain the observed aerobic denitrification rates, we reassessed the experimental data in Marchant et al., (2017), applying a scaling law derived from our modeling outputs. This allowed us to determine when microbially driven O_2 consumption rates outpaced the transport of O_2 into the DBL surrounding individual sand grains, revealing that anoxic microenvironments would have started to form at ambient pore water O_2 concentrations of ~80 μmol L^{-1} (Figure 04a). Thus, denitrification in anoxic microenvironments on single sand grains cannot explain the observed aerobic denitrification occurring at higher O_2 concentrations. It is likely that this aerobic denitrification results from microorganisms respiring O_2 and nitrate at the same time as suggested previously (Marchant et al., 2017). The modelled onset of N_2 production within anoxic microenvironments at ~80 μmol O_2 L^{-1} did however, correspond with the experimentally determined exponential increase in N_2 production, indicating that this increase could result from microenvironments on individual sand grains. Furthermore, we found that the abundance of anoxic microenvironments increased with decreasing ambient pore water O_2 concentrations to such an extent that ~70% of N-loss in oxic sands, previously attributed to aerobic denitrification, could instead be attributed to denitrification in anoxic microenvironments on individual sand grains.

Most current transport-reaction models used to estimate areal N-loss from the sandy shelves do not include any N-loss in the oxic part of the sediment (Ahmerkamp et al., 2017; Cardenas et al., 2008; Sokoll et al., 2016) or only include aerobic denitrification resulting from microorganisms respiring O_2 and nitrate simultaneously (Marchant et al., 2016). Our results show that denitrification within anoxic microenvironments on sand grain surfaces has the clear potential to increase the magnitude of N-loss from the sandy continental shelves, where advection drives oxic seawater centimeters deep into the pore space (Ahmerkamp et al., 2017; Huettel & Gust, 1992; Precht & Huettel, 2004). To assess the role that anoxic microenvironment on individual sand grains play, we integrated the scaling law into a previously developed transport-reaction model used to upscale volumetric rates in the German Bight to areal fluxes of N-loss (Marchant et al., (2016), see methods). We found that total N-loss from oxic and anoxic sediments in the German Bight was consistently underestimated by ~40%, indicating that the sandy sediments of the German Bight are an even more important filter for the anthropogenic N-inputs to coastal North-West Europe than previously thought.

The discovery of anoxic microenvironments on the surface of individual sand grains reveals a heretofore-unknown mechanism that allows anaerobic microbial activity to occur in environments where O_2 is rapidly replenished by advective pore water flow. Furthermore, the close proximity of oxic and anoxic microenvironments on the surface of sand grains likely plays a role in the strong coupling of nitrification and denitrification in these environments (Marchant et al., 2016), as well as enhancing spatial overlaps between other processes such as nitrate and sulfate reduction (Bourceau et al., 2023) and influencing the mobilization and redistribution of iron and manganese-oxides (de Beer et al., 2005; Keiluweit et al., 2018; Védère et al., 2022). Taken together, our results show that patches of anoxia on single sand grain surfaces, invisible to conventional techniques are significant zones of N-loss via denitrification within oxic sandy

sediments. Consequently, they expand the volume of sediment in which N-loss can occur and are therefore a crucial factor in the removal of anthropogenic N-inputs on the sandy continental shelves.

Materials and Methods

Sample Collection

Sediment samples and sea water for the incubations were collected from an intertidal flat in Dorum, North Sea (53.64° N, 8.49° E) in January 2021. A spatula was used to collect the benthic surface sediment (top 1 cm), collected in a pre-washed plastic transport box, and transferred to the lab in Bremen in a cool box. Sediment was stored immersed in sea water in the dark at 12°C on a shaker and sub-samples were collected for the incubations.

Microbial Colonization and cell counting on sand grains

The collected sediments were prepared for SybrGreen I staining by diluting 10,000x concentrate DMSO to 1x final concentration. 0.1 ml of 1x SybrGreen I was added to a 0.2 ml of an Eppendorf cup with sediment and left in the dark for 15 minutes. The sediment was washed with phosphate-buffered saline (PBS) twice and stored at -25°C until used for microscopy. SybrGreen I stains all the microorganisms containing dsDNA (double-stranded DNA) and is used to visualize the colonization of microorganisms on the sand grain surface. Primary producers were distinguished from other organisms based on the chlorophyll-a auto-fluorescence (Franqueira et al., 2000; Greg Mitchell & Kiefer, 1988). Staining and fluorescence z-stack images were further used for cell counting and to determine cell-cell distance on the sand surface (in total 50 sand grains). Regions of interest (ROI) were chosen randomly on the sand grain surfaces for counting the number of cells and cell-cell distance. The closest neighbor cell colony was used for cell-cell distance excluding overlapping cells as it was not possible to visually distinguish them.

Volumetric O_2 consumption rate estimates using sensor particles

An acrylic microfluidic chip was designed to coat sand grains with sensor particles and perform incubations (chamber dimensions 35x7.8x2mm, Figure 01d). A thin

layer (~600 µm) of sand was gently spread out in the chamber of the microfluidic chip using a sterile lab spatula and 1 ml of the prepared sensor particle solution was injected on the sand in the chip from the top using a syringe. The added solution was slowly removed from the chip through 1 ml syringes attached at the outlets. This procedure was repeated three times resulting in a homogenous coating of the sediments with sensor particles, keeping the pore space free from sensor particles. The density of sensor particles was estimated from scanning electron micrographs (Figure S04a-b). Additionally, lifetime imaging using a pco.1600 camera attached to a custom-made modulator was used to capture lifetime images from the sensor particles, in order to confirm the distribution of the sensor particles (Figure S04c-d). Subsequently, the outlets were sealed and the chip was filled with filtered (0.2 µm) seawater. The top of the microfluidic chip was covered using a glass coverslip and images were captured through the bottom glass (supplementary information text for more details).

The prepared microfluidic chip was mounted on an inverted microscope (Leica DMI 6000B) with a sCMOS camera attached (pco.panda 4.2) and images were recorded and stored using pco.camware 4.11 software with a camera exposure of ~200 ms. An LED light source (Omicron LedHUB® – High-Power LED Light Engine) with a wavelength of 455 nm and output power 2400 mW was used for excitation and a polyester filter (Lee filter-101 Yellow; emi.: >535 nm) was attached to the camera for recording emissions from the sensor particles. RGB images for the ratiometric imaging were captured at a resolution of 2048 x 2048 pixels and all post-processing was carried out using Matlab (R2019a, Mathworks). For processing the images, a threshold was set to remove outliers, and data was smoothed using the medfilt2 function with a 5x5 kernel.

A ratiometric imaging approach was used to estimate the O_2 concentration in the acquired RGB images. For each time point 10 images were captured and averaged,

the raw images were split into red and green channels and the ratio was calculated:

$$Ratio = \frac{Red\ channel\ (indicator\ dye)}{Green\ channel\ (reference\ dye)} \qquad \text{(equation 01)}$$

The O_2 production and consumption rates from the microfluidic incubation were calculated by estimating the pixel wise differences of O_2 concentrations at two time points in the chip, divided by the incubation time:

$$R = \frac{C_{t1} - C_{t0}}{t} \qquad \text{(equation 02)}$$

R is the O_2 rate (µmol O_2 L^{-1} h^{-1}), C_{t1} is concentration of O_2 (µmol L^{-1}) at time t_1, C_{t0} is initial concentration of O_2 (µmol O_2 L^{-1}) at time t_0, t is incubation time in hours (t_1 - t_0). Incubation was run for approx. 300 minutes (until anoxic) with capturing images every 20 minutes. In the approach we assume that at t_0, the oxygen concentration is homogeneously distributed around the sand grain.

O_2 rates were masked through thresholding based on the chlorophyll-a auto-fluorescence. This allows linking rates with spatial colonization of the primary producers and other organisms. For O_2 production rates, the median consumption rate was subtracted (-20 µmol O_2 L^{-1} h^{-1}) to calculate the gross O_2 production rate. For plotting the distribution of O_2 rates (production and consumption) against the normalized density, the masked rates were divided by the sum of the O_2 rates. Volumetric rates were converted to fluxes by multiplying with the surface-to-volume ratio of the sand grains.

Modeling single sand grains and the formation of microenvironments

To investigate the effect of the patchy microbial colonization on a single sand grain under varying environmental conditions, we developed a two-dimensional

multiphysics model (Comsol multiphysics 5.6). The model domain consists of circular sand grain with a reactive domain (5 µm thin) on the sand surface (Figure S06). The flow field is calculated by solving the laminar Stokes equations:

$$0 = -\nabla p + \mu \nabla^2 \boldsymbol{u} \qquad \text{(equation 03)}$$

$$\nabla \cdot \boldsymbol{u} = 0 \qquad \text{(equation 04)}$$

u is the velocity vector, p the pressure, µ dynamic viscosity ($1.22 \cdot 10^{-3}$ Pa·s; (Kessler et al., 2014)) and ∇ the gradient-operator .

The oxygen (O_2) and di-nitrogen (N_2) distribution was calculated by solving the stationary advection-diffusion equations:

$$0 = D\,\nabla^2 C_{O2,N2} - \boldsymbol{u} \cdot \nabla C_{O2,N2} - R \qquad \text{(equation 05)}$$

D is diffusion coefficient ($1.1 \cdot 10^{-9}$ m^2 s^{-1} for O_2, and $2.1 \cdot 10^{-9}$ m^2 s^{-1} for N_2 at 25°C corrected for EPS in the colonization patches (Stewart, 2003)), ∇ the gradient-operator, C is concentration of O_2 and N_2, **u** is the velocity vector, R_c is reaction rate taking place in a 5 µm thin layer along the surface. No-flux, slip boundary conditions were applied at the top, and bottom boundaries and no-slip boundary conditions on the sand grain boundary (see Figure S06). Inlet and outlet boundaries as inflow and outflow for the assigned pore water flow. For R_c, we derived a sinusoidal function along the surface of the sand grain to produce alternating patterns of production and consumption:

$$R_{c=}\left(R_{O2,N2}\right) \cdot (\sin(\operatorname{atan}\left(\frac{y}{x}\right) \cdot a)) \cdot f_{O2,N2}(\mathrm{C}) \qquad \text{(equation 06)}$$

Where *y* and *x* are the spatial coordinates, *a* is the amount of patches along the surface. $f_{O2}(C)$ and $f_{N2}(C)$ are concentration dependent functions, where we

applied a Michaelis-Menten kinetic for O_2, $f_{O2}(C) = C_{O2}/(K_m+C_{O2})$, with C_{O2} is the concentration of O_2, K_m is the half-saturation coefficient of O_2 (K_m= 0.1 µmol L^{-1}). For N_2, we applied a O_2 dependent inhibition term $f_{N2}(C) = C_{inh}/(C_{inh}+C_{O2})$, where C_{inh} = 0.1 µmol L^{-1}. The magnitude of the rate was adjusted to 955 mol m^{-3} h^{-1} representing a single-cell rate of 0.06 fmol $cell^{-1}$ h^{-1} (Ahmerkamp et al., 2020). The production of N_2 was estimated using a relationship based on ^{15}N labeled isotope incubations for O_2 consumption and N_2 production (Marchant et al., 2017). Production of N_2 was proportional to the volumetric O_2 consumption rate with inhibition constant of N_2 at 0.1 µmol L^{-1} (Chen & Strous, 2013; Evrard et al., 2013).

In order to rationalize the complex interaction of flow and diffusive exchange in the boundary layer of the sand grain, we derived a non-dimensional number. First, the diffusive boundary layer thickness δ around a single sand grain was estimated by applying a previously derived scaling law (Kiørboe, 2001; Ploug et al., 2002):

$$\delta = \frac{r}{Sh} \qquad \text{(equation 07)}$$

where r is median radius of the sediments, Sh is Sherwood number Sh, $1 + 0.62 \cdot Re^{0.41} Sc^{0.33}$, Re is Reynolds number Re = U r / ν, U is pore water velocity, ν is kinetic viscosity, Sc is Schmidt number Sc = ν / D, D is diffusion coefficient of O_2 in water. The $Sand_{DBL}$ number (analog to the Damköhler number) is then calculated by estimating the diffusive time scale to reaction time scale:

$$Sand_{DBL} = \frac{\delta}{D} \cdot \frac{R\_O2}{C\_0} \qquad \text{(equation 08)}$$

where R_O2 is reaction rate, C_0 is bulk O_2 concentrations.

Acknowledgments

We thank D. Tienken, G. Klockgether, S. Littmann, P. Färber, O. Artmann, and F. Schramm for technical assistance; T. Ferdelman and M. Holtappels for sample logistics; G.Lavik, A. Chennu, J. Milucka, J. von Arx, A. Kidane and F. Lange for fruitful discussions. H.K.M. and F.M.J. received funding from the DFG under Germany's Excellence Strategy (no. EXC-2077-390741603). S.H.A. and K.K. acknowledge funding by Novo Nordisk Fonden. The research was funded by the Max Planck Society.

Supplementary Methods

Sybr Green Imaging

Standard glass slides were customized by creating a frame using Scotch tape (10x10 mm) and sandy sediment was added. Fluorescence microscopes (Olympus microscope BX53 and Zeiss Axio IMager M2) were used for capturing images from the green fluorescence of stained dsDNA (filter-cube GFP; exc.: 469/35 nm, em.: 510/42 nm) and the chlorophyll-a auto-fluorescence (filter-cube N2.1; exc.: 469/35 nm, em.: > 620 nm).

Sensor Particle Fabrication

Sensor particles were prepared by precipitation as described earlier (Ahmerkamp et al., 2022; Koren et al., 2015, 2016; Mistlberger et al., 2010). The sensor particles consist of two dyes, namely, platinum(II)-5,10,15,20-tetrakis-(2,3,4,5,6-penta-fluorophenyl)-porphyrin (PtTFPP; exci.: ~400 nm or ~540 nm, em.: ~650 nm) and macrolex fluorescent yellow 10GN (MY; exc.: ~450 nm, em.: ~480 nm). The former is an oxygen (O_2) dependent dye and the latter is a reference dye to compensate for bleaching of sensor particles and inhomogeneities of the sensor-particle distribution (Li et al., 2019; Moßhammer et al., 2019). The stock solution of sensor particles was centrifuged for two minutes (Eppendorf centrifuge 5430R) and the supernatant was replaced with collected seawater, this was repeated three times.

For calibration, the sensor particle solution was filled in a 6 ml Exetainer and O_2 concentration in the solution was controlled by degassing with N_2 gas and air (21% O_2). The O_2 concentration was monitored using needle optodes (Pyroscience). Correlation between the ratiometric signal and O_2 concentrations was established using the curve fitting tool in Matlab (calibration slope is shown in Figure S05).

Sediment characterisation

To determine the grain size distribution, we recorded multiple images of the collected sand grains (n ~ 400, Figure S3). The images were processed in Matlab (R2019a, Mathworks) to determine diameters (d_g, Figure S3). The porosity (θ, ratio of void volume and total volume) was estimated, by preparing 10 ml of water saturated sediment, which was left overnight in the oven to dry (Evrard et al., 2013; Fraser, 1935). From the weight difference the void volume was used to calculate the porosity of 0.4. The surface to volume ratio ($S_{V,T}$) of the sediments was then calculated based on the measured grain size distribution using:

$$S_{V,T} = 6(1 - \theta) \int_{d_0}^{d_1} \frac{p(d_g)}{d_g} dd_g \qquad \text{(equation 09)}$$

where $p(d_g)$ is the probability density function of the respective sediment fractions and d_g the diameter of the grains.

Areal denitrification estimates

We applied an empirical transport model after Elliott & Brooks, (1997) (and validated through Ahmerkamp et al., (2017) for North Sea sediments) to estimate the contribution of denitrification within microenvironments to total denitrification based on field-obtained data by Marchant et al., (2016). The model allows to calculate an effective mixing depth *D* in sandy sediments as a function of time *t*:

$$D = \frac{1}{k \ln(\frac{0.42\, k^2 K\, h_m t}{\theta} + 1)} \qquad \text{(equation 10)}$$

Where h_m is the hydraulic head (m), θ the porosity, k the wavenumber λ/(2*pi), λ the characteristic bedform size, K is the hydraulic conductivity (m s^{-1}). First, we calculated the time until oxygen and nitrate are depleted by considering water column concentrations and measured volumetric reaction rates. These two characteristic timescales are used in equation 10 to calculate oxygen and nitrate penetration depths. When integrating volumetric denitrification rates over the resulting nitrate penetration depths, areal denitrification rates can be estimated to range between 1 and 1.8 mmol m^{-2} d^{-1} (for details see also Marchant et al., 2016).

In order to estimate the contribution of microenvironments to areal denitrification, we calculated the $Sand_{DBL}$ number based on equation 08 (in main text). To determine the characteristic pore water velocity we followed the (Elliott & Brooks, 1997) approach: $U = k \cdot K \cdot h_m$. Within sands the bulk oxygen concentration depletes with depth and to take the changing oxygen concentrations into account, we mathematically split the oxic sediment into four layers. We then calculated the oxygen concentration for each of these layers and estimated the $Sand_{DBL}$ number to range between 160 and 5013 which implies that on average between 50-80 % of reactive volumes in bulk oxic sands are anoxic. When assuming that anaerobic denitrification takes place in these anoxic volumes the contribution to total denitrification is between 36-43 %.

Supplementary Figure

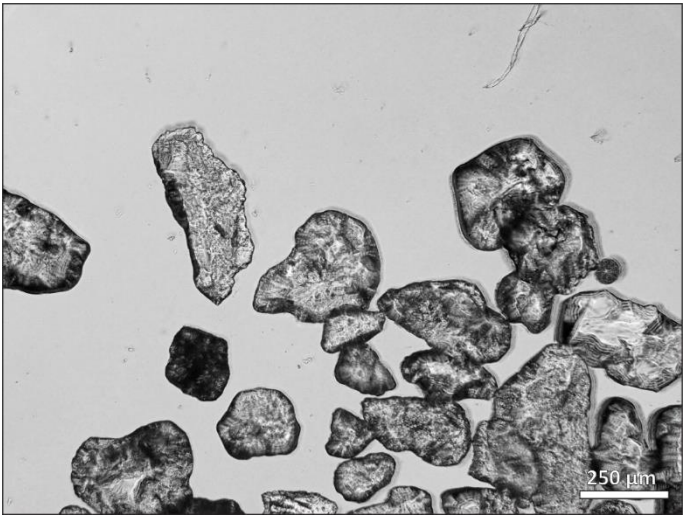

Figure S01. Photomicrograph of sand grains. Monochrome bright-field image of the investigated intertidal sand grains reveal heterogeneous shapes and irregularities on the sand surface.

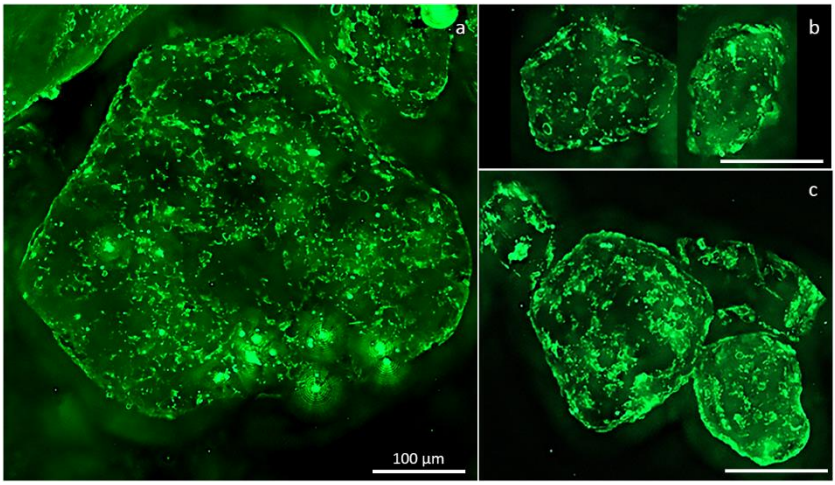

Figure S02. Colonization of sand grains by microorganisms. **a-c** dsDNA staining (SYBR Green I, green, exc.: 469/35 nm, em.: 510/42 nm) of representative sand grains indicates a patchy microbial colonization. In total 50 sand grains were analyzed for cell-counts, cell-cell distance and distance between patches. A maximum intensity projection was carried out for a z-stack of 25 images.

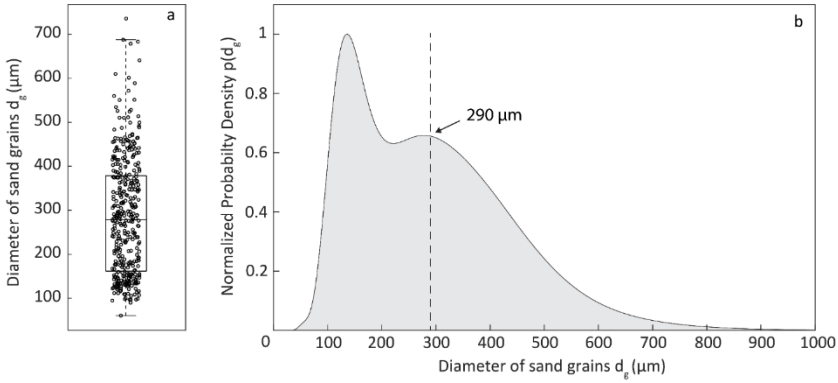

Figure S03. Sediment grain size distribution determined from photomicrographs. a Variation in the size of the sand grains is represented using a box-whisker plot where the upper and lower sides are the quartiles, the line in the box represents the median, and the upper and lower line represent maximum and minimum excluding outliers. **b** Sand grain probability density distribution with the median at 290 µm (dashed line, n = 400).

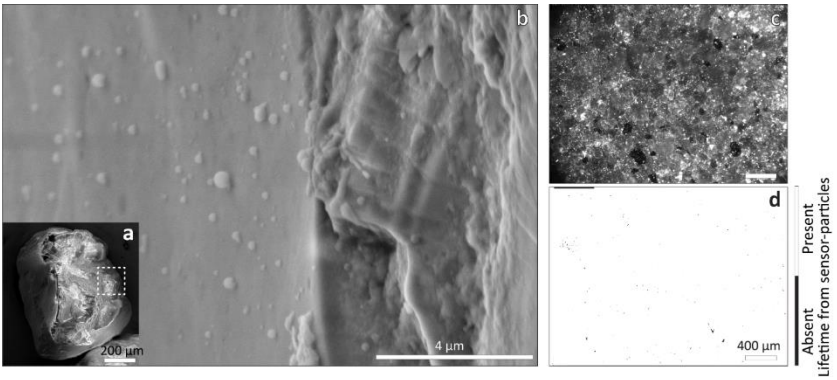

Figure S04. Scanning electron micrographs and life-time imaging of sensor particles coated on sand grains. **a,b** Scanning electron micrograph of sand grains showing the distribution of sensor particles on the surface of a sand grain (~5 particles μm^{-2}). We applied lifetime imaging to determine the presence of sensor particles on the sand grain surface, **c** intensity image (exc.: ~450 nm, em.: 500-550 nm) of sand grains with sensor particles, **d** binary image of the fluorescence lifetime where a threshold of 30 µs was selected. White pixels indicate a lifetime where sensor particles are present (lifetime > 30 µs) and black indicates areas where sensor particles were absent (< 30 µs).

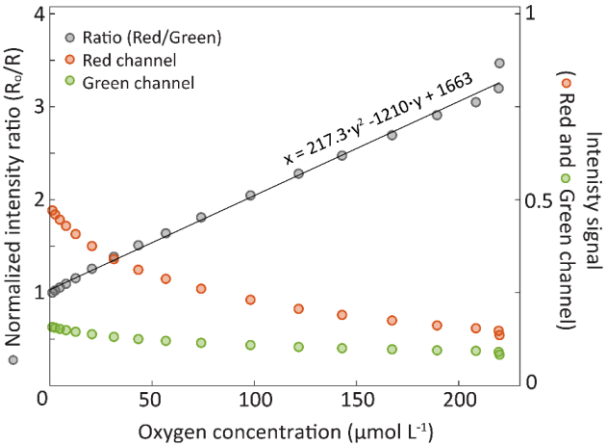

Figure S05. Calibration curve for sensor particles. Ratiometric imaging was performed using a RGB camera. The oxygen-sensitive luminescence (red circles, red channel R) was referenced through an oxygen-insensitive dye (green circles, green channel G). The ratiometric signal (R/G) is shown in gray with solid line representing the best fit which was used for calibration.

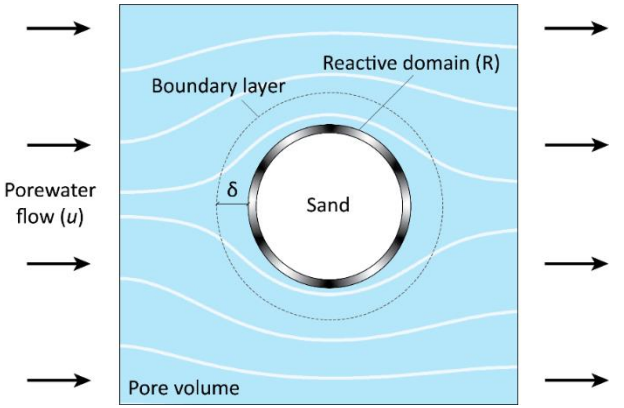

Figure S06. Schematic of the domain used for the mathematical model. In the pore volume the Stokes equations were solved with no-slip conditions at the outer boundary of the reactive domain. Scalar transport equations were solved for the entire domain with reaction terms only active in the reactive domain. Oxygen consumption and production within the reactive sub-domain were added as sinusoidal waves indicated through black and white, where, black indicates consumption and white indicates the production of O_2. Streamlines represent the flow path and the total domain size represents 500 x 500 µm. All relevant parameters and equations are listed in table S1.

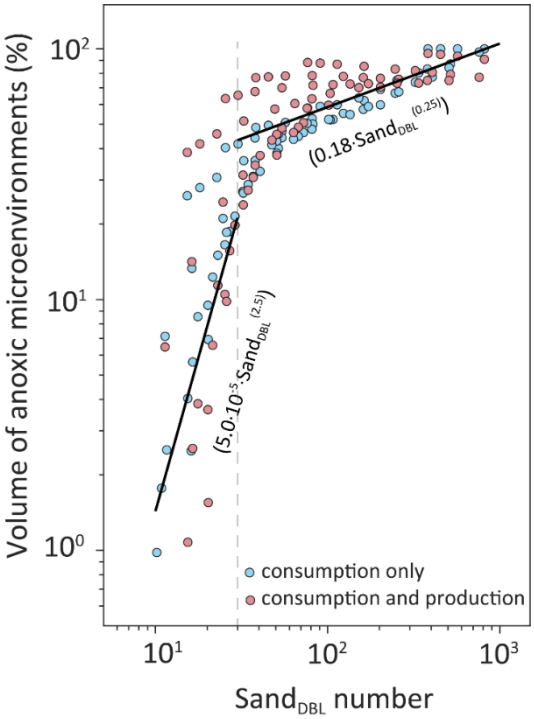

Figure S07. Scaling of anoxic volumes with the non-dimensional $Sand_{DBL}$ number. The phase space between the SandDBL number and the anoxic volumes indicates two regimes. For SandDBL < 30 best fit was found for $5.0 \cdot 10^{-5} \cdot Sand_{DBL}^{(2.5)}$ (r-squared value 0.4) and for SandDBL > 30 best fit was found for $0.18 \cdot Sand_{DBL}^{(0.25)}$ (r-squared value 0.6), and universal fit for $1\text{-}1.87 \cdot Sand_{DBL}^{(-0.26)}$ (r-squared value 0.6). The data set covers all model runs for SandDBL between 10 and 1000 of anoxic microenvironments with only O_2 consumption on the sand grain surface and simultaneous O_2 consumption and production.

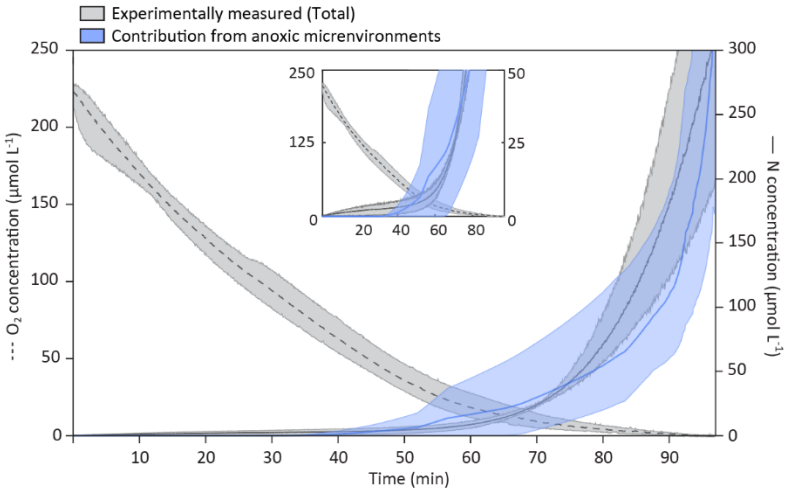

Figure S08. Denitrification attributed to anoxic microenvironments in sediment with bulk oxic porewater. Co-occurring of O_2 respiration (dotted line) and N production (solid line) based on experimental measurements (grey) in sandy sediments compared to contribution of N produced from the anoxic environments (blue) derived using the here- derived scaling law.

Table S1. Model Parameters.

Parameter	Equation/Values adopted	Description
D_{O2}	$2.0 \cdot 10^{-9}$ m² s^{-1}	Diffusion coefficient of O_2 in water (Stewart, 2003)
D_{N2}	$2.6 \cdot 10^{-9}$ m² s^{-1}	Diffusion coefficient of N_2 in water (Stewart, 2003)
D_{eps}	$1.1 \cdot 10^{-9}$ m² s^{-1}	Diffusion coefficient of gas corrected for EPS/biofilm in the reactive zone (Stewart, 2003)
d_g	290 µm	Median diameter of sand grains
vel	0 - 1000 µm s^{-1}	Pore water velocity[a] (Kösters & Winter, 2014; Reimers et al., 2004, 2012)
Oxygen rate (production / consumption)	(R_C * func * c_{O2} / (c_{O2}+K_m))	Michaelis–Menten kinetics for O_2 production and consumption in the reactive zone
R_C	203.89 µmol L^{-1} s^{-1}	Single-cell volumetric oxygen consumption rate (Ahmerkamp et al., 2020)
func	(sin(atan(y/x)*4) - 0.3)	Equation for sinusoidal spatial distribution of oxygen production and consumption rates in the reactive zone
x,y		Spatial location of point in the reactive zone
c_{O2}	0 - 100 µmol L^{-1}	Inflow O_2 concentration
[a]Values adopted based on in situ measurements for bottom water velocity and pore water velocity		

Parameter	**Equation/Values adopted**	**Description**
K_m	0.1 µmol L^{-1}	Half-saturation constant for O_2
Denitrification rate (N_2 production)	((-R_C) * func * cf * c_inh/(c_inh+c_2) / 2)	N_2 production based on experimental data
c_{N2}		N_2 concentration
cf	0.1	Ratio of aerobic respiration (AR) rates to denitrification (DN) (Marchant et al., 2017)
c_{inh}	0.1 µmol L^{-1}	Inhibition constant for denitrification (Chen & Strous, 2013; Evrard et al., 2013)

References

Ahmerkamp, S., Jalaluddin, F. M., Cui, Y., Brumley, D. R., Pacherres, C. O., Berg, J. S., Stocker, R., Kuypers, M. M. M., Koren, K., & Behrendt, L. (2022). Simultaneous visualization of flow fields and oxygen concentrations to unravel transport and metabolic processes in biological systems. *Cell Reports Methods*, *2*(5), 100216. https://doi.org/10.1016/j.crmeth.2022.100216

Ahmerkamp, S., Marchant, H. K., Peng, C., Probandt, D., Littmann, S., Kuypers, M. M. M., & Holtappels, M. (2020). The effect of sediment grain properties and porewater flow on microbial abundance and respiration in permeable sediments. *Scientific Reports*, *10*(1), 1–12. https://doi.org/10.1038/s41598-020-60557-7

Ahmerkamp, S., Winter, C., Krämer, K., Beer, D. de, Janssen, F., Friedrich, J., Kuypers, M. M. M., & Holtappels, M. (2017). Regulation of benthic oxygen fluxes in permeable sediments of the coastal ocean. *Limnology and Oceanography*, *62*(5), 1935–1954. https://doi.org/10.1002/lno.10544

Anderson, J. G., & Meadows, P. S. (1978). Microenvironments in marine sediments. *Proceedings of the Royal Society of Edinburgh. Section B. Biological Sciences*, *76*(1–3), 1–16. https://doi.org/10.1017/S0269727000002761

Aufrecht, J. A., Fowlkes, J. D., Bible, A. N., Morrell-Falvey, J., Doktycz, M. J., & Retterer, S. T. (2018). Pore-scale hydrodynamics influence the spatial evolution of bacterial biofilms in a microfluidic porous network. *PLoS ONE*, *14*(6), 1–17. https://doi.org/10.1371/journal.pone.0218316

Bourceau, O. M., Ferdelman, T., Lavik, G., Mussmann, M., Kuypers, M. M. M., & Marchant, H. K. (2023). Simultaneous sulfate and nitrate reduction in coastal sediments. *ISME Communications*, *3*(1), 17. https://doi.org/10.1038/s43705-023-00222-y

Cardenas, M. B., Cook, P. L. M., Jiang, H., & Traykovski, P. (2008). Constraining denitrification in permeable wave-influenced marine sediment using linked hydrodynamic and biogeochemical modeling. *Earth and Planetary Science Letters*, *275*(1–2), 127–137. https://doi.org/10.1016/j.epsl.2008.08.016

Ceriotti, G., Borisov, S. M., Berg, J. S., & de Anna, P. (2022). Morphology and Size of Bacterial Colonies Control Anoxic Microenvironment Formation in Porous Media. *Environmental Science & Technology*, *56*(23), 17471–17480. https://doi.org/10.1021/acs.est.2c05842

Chen, J., & Strous, M. (2013). Denitrification and aerobic respiration, hybrid electron transport chains and co-evolution. *Biochimica et Biophysica Acta - Bioenergetics*, *1827*(2), 136–144. https://doi.org/10.1016/j.bbabio.2012.10.002

Chua, E. J., Huettel, M., Fennel, K., & Fulweiler, R. W. (2022). A case for addressing the unresolved role of permeable shelf sediments in ocean denitrification. *Limnology And Oceanography Letters*, *7*(1), 11–25. https://doi.org/10.1002/lol2.10218

Costerton, J. W., Lewandowski, Z., DeBeer, D., Caldwell, D., Korber, D., & James, G. (1994). Biofilms, the customized microniche. *Journal of Bacteriology*, *176*(8), 2137–2142. https://doi.org/10.1128/jb.176.8.2137-2142.1994

Coyte, K. Z., Tabuteau, H., Gaffney, E. A., Fostera, K. R., & Durham, W. M. (2017). Microbial competition in porous environments can select against rapid biofilm growth. *Proceedings of the National Academy of Sciences of the United States of America*, *114*(2), E161–E170. https://doi.org/10.1073/pnas.1525228113

de Anna, P., Pahlavan, A. A., Yawata, Y., Stocker, R., & Juanes, R. (2021). Chemotaxis under flow disorder shapes microbial dispersion in porous media. *Nature Physics*, *17*(1), 68–73. https://doi.org/10.1038/s41567-020-1002-x

de Beer, D., Stoodley, P., Roe, F., & Lewandowski, Z. (1994). Effects of biofilm structures on oxygen distribution and mass transport. *Biotechnology and Bioengineering*, *43*(11), 1131–1138. https://doi.org/10.1002/bit.260431118

de Beer, D., Wenzhöfer, F., Ferdelman, T. G., Boehme, S. E., Huettel, M., van Beusekom, J. E. E., Böttcher, M. E., Musat, N., & Dubilier, N. (2005). Transport and mineralization rates in North Sea sandy intertidal sediments, Sylt-Rømø Basin, Wadden Sea. *Limnology and Oceanography*, *50*(1), 113–127. https://doi.org/10.4319/lo.2005.50.1.0113

Drescher, K., Shen, Y., Bassler, B. L., & Stone, H. A. (2013). Biofilm streamers cause catastrophic disruption of flow with consequences for environmental and medical systems. *Proceedings of the National Academy of Sciences of the United States of America*, *110*(11), 4345–4350. https://doi.org/10.1073/pnas.1300321110

Elliott, H., & Brooks, N. H. (1997). Transfer of nonsorbing solutes to a streambed with bed forms : Theory permeable streambed and the overlying water of

a stream or river is presented in this In a companion paper this issue] the results of experimental n + 00t Os u n + 00t Os q (x) = U •. *Water Resources Research*, *33*(1), 123–136.

Evrard, V., Glud, R. N., & Cook, P. L. M. (2013). The kinetics of denitrification in permeable sediments. *Biogeochemistry*, *113*(1–3), 563–572. https://doi.org/10.1007/s10533-012-9789-x

Franklin, S., Vasilas, B., & Jin, Y. (2019). More than Meets the Dye: Evaluating Preferential Flow Paths as Microbial Hotspots. *Vadose Zone Journal*, *18*(1), 1–8. https://doi.org/10.2136/vzj2019.03.0024

Franqueira, D., Orosa, M., Torres, E., Herrero, C., & Cid, A. (2000). Potential use of flow cytometry in toxicity studies with microalgae. *Science of the Total Environment*, *247*(2–3), 119–126. https://doi.org/10.1016/S0048-9697(99)00483-0

Fraser, H. J. (1935). Experimental Study of the Porosity and Permeability of Clastic Sediments. *The Journal of Geology*, *43*(8, Part I), 910–1010. https://www.jstor.org/stable/30058422

Gao, H., Matyka, M., Liu, B., Khalili, A., Kostka, J. E., Collins, G., Jansen, S., Holtappels, M., Jensen, M. M., Badewien, T. H., Beck, M., Grunwal, M., de Beer, D., Lavik, G., & Kuypers, M. M. M. (2012). Intensive and extensive nitrogen loss from intertidal permeable sediments of the Wadden Sea. *Limnology and Oceanography*, *57*(1), 185–198. https://doi.org/10.4319/lo.2012.57.1.0185

Gao, H., Schreiber, F., Collins, G., Jensen, M. M., Kostka, J. E., Lavik, G., De Beer, D., Zhou, H. Y., & Kuypers, M. M. M. (2010). Aerobic denitrification in

permeable Wadden Sea sediments. *ISME Journal*, *4*(3), 417–426. https://doi.org/10.1038/ismej.2009.127

Gihring, T. M., Lavik, G., Kuypers, M. M. M., & Kostka, J. E. (2010). Direct determination of nitrogen cycling rates and pathways in Arctic fjord sediments (Svalbard, Norway). *Limnology and Oceanography*, *55*(2), 740–752. https://doi.org/10.4319/lo.2009.55.2.0740

Greg Mitchell, B., & Kiefer, D. A. (1988). Chlorophyll α specific absorption and fluorescence excitation spectra for light-limited phytoplankton. *Deep Sea Research Part A, Oceanographic Research Papers*, *35*(5), 639–663. https://doi.org/10.1016/0198-0149(88)90024-6

Hense, B. A., Gais, P., Jütting, U., Scherb, H., & Rodenacker, K. (2008). Use of fluorescence information for automated phytoplankton investigation by image analysis. *Journal of Plankton Research*, *30*(5), 587–606. https://doi.org/10.1093/plankt/fbn024

Huettel, M, & Gust, G. (1992). Solute release mechanisms from confined sediment sediment cores in stirred benthic chambers and flume flows. *Marine Ecology Progress Series*, *82*, 187–197. https://www.int-res.com/articles/meps/82/m082p187.pdf

Huettel, Markus, Berg, P., & Kostka, J. E. (2014). Benthic Exchange and Biogeochemical Cycling in Permeable Sediments. *Annual Review of Marine Science*, *6*(1), 23–51. https://doi.org/10.1146/annurev-marine-051413-012706

Huettel, Markus, Røy, H., Precht, E., & Ehrenhauss, S. (2003). Hydrodynamical impact on biogeochemical processes in aquatic sediments. *Hydrobiologia*,

494(1–3), 231–236. https://doi.org/10.1023/A:1025426601773

Keiluweit, M., Gee, K., Denney, A., & Fendorf, S. (2018). Anoxic microsites in upland soils dominantly controlled by clay content. *Soil Biology and Biochemistry*, *118*(December 2017), 42–50. https://doi.org/10.1016/j.soilbio.2017.12.002

Kessler, A. J., Cardenas, M. B., Santos, I. R., & Cook, P. L. M. (2014). Enhancement of denitrification in permeable carbonate sediment due to intra-granular porosity: A multi-scale modelling analysis. *Geochimica et Cosmochimica Acta*, *141*, 440–453. https://doi.org/10.1016/j.gca.2014.06.028

Kiørboe, T. (2001). Formation and fate of marine snow: Small-scale processes with large-scale implications. *Scientia Marina*, *65*(SUPPLEMENT 2), 57–71. https://doi.org/10.3989/scimar.2001.65s257

Koren, K., Brodersen, K. E., Jakobsen, S. L., & Kühl, M. (2015). Optical sensor nanoparticles in artificial sediments-a new tool to visualize O2 dynamics around the rhizome and roots of seagrasses. *Environmental Science and Technology*, *49*(4), 2286–2292. https://doi.org/10.1021/es505734b

Koren, K., Jakobsen, S. L., & Kühl, M. (2016). In-vivo imaging of O2 dynamics on coral surfaces spray-painted with sensor nanoparticles. *Sensors and Actuators, B: Chemical*, *237*, 1095–1101. https://doi.org/10.1016/j.snb.2016.05.147

Kösters, F., & Winter, C. (2014). Exploring German Bight coastal morphodynamics based on modelled bed shear stress. *Geo-Marine Letters*, *34*(1), 21–36. https://doi.org/10.1007/s00367-013-0346-y

Kuriyama, K., Gründling-Pfaff, S., Diehl, N., Woelfel, J., & Karsten, U. (2021). Microphytobenthic primary production on exposed coastal sandy sediments of the Southern Baltic Sea using ex situ sediment cores and oxygen optodes. *Oceanologia*, *63*(2), 247–260. https://doi.org/10.1016/j.oceano.2021.02.002

Kurz, D. L., Secchi, E., Carrillo, F. J., Bourg, I. C., Stocker, R., & Jimenez-Martine, J. (2022). Competition between growth and shear stress drives intermittency in preferential flow paths in porous medium biofilms. *Proceedings of the National Academy of Sciences of the United States of America*, *119*(30), 1–10. https://doi.org/10.1073/pnas.2122202119

Lehto, N., Glud, R. N., á Nordi, G., Zhang, H., & Davison, W. (2014). Anoxic microniches in marine sediments induced by aggregate settlement: Biogeochemical dynamics and implications. *Biogeochemistry*, *119*(1–3), 307–327. https://doi.org/10.1007/s10533-014-9967-0

Li, C., Ding, S., Yang, L., Zhu, Q., Chen, M., Tsang, D. C. W., Cai, G., Feng, C., Wang, Y., & Zhang, C. (2019). Planar optode: A two-dimensional imaging technique for studying spatial-temporal dynamics of solutes in sediment and soil. *Earth-Science Reviews*, *197*(February), 102916. https://doi.org/10.1016/j.earscirev.2019.102916

Lichtenthaler, H. K., & Buschmann, C. (2001). Chlorophylls and Carotenoids: Measurement and Characterization by UV-VIS Spectroscopy. *Current Protocols in Food Analytical Chemistry*, *1*(1), F4.3.1-F4.3.8. https://doi.org/10.1002/0471142913.faf0403s01

Marchant, H. K., Ahmerkamp, S., Lavik, G., Tegetmeyer, H. E., Graf, J., Klatt, J. M., Holtappels, M., Walpersdorf, E., & Kuypers, M. M. M. (2017). Denitrifying

community in coastal sediments performs aerobic and anaerobic respiration simultaneously. *ISME Journal*, *11*(8), 1799–1812. https://doi.org/10.1038/ismej.2017.51

Marchant, H. K., Holtappels, M., Lavik, G., Ahmerkamp, S., Winter, C., & Kuypers, M. M. M. (2016). Coupled nitrification-denitrification leads to extensive N loss in subtidal permeable sediments. *Limnology and Oceanography*, *61*(3), 1033–1048. https://doi.org/10.1002/lno.10271

Matyka, M., Khalili, A., & Koza, Z. (2008). Tortuosity-porosity relation in porous media flow. *Physical Review E - Statistical, Nonlinear, and Soft Matter Physics*, *78*(2), 1–8. https://doi.org/10.1103/PhysRevE.78.026306

Miller, D. (1989). Abrasion effects on microbes in sandy sediments. *Marine Ecology Progress Series*, *55*(1), 73–82. https://doi.org/10.3354/meps055073

Mistlberger, G., Koren, K., Scheucher, E., Aigner, D., Borisov, S. M., Zankel, A., Pölt, P., & Klimant, I. (2010). Multifunctional magnetic optical sensor particles with tunable sizes for monitoring metabolic parameters and as a basis for nanotherapeutics. *Advanced Functional Materials*, *20*(11), 1842–1851. https://doi.org/10.1002/adfm.201000321

Moßhammer, M., Brodersen, K. E., Kühl, M., & Koren, K. (2019). Nanoparticle- and microparticle-based luminescence imaging of chemical species and temperature in aquatic systems: a review. *Microchimica Acta*, *186*(2), 20–23. https://doi.org/10.1007/s00604-018-3202-y

Nelson, J. R., Eckman, J. E., Robertson, C. Y., Marinelli, R. L., & Jahnke, R. A. (1999). Benthic microalgal biomass and irradiance at the sea floor on the

continental shelf of the South Atlantic Bight: Spatial and temporal variability and storm effects. *Continental Shelf Research*, *19*(4), 477–505. https://doi.org/10.1016/S0278-4343(98)00092-2

Nøhr Glud, R., Gundersen, J. K., Barker Jørgensen, B., Revsbech, N. P., & Schulz, H. D. (1994). Diffusive and total oxygen uptake of deep-sea sediments in the eastern South Atlantic Ocean:in situ and laboratory measurements. *Deep Sea Research Part I: Oceanographic Research Papers*, *41*(11–12), 1767–1788. https://doi.org/10.1016/0967-0637(94)90072-8

Paterson D. M. (1995). Biogenic structure of early sediment fabric visualized by low-temperature scanning electron microscopy. *Journal of the Geological Society*, *152*(1), 131–140. https://doi.org/10.1144/gsjgs.152.1.0131

Ploug, H., Hietanen, S., & Kuparinen, J. (2002). Diffusion and advection within and around sinking, porous diatom aggregates. *Limnology and Oceanography*, *47*(4), 1129–1136. https://doi.org/10.4319/lo.2002.47.4.1129

Polerecky, L., Franke, U., Werner, U., Grunwald, B., & De Beer, D. (2005). High spatial resolution measurement of oxygen consumption rates in permeable sediments. *Limnology and Oceanography: Methods*, *3*(FEB.), 75–85. https://doi.org/10.4319/lom.2005.3.75

Precht, E., & Huettel, M. (2004). Rapid wave-driven advective pore water exchange in a permeable coastal sediment. *Journal of Sea Research*, *51*(2), 93–107. https://doi.org/10.1016/j.seares.2003.07.003

Probandt, D., Knittel, K., Tegetmeyer, H. E., Ahmerkamp, S., Holtappels, M., & Amann, R. (2017). Permeability shapes bacterial communities in sublittoral surface sediments. *Environmental Microbiology*, *19*(4), 1584–

1599. https://doi.org/10.1111/1462-2920.13676

Rani, S. A., Pitts, B., Beyenal, H., Veluchamy, R. A., Lewandowski, Z., Davison, W. M., Buckingham-Meyer, K., & Stewart, P. S. (2007). Spatial patterns of DNA replication, protein synthesis, and oxygen concentration within bacterial biofilms reveal diverse physiological states. *Journal of Bacteriology*, *189*(11), 4223–4233. https://doi.org/10.1128/JB.00107-07

Rao, A. M. F., McCarthy, M. J., Gardner, W. S., & Jahnke, R. A. (2007). Respiration and denitrification in permeable continental shelf deposits on the South Atlantic Bight: Rates of carbon and nitrogen cycling from sediment column experiments. *Continental Shelf Research*, *27*(13), 1801–1819. https://doi.org/10.1016/j.csr.2007.03.001

Reimers, C. E., Özkan-Haller, H. T., Berg, P., Devol, A., McCann-Grosvenor, K., & Sanders, R. D. (2012). Benthic oxygen consumption rates during hypoxic conditions on the Oregon continental shelf: Evaluation of the eddy correlation method. *Journal of Geophysical Research: Oceans*, *117*(C2), n/a-n/a. https://doi.org/10.1029/2011JC007564

Reimers, C. E., Stecher, H. A., Taghon, G. L., Fuller, C. M., Huettel, M., Rusch, A., Ryckelynck, N., & Wild, C. (2004). In situ measurements of advective solute transport in permeable shelf sands. *Continental Shelf Research*, *24*(2), 183–201. https://doi.org/10.1016/j.csr.2003.10.005

Revsbech, N. P., & Jørgensen, B. B. (1986). Microelectrodes: their use in microbial ecology. In *Advances in Microbial Ecology* (pp. 293–352). https://doi.org/10.1007/978-1-4757-0611-6_5

Savant, S. A., Reible, D. D., & Thibodeaux, L. J. (1987). Convective transport within

stable river sediments. *Water Resources Research*, *23*(9), 1763–1768. https://doi.org/10.1029/WR023i009p01763

Scheidweiler, D., Peter, H., Pramateftaki, P., de Anna, P., & Battin, T. J. (2019). Unraveling the biophysical underpinnings to the success of multispecies biofilms in porous environments. *ISME Journal*, *13*(7), 1700–1710. https://doi.org/10.1038/s41396-019-0381-4

Sokoll, S., Lavik, G., Sommer, S., Goldhammer, T., Kuypers, M. M. M., & Holtappels, M. (2016). Extensive nitrogen loss from permeable sediments off North-West Africa. *Journal of Geophysical Research: Biogeosciences*, *121*(4), 1144–1157. https://doi.org/10.1002/2015JG003298

Stewart, P. S. (2003). Diffusion in Biofilms. *Journal of Bacteriology*, *185*(5), 1485–1491. https://doi.org/10.1128/JB.185.5.1485

Stewart, P. S., & Franklin, M. J. (2008). Physiological heterogeneity in biofilms. *Nature Reviews Microbiology*, *6*(3), 199–210. https://doi.org/10.1038/nrmicro1838

Védère, C., Vieublé Gonod, L., Nunan, N., & Chenu, C. (2022). Opportunities and limits in imaging microorganisms and their activities in soil microhabitats. *Soil Biology and Biochemistry*, *174*, 108807. https://doi.org/10.1016/j.soilbio.2022.108807

Wörman, A. (1998). Analytical solution and timescale for transport of reacting solutes in rivers and streams. *Water Resources Research*, *34*(10), 2703–2716. https://doi.org/10.1029/98WR01338

Zetsche, E., Paterson, D. M., Lumsdon, D. G., & Witte, U. (2011). Temporal

variation in the sediment permeability of an intertidal sandflat. *Marine Ecology Progress Series*, *441*, 49–63. https://doi.org/10.3354/meps09390

Zumft, W. G. (1997). Cell biology and molecular basis of denitrification. *Microbiology and Molecular Biology Reviews*, *61*(4), 533–616. https://doi.org/10.1128/mmbr.61.4.533-616.1997

Chapter 3

Simultaneous visualization of flow fields and oxygen concentrations to unravel transport and metabolic processes in biological systems

---

Soeren Ahmerkamp[1,*], Farooq Moin Jalaluddin[1,*], Yuan Cui[2,*], Douglas R. Brumley[3], Cesar O. Pacherres[4,8], Jasmine Berg[5], Roman Stocker[6], Marcel MM Kuypers[1], Klaus Koren[7], Lars Behrendt[2]

* Authors contributed equally

Authors Affiliations

[1] Max Planck Institute for Marine Microbiology, 28359 Bremen, Germany
[2] Science for Life Laboratory, Department of Environmental Toxicology, Uppsala University, 75236 Uppsala, Sweden
[3] School of Mathematics and Statistics, The University of Melbourne, Victoria 3010, Australia
[4] Alfred Wegener Institute, Helmholtz Centre for Polar and Marine Research, Germany
[5] University of Lausanne, Lausanne, Switzerland
[6] Institute for Environmental Engineering, Department of Civil, Environmental and Geomatic Engineering, ETH Zurich, 8093 Zurich, Switzerland
[7] Aarhus University Centre for Water Technology, Department of Biology, Aarhus University, 8000 Aarhus, Denmark
[8] Current Address: Copenhagen University, Department of Biology, Denmark

Corresponding authors: sahmerka@mpi-bremen.de, klaus.koren@bio.au.dk, lars.behrendt@scilifelab.uu.se. Lead corresponding author: Soeren Ahmerkamp (sahmerka@mpi-bremen.de)

Manuscript published in Cell Report Methods
https://doi.org/10.1016/j.crmeth.2022.100216

Motivation

In aquatic environments, oxygen (O_2) production and consumption are intimately connected via transport processes. Many organisms interact with or generate flow fields to enhance exchange-processes and optimize their metabolism, yet our understanding on these complex interactions is mostly derived from simplified mathematical models. This is primarily because we lack methods that can accurately measure transport processes and O_2 concentrations at the same time. To address this problem, we developed 'sensPIV' a simple, inexpensive, yet powerful method that uses chemically sensing microparticles to quantitatively link O_2 distributions to physical transport processes.

Highlights

- sensPIV uses chemically sensing particles to visualize O_2 concentrations and flows
- Measurements can be performed with simple setups available in many labs
- O_2 transport can be measured in microfluidic devices, aggregates and live corals
- sensPIV shows that ciliary flows optimize coral metabolism

eTOC Blurb

Ahmerkamp et al. present sensPIV, a simple, inexpensive, yet powerful method that uses chemically sensing microparticles to quantitatively link oxygen distributions to physical transport processes. SensPIV can be used to study flow-organism interactions across many life-science and engineering applications.

Summary

From individual cells to whole organisms, O_2 transport unfolds across micrometer to millimeter length scales and can change within milliseconds in response to fluid flows and organismal behavior. The spatio-temporal complexity of these processes makes the accurate assessment of O_2 dynamics via currently available methods difficult or unreliable. Here, we present 'sensPIV' a method to simultaneously measure O_2 concentrations and flow fields. By tracking O_2 sensitive microparticles in flow using imaging technologies that allow for instantaneous referencing, we measured O_2 transport within i) microfluidic devices, ii) sinking model aggregates and iii) complex colony-forming corals. Through the use of sensPIV we find that corals use ciliary movement to link zones of photosynthetic O_2 production to zones of O_2 consumption. SensPIV can potentially be extendable to study flow-organism interactions across many life-science and engineering applications

Introduction

The production of dioxygen (O_2) by photosynthesis began approximately 2.3 billion years ago and the high energy yield obtained from O_2 respiration enabled the development of multicellular life on Earth (Bekker et al., 2004; Falkowski, 2006). However, the poor water solubility of O_2 places fundamental constraints on biological metabolism. The molecular diffusion of O_2, or diffusive flux, around and into cells is typically slow compared to intracellular reaction rates. To expedite the transport of O_2 from regions of production to consumption, life has evolved a range of ventilation mechanisms to enhance fluid flow in close proximity of cells. The magnitude and direction of this flow transports solutes, resulting in an advective flux. In systems ranging from coral surfaces to circulatory systems of animals, biological metabolism and physical transport processes (i.e. advection and diffusion) are intimately linked and unfold dynamically (from milliseconds to days) across spatial scales (µm to mm). Charting the complex interplay between O_2 production, consumption and transport processes is only possible through simultaneously measuring these quantities in a dynamic fashion. However, existing methods have largely focused on measuring O_2 concentrations and transport processes separately. Here we expand the toolbox of existing O_2-sensing techniques by combining particle image velocimetry (PIV) with optode-based chemical sensing. This method, chemical-sensing Particle Image Velocimetry ('sensPIV'), now enables measurements of transport processes and O_2 concentrations simultaneously across spatial scales and environments.

Microscale transport is usually measured on particle ensembles via PIV, or by particle tracking velocimetry (PTV) which tracks individual particles in fluid flow. Both methods repeatedly image naturally-occurring or artificially-added particles (typical size 0.1-10 µm) to obtain information about the local speed and direction of fluid flow. Based on this information, flow fields can be accurately reconstructed

in 2D or, using stereoscopic or tomographic approaches in 3D (Raffel et al., 1998; Westerweel et al., 2013). A number of commercially available PIV systems and image processing tools have enabled researchers to describe transport processes such as blood flow through cardiovascular systems (Kheradvar et al., 2010; Yousif et al., 2011) or the interaction of small crustacea (Gemmell et al., 2014), flocs or particles (Zetsche et al., 2020), jellyfish (Costello et al., 2021; Gemmell et al., 2015) and planktonic protists (Drescher et al., 2010; Gilpin et al., 2017; Nielsen & Kiørboe, 2021) with their flow field. While these studies have provided insights into the interaction of organisms with surrounding flow fields during propulsion or foraging, they do not provide a quantitative assessment of how transport processes affect fluxes of O_2.

Microscale O_2 measurements have traditionally been performed using amperometric micro-electrodes (Clark et al., 1953). Owing to their high accuracy and resolution, microsensors have decisively influenced our understanding of the role of O_2 in biogeochemical processes (Revsbech & Jørgensen, 1986), human physiology (Sheffield, 1998), and plant physiology (Pedersen et al., 1998). More recently, optical sensors called optodes, have emerged as powerful tools for measuring O_2. This technology is based on the O_2-dependent phosphorescence quenching of a chemical indicator enabling contactless O_2 sensing (Klimant et al., 1995; Morris et al., 1993). By entrapping the indicator chemical in a polymeric matrix, surfaces can be coated resulting in a variety of sensor types such as optical fibers or planar optodes. Planar optodes enable the imaging of O_2 in 2D and have revolutionized our understanding of O_2 distributions and their heterogeneity within complex biological samples like sediments (Frederiksen & Glud, 2006; Meysman et al., 2010; Stockdale et al., 2009) or dental plaque (Khosravi et al., 2020). Recently, micro- and nanoparticle-based optodes (optode particles) have been used to visualize O_2 concentrations around microorganisms (Kühl et al., 2020), within microorganisms (Okkelman et al., 2020; Tobita & Yoshihara, 2016;

Zhdanov et al., 2015) and in the bone marrow of live animals (Spencer et al., 2014). Despite these powerful applications, the drawbacks of optodes include their low temporal resolution and the fact that planar optodes affect advective transport by acting as a wall and modifying the flow. As a result, optodes are typically applied to static measurements of O_2 concentrations and diffusive transport. In nature, however, organisms interact with complex O_2 gradients emanating from changing flow, aerotaxis or O_2 uptake (Guasto et al., 2012; Stocker, 2012). Studying the microscale organization of O_2 fluxes thus requires the ability to concurrently visualize O_2 gradients and advective transport.

The importance of combining measurements of transport processes and O_2 concentrations has already been highlighted by some studies. For example, sequential measurements using PIV and microsensors uncovered the effects of ciliary flow on O_2 exchange in coral boundary layers (Pacherres et al., 2022; Shapiro et al., 2014). Unfortunately, such studies could not fully resolve the spatial distribution of O_2 as microsensors can disturb flow fields. Concentration gradients and flow within, e.g., the phycosphere of individual algae or bacteria (Sommer et al., 2017) may also exhibit strong variation in time and space and to measure such minute changes in O_2 it is important to apply sensors that are non-invasive. Yet, only a handful of studies (Abe et al., 2004; Kim et al., 2013) have succeeded in measuring O_2 concentrations and advective flow simultaneously and non-invasively using complex, highly controlled experimental setups. In particular, difficulties in compensating for uneven illumination and small windows of detectable O_2 concentrations have prevented a broad implementation of these techniques. A simple, reliable and reproducible approach that combines measurements of transport processes with O_2 sensing is needed to enable the systematic study of how organisms interact with and modify their environment to optimize transport across a range of spatial scales.

Here we present 'sensPIV', a method that combines the ability of optodes to dynamically measure O_2 with the ability of PIV to accurately resolve advective and diffusive transport processes. Using sensPIV, the interplay between transport processes and biological reactions can now be investigated at high resolution across a range of environments using experimental setups available in many laboratories. We demonstrate the versatility of sensPIV by applying it to three contrasting experimental systems of increasing complexity: microfluidic devices, artificial marine aggregates and living coral fragments. Our sensPIV measurements reveal how flow fields increase exchange processes around particles and how corals actively modulate their microenvironment to enhance the flux of O_2.

Results

Method development

There are three essential steps to successfully employ sensPIV: i) the synthesis of O_2-sensitive optode particles ii) the correct illumination of optode particles and iii) the correct choice of imaging modalities.

Synthesis of sensPIV particles

Particles used for sensPIV must exhibit a quantifiable quenching response over a range of O_2 concentrations, fast response times and good imaging capabilities. Although many O_2-sensitive compounds fulfill these requirements (see for example (Quaranta et al., 2012; Wang & Wolfbeis, 2014) for chemistry overview), we recommend the use of Platinum(II) meso- (2,3,4,5,6-pentafluoro)phenyl porphyrin (PtTFPP) as it is commercially available, photostable, relatively unaffected by temperature and exhibits a good sensitivity across a broad range of O_2 concentrations (Figure 01a-h, Supplementary Video 1, see (Borisov et al., 2008)). The dynamic-quenching of PtTFPP by O_2 leads to a reversible, O_2-dependent change in luminescence intensity as well as luminescence lifetime. This relationship is described by the Stern-Volmer relationship:

$$\frac{\tau_0}{\tau} - 1 = \frac{I_0}{I} - 1 = K_{SV} \cdot [O_2] \qquad \text{(equation 01)}$$

where K_{sv} is the Stern-Volmer constant, $[O_2]$ is the dissolved- O_2 concentration, I is the luminescence intensity at a given dissolved O_2 concentration and I_0 the luminescence intensity in the absence of O_2. The same relationship applies to the luminescence lifetime in the presence (τ) and absence of O_2 (τ_0). From Equation (1), it follows that the calibration of sensPIV particles can be performed by measuring the luminescence intensities of O_2 -sensitive dyes at known O_2 concentrations.

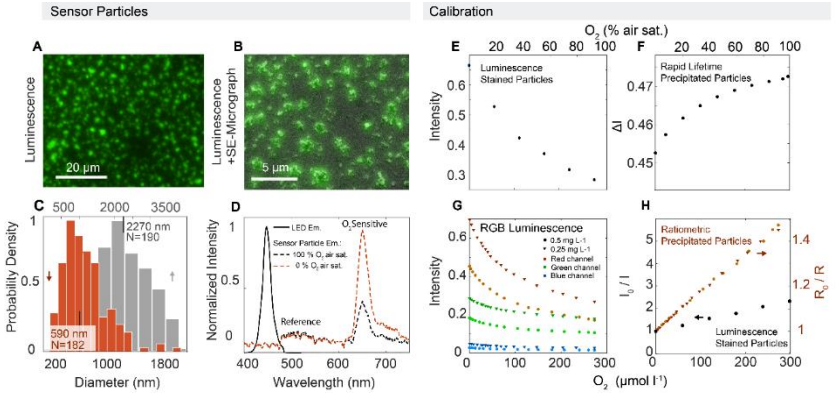

Figure 01: Characterization of the sensor particles. a O_2-sensitive sensor particles excited by blue wavelengths (365-440 nm) emit green and red fluorescence (500-650 nm). **b** Scanning electron micrographs of the same sensor particles as in **(a)** overlaid with the fluorescent signal. **c** Size spectrum analysis reveals that sensor particle sizes range between 200 and 1800 nm (median = 590 nm) for precipitated particles (orange) and 500-4000 nm (median = 2270 nm) for stained particles (gray). **d** Excitation and emission spectra of O_2-sensitive dye Platinum(II) meso- (2,3,4,5,6-pentafluoro)phenyl porphyrin) (PtTFPP). Dashed lines indicate the emission of the O_2-sensitive dye (red) and reference dye (black) and the solid black line indicates the emission spectrum of PtTFPP. **e** The luminescence intensity of stained particles based on the intensity of the camera pixel and **f** Rapid lifetime measurement of precipitated particles as a function of O_2 concentrations. **g** Luminescence imaging of precipitated ratiometric sensPIV particles with an RGB camera. Note that as a result of the spectral overlap between channels, the green channel also exhibits a slight O_2 dependency. The concentrations of 0.5 mg L^{-1} (red, triangles) and 0.25 mg L^{-1} (orange, round) refer to the tested sensor particle concentrations. **h** Calibration curve for two types of sensor particles at different concentrations of O_2. Orange/red colors denote

particles produced via precipitation (0.5 mg L^{-1}: red, triangles; 0.25 mg L^{-1}.: orange circles) and black colors denote particles produced via staining methods.

To synthesize suitable particles for sensPIV, we explored two methods i) a precipitation method (Mistlberger et al., 2010) and ii) a staining method that uses commercially available particles (diameter of 2.3 µm, Figure 01a-d and Supplementary Figure 01a). Precipitation is a straightforward process where an indicator dye (PtTFPP), a reference dye (macrolex fluorescence yellow 10GN) and a polymer (styrene maleic anhydride) are dissolved in a solvent (tetrahydrofuran) that is well miscible with water (see methods). As dyes and the polymer are water insoluble, precipitation of dye- containing particles (size 200 nm -1800 nm) occurs instantaneously when mixed with water (Figure 01a-c, Supplementary Figure 01a). To prevent particle aggregation, we used a copolymer of styrene and maleic anhydride. During precipitation, the anhydride groups are hydrolyzed and the resulting carbonic acid groups on the surface stabilize the particles (see (Mistlberger et al., 2010) for tuning possibilities of nano-particles). The main advantage of precipitation is the possibility of producing large amounts of sensor particles with minimal effort and virtually no specialized equipment. In contrast to precipitation, the staining method uses commercially available synthetic particles which are exposed to a mixture of an organic solvent (here acetone) and water with added O_2 indicator PtTFPP (Borisov et al., 2008). Particles immersed in this mixture swell and entrap lipophilic dyes within the particles when the organic solvent evaporates.

Notably, both synthesis methods produce particles that contain a range of different particle sizes (Figure 01c, 590 ± 360 nm (SD) by precipitation and 2270 ± 1960 nm by staining) and, in order to suppress variability in particle sizes, we

developed a protocol consisting of a series of sonication, centrifugation and subsequent filtration steps (described in methods and Supplementary Figure 01b). We found that despite inhomogeneous particle sizes, a simple two-point calibration is sufficient for accurate O_2 measurements via sensPIV (Figure 01e-h).

Excitation and imaging of sensPIV particles

Quantifying the O_2-dependent phosphorescence (Klimant et al., 1995; Morris et al., 1993) of nano- and micrometer-sized sensPIV particles requires microscale visualization. In this study, we examined sensPIV particles via epifluorescence microscopy or light-sheet microscopy (Figure 02a-c). Standard epifluorescence microscopes can be readily adapted for sensPIV measurements, either by using existing laser- or diode-based light sources to excite PtTFPP (Ex. ~ 390 nm), or by adding a specific fluorescence filter cube (e.g., Ex. ~ 390 nm, Em. > 490 nm) when using full-spectrum light sources (Figure 02a-c). Epifluorescence microscopes are available in many research environments and are well suited to perform sensPIV in well-defined experimental setups (e.g., microfluidic applications). Compared to epifluorescence microscopy, light-sheet microscopy can be used to image sensPIV particles around larger 3D objects (mm-cm scale), or in experimental setups that require additional instrumentation, such as flow-chambers. Light-sheet microscopy, however, requires high light intensities and a homogeneous illumination field, which is achievable only with high power LED systems with an output ranging between 2.5 W to 5 W or with laser diodes (see methods section).

Simultaneously recording fluid movement and local O_2 concentration via sensPIV particles requires fast cameras (> 10 Hz for the applied test cases) in order to capture the luminescence of rapidly moving particles. Capturing differences in luminescence is achieved via three imaging modalities, i) luminescence imaging (Figure 02a), ii) ratiometric imaging (Figure 02b) and iii) rapid lifetime imaging (Figure 02c). In its simplest form, sensPIV can be executed by recording the

luminescence intensity of sensor particles with a simple monochromatic camera. Such cameras are characterized by high quantum efficiencies which allow for lower excitation intensities and faster recording frequencies (> 100 Hz). However, the accuracy of measurements with monochromatic cameras is usually limited by the homogeneity of the illumination which may be affected through shading when observed samples exhibit 3-dimensionality. In our proof-of-concept applications, we demonstrate that effects of inhomogeneous excitation light can be avoided by performing in situ calibrations of sensor particles in simplified, controlled environments (such as microfluidic devices, see test case 1), or by using alternative imaging methods (such as ratiometric or rapid lifetime imaging) that record the light used for excitation at the same time as the emission light, thereby enabling instantaneous referencing.

Ratiometric imaging takes advantage of two luminescent dyes present within the same sensPIV particle to obtain a ratio of luminescence signals. One dye serves as the O_2-sensitive indicator while the second O_2-insensitive dye acts as a reference. Normalizing the intensity of the O_2-sensitive dye with the reference intensity compensates for inhomogeneous illumination fields, particle sizes and artefacts introduced by topographic features (see (Koren et al., 2015) and references therein). Ideally, ratiometric dyes cover two colors of the RGB chip installed in many commercially cameras, which allows for convenient sensPIV measurements by taking a single image. In our experiments, we optimized the synthesis of PtTFPP sensor particles for ratiometric sensPIV (see above and supplementary information, test case 3 for application). The O_2-sensitive compound PtTFPP (Em. peak at ~650 nm) in combination with the reference dye Macrolex fluorescent yellow 10GN (MY, Em. peak at ~480 nm) yields optimal performance in combination with standard RGB cameras (see also (Koren et al., 2015)). Notably, MY does not only act as a reference dye but also acts as an antenna molecule that transfers excitation energy to PtTFPP and thereby increases sensor brightness via

light-harvesting effects (see (Mayr et al., 2009)). Instead of less powerful green or potentially harmful UV LEDs, which target the specific absorbance spectra of PtTFPP, it is therefore possible to work with less harmful and bright blue LEDs.

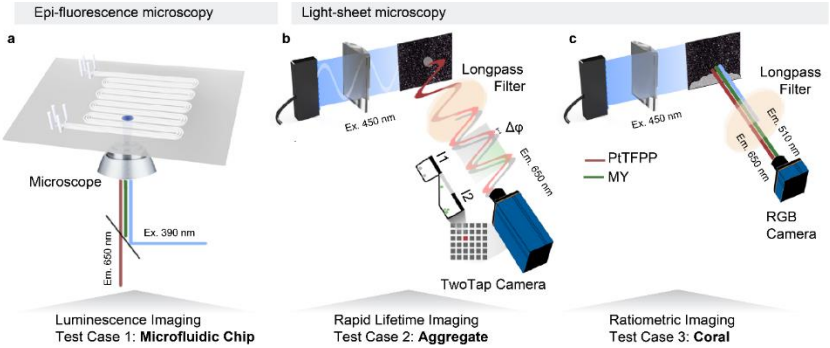

Figure 02: Conceptual illustration of the three imaging approaches compatible with sensPIV and used within this study. **a** Luminescence intensity imaging: here UV light (~390 nm) is used to excite the O_2 -sensitive dye (PtTFPP) on sensPIV particles. The resulting red-shifted (>650 nm) luminescence intensity depends on ambient O_2 concentrations. This approach is achievable using a simple epifluorescence microscope. **b** Rapid lifetime imaging: here sensPIV particles are excited with an intensity modulated light sheet (~450 nm) and the luminescence (~650 nm) emitted by sensor particles is phase shifted. The resulting phase shift $\Delta\varphi$ depends on the O_2 concentration and is estimated based on a two-tap camera chip (see methods). **c** Ratiometric imaging: here blue light (~450 nm) is used to excite both PtTFPP (via energy transfer, see text) and the reference dye, MY. The emission of the PtTFPP (red, R, ~650 nm) is normalized by the emission of MY (green, G, ~500 nm) which compensates for inhomogeneous illumination and simplifies calibration.

To measure dissolved O_2 concentrations without addition of a reference dye, luminescent lifetime imaging is the method of choice (Murniati et al., 2016). The luminescence lifetime is the mean time between activation of a molecule and photon emission and is characteristic for every luminophore. The lifetime of the O_2-sensitive PtTFPP (~60 µs without O_2) can be estimated via repeated imaging of the declining luminescence intensity after light exposure (see (Koren et al., 2019)). However, for typical shutter-modulated cameras, readout times are on the order of 10-100 s due to relatively slow sensors. Newer cameras allow for estimating the lifetime (τ) in the frequency domain based on the frequency-shift (see Key Resources Table and Methods) and can capture lifetime images in less than 10 s (Koren et al., 2019). In order to meet the requirements for sensPIV (recording frequencies > 10 Hz) we performed rapid lifetime measurements with a camera-chip (QMFLIM2, pco) that has an in-pixel charge swing separating two taps within each pixel (Chen et al., 2015). The in-pixel charge swing allows quasi-instantaneous recording of two sequential images (I_{T1}, I_{T2}) where each image covers half the period of the excitation signal (5 kHz, see Figure 02). The normalized intensity difference of the two images $\Delta I = (I_{T1} - I_{T2}) / (I_{T1} + I_{T2})$ is directly related to the dissolved-O_2 concentration (see Figure 02c). The advantage of lifetime imaging is that only one O_2-sensitive dye is needed and highly accurate measurements are achievable even in heterogeneous samples (see test case 2 for application). The main disadvantages of this method are, i) the relatively high cost of the camera system and ii) that measured signals do not scale linearly (Figure 01f) which requires the application of a second order polynomial fit (see methods).

Applications of sensPIV

SensPIV under well-defined O_2 gradients within microfluidic devices

Microfluidic chambers are ideal testing arenas for sensPIV as they provide a high level of control over fluid flows, O_2 concentrations and imaging of microscale processes (Son et al., 2015). Owing to the importance of viscosity at small scales, fluid flows in microfluidic channels are laminar and exact mathematical solutions allow for robust calibration of flow measurements in prototypical channel geometries like rectangular channels (Batchelor, 1967). Moreover, specific O_2 concentrations can be controlled and varied over time (Garren et al., 2014; Rusconi et al., 2014; Yawata et al., 2014). These characteristics make microfluidic devices useful for biological and medical applications, including the study of bacterial aerotaxis and measuring O_2-dependent cellular responses (Menolascina et al., 2017). Here we used microfluidic devices to carefully calibrate sensPIV particles and to demonstrate accurate, simultaneous visualization of fluid flows and O_2 concentrations.

First, we introduced sensPIV particles into a polydimethylsiloxane (PDMS) microfluidic device consisting of a main fluid channel surrounded by two adjacent gas channels (Figure 03a). As PDMS is gas-permeable, we can control dissolved O_2 concentrations in the main fluid channel containing sensPIV particles. To calibrate sensPIV particles, we equilibrated the fluid in the main channel first with compressed air (21% O_2) and then with nitrogen gas (0% O_2) while measuring the luminescence intensity of particles under no flow. Following this two-point calibration, we supplied compressed air to one of the gas channels and nitrogen gas to the other, ultimately resulting in a steady linear O_2 gradient across the main channel. By relating the luminescence intensity of individual sensPIV particles to a previously obtained calibration curve, we could observe the evolution of O_2 concentrations across the main channel (Figure 03b), as the system transitioned to the steady linear profile. This allowed us to compare our experimental O_2

measurements with a time-resolved numerical model solving the scalar transport equations (Figure 03b, see methods section). This revealed that experimental O_2 concentrations reached equilibrium after 70-100 seconds, which is consistent with diffusion time scales derived from our model. Experimental data and model results were in good agreement and demonstrated correlation-coefficients (R) between 0.75-0.82 (Figure 03b, 1 indicating good positive correlation, Supplementary Tab. 1). Dissimilarities between model results and experimental results occurred during the initialization of experiments, an observation we attribute to the capacity of PDMS to retain gases and the difference in the time required for gases to be released. Together, these experiments demonstrate that stationary sensPIV particles can visualize steady-state, and dynamically changing O_2 concentrations in simple microfluidic geometries.

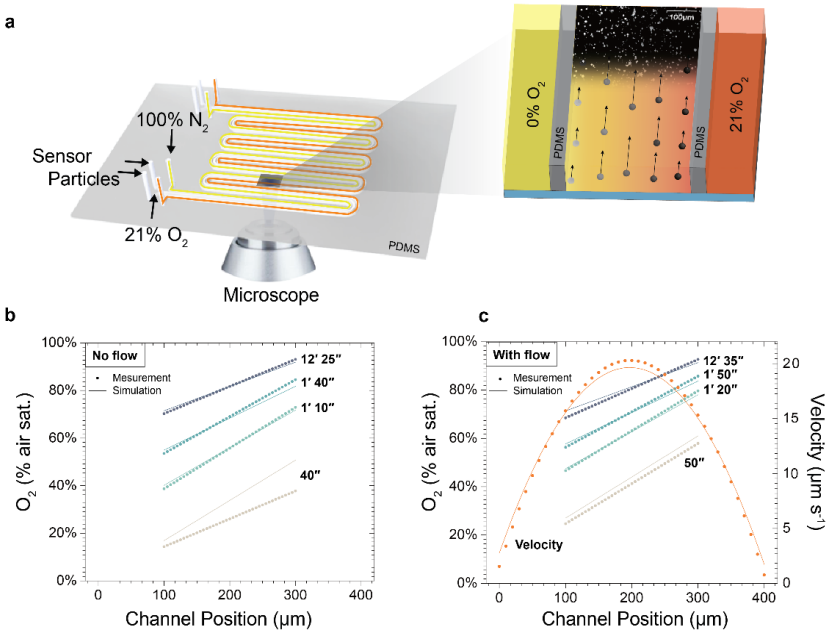

Figure 03: The behavior of sensPIV particles in a simple microfluidic device with a well-defined linear O_2 profile. a Cross-section of the microfluidic device used to control the gas environment around sensPIV particles. The microfluidic device was adapted from (Rusconi et al., 2014) and consists of a central fluidic channel surrounded by two (gas) side channels. Injecting 100% N_2 (= 0% O_2) into one of the gas channels and compressed air (= 21% O_2) into the other resulted in a linear O_2 gradient across the central fluidic channel containing sensPIV particles. **b** O_2 profiles in no flow conditions. Here sensPIV particles were introduced into the main channel and kept quiescent. Shown are sensPIV measurements (dotted lines) and model simulations (solid lines) at time 40 s, 1 min 10 s,1 min 40 s and 12 min 25 s. **c** O_2 profiles under flow conditions. Here sensPIV particles were continuously introduced into the main fluidic channel at a flow velocity of 11 µm s^{-1}. Comparison between sensPIV measurements and model simulations at 50 s, 1

min 20 s,1 min 50 s and 12 min 35 s (correlation coefficients are presented in Supplementary Tab. 1).

Second, to determine whether sensPIV particles can accurately visualize transport processes and O_2 concentrations simultaneously, we used the same microfluidic device to control both O_2 concentrations and particle velocities in the main channel. At an average flow speed of 11 μm s^{-1} in the fluid channel and a compressed gas supply of 21% O_2 and 0% O_2 to the gas channels, we tracked and measured the intensity of sensPIV particles to simultaneously determine flow fields and local O_2 concentrations (Figure 03c). This enabled us to derive the characteristic flow field in the main channel (a parabolic shape) and concurrently visualize the developing gradients of O_2. Experimental data on flow fields and local O_2 concentrations largely matched numerical modeling outputs (Figure 03c, $R_{velocity}$= 0.83, $R_{gradient}$ = 0.79-0.84, Supplementary Tab. 1) and demonstrated that the equilibrium profile was attained after approximately 80-110 seconds.

SensPIV for measuring the dynamic O_2 exchange around a model laboratory aggregate.

Sedimentation of particles, flocs or aggregates is a process occurring in both natural and industrial settings, including particulate matter transport in the ocean and deposition in wastewater treatment plants. In organic aggregates, the high carbon content and associated microbial activity leads to the formation of distinct microenvironments. When respiration exhausts O_2 inside aggregates (Ploug, 2001), anaerobic processes are favored (e.g., denitrification and anammox) resulting in the enhanced removal of nutrients in wastewater treatment plants (Speth et al., 2016) and the ocean (Bianchi et al., 2018; Karthäuser et al., 2021). Inside aggregates, the duration and extent of O_2 depletion is governed by the external supply of O_2 and its transport through the aggregate boundary layer. The thickness of the aggregate boundary layer controls O_2 fluxes into aggregates and

is highly dependent on the surrounding flow field. Here we used sensPIV to quantitatively assess the O_2 exchange processes around, and into millimeter-sized aggregates. For this, we synthesized porous agarose aggregates (porosity, i.e. the ratio of voids to total volume, $\theta = 0.97 \pm 0.01$, radius, $r = 2.7 \pm 0.1$ mm, $n = 6$) with embedded sensor particles (produced via the precipitation method). To simulate an O_2-depleted aggregate, agarose aggregate were degassed and placed into a temperature-compensated flow chamber (Figure 04a) to simulate sinking. Two separate experiments were performed in which the aggregate was exposed to a flow of 2.1 mm s^{-1}, representing a Reynolds number of approximately 1, and a reference experiment with no flow.

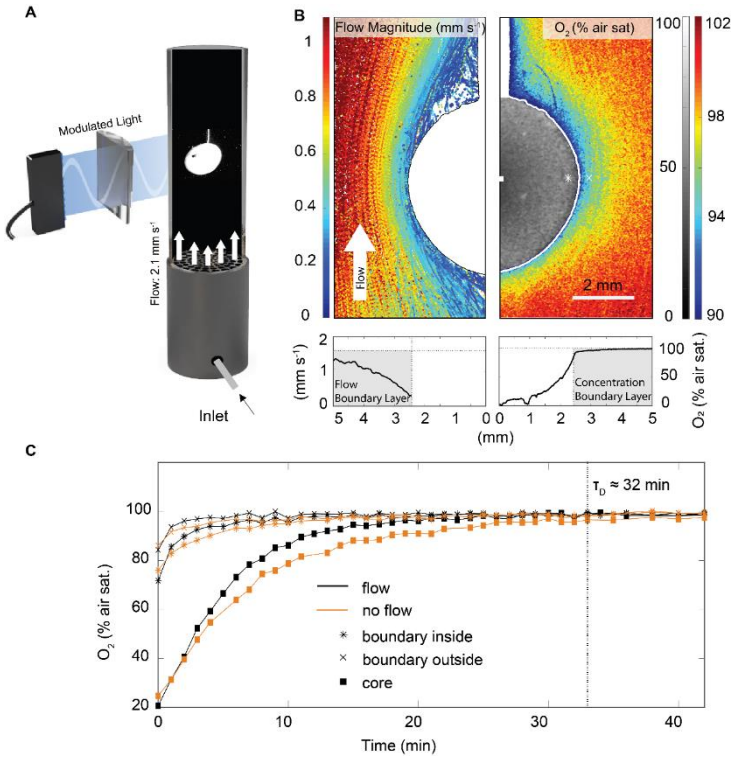

Figure 04: sensPIV visualizes flow and O_2 gradients around and inside a porous agarose aggregate. a Conceptual illustration of the experimental setup consisting of a flow chamber, an agarose sphere with embedded sensor particles and the imaging setup. **b** Reconstruction of the flow field (left panel) and O_2 concentration inside and around the aggregate (right panel). Note the different scale bars for the O_2 concentration inside and outside the aggregate (see also text). Lower panels indicate flow and O_2 profile along the equator of the aggregate. **c** Transient O_2 concentrations in the core, at the surface and in the boundary layer

of a aggregate under flow and no-flow conditions. Diffusion timescale τ_D is estimated from the radius of the aggregate and the diffusion of O_2 (see text).

In both experiments, the O_2 boundary layer surrounding the aggregate and the O_2 concentration inside the aggregate was visualized by taking a total of 100 images via rapid lifetime imaging (frequency of 10 Hz, Figure 04b). Flow fields were reconstructed by PTV (Supplementary Figure 02) and O_2 concentrations were estimated by relating the difference of two intensity images to a calibration curve (Figure 01f, see also Supplementary Figure 03). High-resolution sensPIV images revealed a 2.5 mm-thick O_2 boundary layer surrounding the aggregate and O_2 concentrations that rapidly decrease from 100% to 90% air saturation in the vicinity of the aggregate surface. The shape of the O_2 boundary layer is narrow on the upstream side and then asymmetrically increases in size towards the downstream side, together confirming previous microsensor-based measurements (Ploug, 2001). We note that while microsensors provides comparable information, sensPIV measures O_2 transport processes in 2-dimensions without disturbing flow fields (see also Supplementary Figure 04).

We next examined the impact of flow on the transfer of O_2 from the aggregate exterior into its interior. To better understand this process, we estimated the diffusion timescale of O_2 into the aggregate ($\tau_D = a^2 D^{-1}$ = 32 min) which qualitatively matched our experimental results with sensPIV (= 30 min). However, the direct comparison of flow (velocity of 2.1 mm s^{-1}) with no-flow conditions revealed an enhanced diffusion of O_2 into the aggregate core by more than 8% (measured after 10 min). To quantify this enhancement effect, we evaluated the O_2 fluxes, *J*, through the exterior of the aggregate by calculating the concentration gradient perpendicular to the surface under flow and no-flow conditions. To account for the asymmetry of O_2 concentrations induced by flow fields, all O_2 gradients were averaged along the whole surface of the aggregate following:

$$J = -\frac{\theta D}{A} \int \vec{n} \cdot \nabla C \, dA$$

where D is the diffusion coefficient of O_2, θ the porosity of the aggregate, $\vec{n}$ is the unit normal vector perpendicular to the surface of the aggregate (*A)* resulting in a surface O_2 concentration gradient $\vec{n} \cdot \nabla C$.

After initiating flow, the fluxes of O_2 into the anoxic aggregate core were between 1.3-1.8 nmol cm^{-2} s^{-1} and declined over time as the aggregate saturated with O_2 (compare Figure 04d). We extracted the fluxes for a given O_2 concentration inside the aggregate and expressed the flow-dependent uptake enhancement as the Sherwood number, which is the ratio of the flux in the presence of flow to the flux in the absence of flow. For the aggregate case, we found an average Sherwood number of 1.75, implying that the fluid flow increased O_2 exchange by 75% compared to no-flow conditions. This number only represents a single test case and strongly depends on the ratio of settling velocity timescales and diffusion timescales. Previous modelling studies have estimated the uptake enhancement to be about ten times greater for the same spherical aggregate shape and flow regime (Kiørboe & Thygesen, 2001). We attribute this difference to the fact that most models do not take into account aggregate porosity and apply simplified boundary conditions (Moradi et al., 2018). Our visualization of aggregate-fluid exchange processes under flow conditions thus demonstrates the importance of experimentally verifying numerical models. SensPIV is suited to address this challenge and to elucidate how the presence of flow and metabolic activity shapes O_2 gradients.

SensPIV for the visualization of O_2 dynamics and cilia-induced flows around the coral *Porites lutea.*

Cilia are hair-like structures present in many motile microorganisms, but also humans and other mammals (Sleigh, 1962; Wan, 2018). A key function of cilia is to initiate fluid motion to propel organisms or to enhance ventilation across surfaces (Gilpin et al., 2020). In a final experiment, sensPIV was used to investigate the microscale interaction of epidermal cilia on a reef-building coral with its surrounding flow environment. Previous studies on coral flow fields demonstrated that the beating of epidermal cilia stirs the boundary layer and enhances mass transport (Shapiro et al., 2014). However, due to methodological limitations, it was not fully understood how the flow field generated by cilia affects the O_2 concentrations within the coral boundary layer and what benefit the coral derives from this.

Here, we used the stony coral *Porites lutea* as a model organism and measured sensPIV particles around its surface through a recently developed light-sheet microscope and recirculating flow chamber (Pacherres et al., 2020). First, we tested the biocompatibility of sensPIV particles by adding particles and observing coral cilia beating for 5 minutes during stroboscopic light exposures (20 ms each). The introduction of sensPIV did not visibly induce coral bleaching nor change the beating of cilia, but induced substantial mucus production as previously observed under light stress (Fabricius-Dyg et al., 2012; Koren et al., 2016). After experiments, coral fragments were visually inspected for several days and no substantial release of zooxanthellae was detected. Finally, we tested the effects of continuous illumination by exposing a coral fragment to light for two minutes, a duration that is 60-times longer than the total illumination time used in experiments. Prolonged light exposure caused the release of endosymbionts and bleaching of the coral fragments exposed to light. These experiments suggest that sensPIV particles are biocompatible as long as light and particle exposure are

minimized. In all subsequent experiments, this was achieved by using short light strobes (≤ 20 ms) and removing sensor particles after finishing experiments (~1 min).

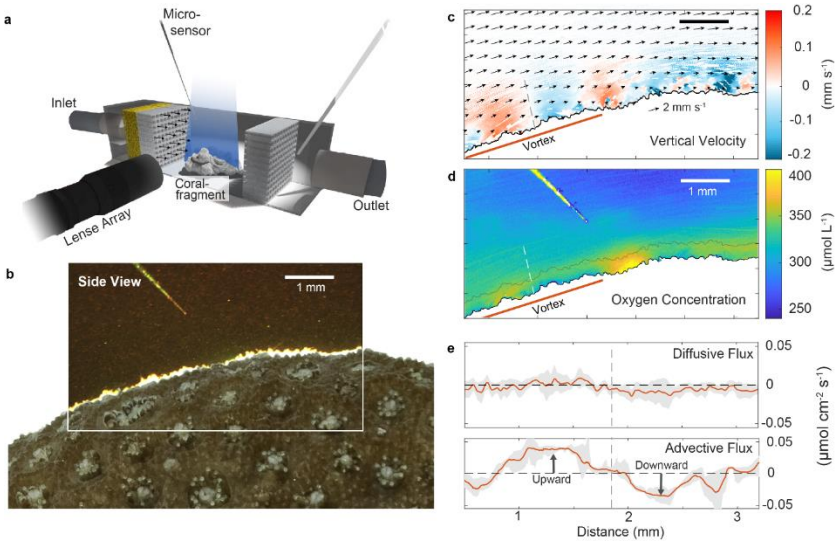

Figure 05: sensPIV can visualize flow and O_2 around corals and other complex biological structures. a A custom light-sheet microscope based flow chamber setup containing an actively stirring coral specimen (*Porites lutea,* see SV1 for video). **b** Color image of sensPIV particles around the coral surface. Note the O_2 microsensor in the top left corner which is used to cross-reference measurements. **c** Combined particle image velocimetry (PIV) and particle tracking velocimetry (PTV) graph of sensPIV particles. Arrows indicate the flow along the coral´s surface, as determined by PIV using the red channel of the RGB image. Colored dots represent individual particles and the color indicates the velocity

component perpendicular to the coral surface as determined by PTV. Red and blue depict upward and downward flow of particles. **d** sensPIV-derived O_2 concentrations inside the coral boundary layer. **e** Diffusive and advective O_2 fluxes normal to the surface along the vortex area highlighted in (**d)**. The advective flux perpendicular to the surface was averaged for the first 250 μm above the coral surface along the red line and the upper limit is indicated by a gray line in **d**.

To visualize O_2 concentrations around *P. lutea*, we introduced sensPIV particles and recorded 100 color images within a time window of two seconds (see also Supplementary Video 2). Based on these images, we reconstructed the O_2 concentration using a ratiometric-referencing approach with the red (R) and green (G) channels of the color image (Figure 04a,b). We found that single images can reconstruct O_2 concentrations with an error of approximately 10% - 15%, and that additional images (n > 40) reduced the error to below 2 % (see Supplementary Figure 04). To compare the accuracy of sensPIV with the accuracy of a 'traditional' amperometric microsensor, individual vertical profiles were extracted from sensPIV measurements and O_2 concentrations were found to change by $\Delta C = 1.5$ µmol L^{-1} over a distance of $\sim \Delta z = 20$ µm which is close to the resolution of commercially available O_2 microsensors (see Supplementary Figure 05). However, while both methods capture similar O_2 concentrations, microsensors are able to resolve more pronounced gradients. We attribute this to the fact that the sensPIV experiments were performed at oversaturated O_2 concentrations in the range of 240-650 µmol L^{-1} (Nelson & Altieri, 2019). At this concentration range the phosphorescence of O_2 sensor particles is already substantially quenched as illustrated by the sensor calibration (Figure 01g). At an O_2 saturation of 0%, a 10% change of O_2 results in a signal change of 7%, while at 100% O_2 saturation, a 10% change of O_2 results in a signal change of 1%. PtTFPP thus appear best suited for low-O_2 conditions and better accuracies at high O_2 concentrations could be achieved with iridium or ruthenium-based dyes (Quaranta et al., 2012).

The sensPIV analysis of O_2 concentrations revealed a boundary layer along the coral surface with a width of approximately 1300 ± 300 µm (Figure 04d, Supplementary Figure 05c) and characterized by large heterogeneities in both horizontal and vertical directions. Two distinct semi-circular shaped vortices indicated local increases in O_2 production at the coral surface (Figure 04d). The

width of the vortices varied between 800 µm and 1500 µm and extended 900 ± 300 µm into the flow field thus traversing almost the entire boundary layer (Figure 04d). The flow field (black arrows in Figure 04c) in the vicinity of the coral exhibited complex pulsed movements that were insufficiently captured by averaged image ensembles. To improve the visualization of these vortical flows, the velocity perpendicular to the coral surface was calculated via PTV (Figure 04c). This demonstrated that vertical velocities ranged from -0.1 to 0.1 mm s^{-1} and the width of each of the vortices was 1000 - 1250 µm (compare also Supplementary Figure 05 d).

A comparison of O_2 concentrations and flow fields suggest that upward-directed fluid motion, induced by cilia, coincide with zones of higher O_2 concentrations while downwelling flows coincide with lower O_2 concentrations. This implies that cilia are not stirring the entire boundary layer homogeneously as assumed previously (Shapiro et al., 2014), but likely organize their beating pattern to increase the upward transport of excess O_2 from the tissue. O_2 is also transported downwards towards the mouth openings (Pacherres et al., in review) where the coral actively respires. SensPIV has thus helped reveal that the coral actively stirs the boundary layer in order to externally link zones of O_2 production with zones of O_2 consumption and, presumably, accelerate metabolism. To quantify this transport effect, we calculated the advective flux of O_2 as

$$J_{adv} = u_{\perp} C$$

and diffusive flux as

$$J_{diff} = - D \vec{n} \cdot \nabla C$$

Where $u_{\perp}$ is the velocity perpendicular to the surface and C is the O_2 concentration. The advective flux of O_2 was averaged for the first 250 µm above the coral surface and ranged from -36 nmol cm^{-2} s^{-1} to 38 nmol cm^{-2} s^{-1} (negative sign implies downward pointing flux). Averaging along the vortex, the net upward flux is 1.5 nmol cm^{-2} s^{-1}. In comparison, the net diffusive flux (averaged along the whole coral surface) is 0.4 nmol cm^{-2} s^{-1}. The dominance of advection over diffusion can be tested using the non-dimensional Peclet number (Pe$\sim u_{\perp}L/D$), where L is the characteristic length scale of the vortices (L$\sim$1000 mm). For the present coral, the Peclet number was calculated to be approximately 100, confirming the ratio of the measured advective to diffusive fluxes of $\sim$ 95. In conclusion, the dominance of advective fluxes implies a substantial consumption of photosynthetically produced O_2 through respiration at the mouth openings.

Discussion

SensPIV links microscale measurements of flow, traditionally performed via PIV, with measurements of O_2 concentration, typically performed with microsensors or immobilized optodes. Here we demonstrate the ability of sensPIV to simultaneously measure flow fields and O_2 concentrations. Our three test cases demonstrated the power of sensPIV to study microscale advective and diffusive fluxes in experiments at varying complexity. These applications show the simple implementation of sensPIV for experimental research ranging from ecology, to life-sciences and engineering. Using sensPIV, we obtained insight into how corals optimize O_2 consumption and production by measuring their advective ciliary flow. Previously, heterogeneous nutrient and O_2 concentrations within the boundary layer of corals were attributed to changes in coral topography and the resulting variations in concentration boundary layer thicknesses (de Beer et al., 2000). Using sensPIV, we instead discovered that coral topography acts in tandem with local ciliary flow to enhance removal of O_2 from coral tissues and, at the same

time, optimize the coral metabolism. While further research is needed to disentangle the complex interactions occurring on coral surfaces, our initial results emphasize the ability of sensPIV to provide insights into mass-flow exchange around complex biological structures. Although we only present results from the coral species *Porites lutea*, we emphasize that cilia are found in many biological systems such as in the human respiratory tract (Loiseau et al., 2020) and the oviduct of female mammals (Byatt-Smith et al., 1991; Enuka et al., 2012). In these examples, the transport of O_2 might play a key role in the clearance of particles and pathogens and for supplying O_2 to embryos which could be studied using sensPIV.

Notably, sensPIV (in its most basic form) only requires simple setups (see Key Resources Table) making this technology accessible to the research community at low cost. We thus anticipate the integration of sensPIV into a range of existing microscopy platforms (e.g. light-sheet microscopy (Krzic et al., 2012)) or into aquatic in situ laser scanning instruments for measurements of O_2 and flow fields (e.g. (Ahmerkamp et al., 2017; Katija & Dabiri, 2008; Liao et al., 2009)). Moreover, engineering and medical research may also profit from sensPIV as a tool to study transport of O_2 in bioreactors (Seidel et al., 2021), for aerodynamic pressure measurements (Gregory et al., 2008), when measuring the transfer efficiency of O_2 to tissue cells (Bein et al., 2018) or even to discriminate pO_2 in cell populations via flow-cytometry (e.g. (Koch, 2002)). To date, most studies that estimate the effect of flow on O_2 fluxes have been performed using numerical models (Ahmerkamp et al., 2015; Broomé et al., 2013; Moradi et al., 2018). However, these models are abstract versions of reality, rely on simplified system geometries and boundary conditions, usually assume immobile objects, and typically discount microscale heterogeneities in flow and O_2 concentrations. By applying sensPIV to sinking agarose aggregates, we revealed the bias resulting from model oversimplifications and highlighted the need to include the porosity of aggregates for more realistic

predictions. In the future, sensPIV could probe the influence of the spatial organization of microorganisms inside particles and their exchange with ambient flow and chemistry. Moreover, the combination of numerical simulations with sensPIV experiments could provide powerful insights into the complex coupling between flow, metabolic rates and exchange fluxes. Our model aggregates (test case 2) also serve as analogs of other motile 'particles' such as synthetic microswimmers or motile microorganisms and could facilitate measurements of O_2 'trails' around individual cells (Guasto et al., 2012; Kanso et al., 2021) and to study the collective mixing of suspensions of microorganisms (Sommer et al., 2017). Applying sensPIV in more complex flow setups will enable the study of planktonic organisms (Krishnamurthy et al., 2020) and their single cell heterogeneity (Behrendt et al., 2020). Understanding the dynamics underlying these processes could lead to novel insights into how organisms interact with their microscale environment.

Finally, sensPIV is not limited to measurements of O_2 but can in principle also measure an increasing number of other analytes - including pH, CO_2, temperature and NH_3 (Merl & Koren, 2020; Moßhammer et al., 2019). Our sensPIV data on corals emphasizes the need for measuring spatially separated zones of production and consumption to understand the distribution of metabolites across complex shapes. The exchange processes between coral endosymbionts and the coral animal in the boundary layer likely apply to nutrient distributions and chemical solutes in addition to O_2. The integration of other chemical sensors into sensPIV could provide important insights into the interplay between remineralization processes and flow at the scale of individual organisms.

Limitations of the Study

SensPIV has limitations which are related to current imaging technologies and synthesis of sensor particles. The spatial resolution of sensPIV is mainly limited

by the size of particles and the ability of cameras to discern them as individuals. In our test-cases, the smallest visible sensor particles had a median diameter of 500 nm. Consequently this set the resolution for resolving spatial gradients in the range of 1-10 micrometer. For intracellular studies, where a resolution far below 1 µm is required and diffusion timescales dominate, other methods thus far surpass the ability of sensPIV to measure O_2 (e.g. Okkelman et al., 2020; Zhdanov et al., 2015). The strength of sensPIV is its ability to image flow-fields and concentrations simultaneously at a resolution that is close to microsensors. However, if the effects of flow fields are negligible and/or O_2 gradients are one-dimensional, traditional microsensors still outperform sensPIV in relation to spatial resolution and accuracy.

Further, if sensPIV is applied to autofluorescent organisms (e.g. phototrophs), their natural fluorescence can interfere with the luminescence signal emitted by sensPIV particles. This limitation can be overcome by using O_2 sensitive dyes which are excited in the deep red or near-infrared range and thereby avoid autofluorescence spillover from photopigments (e.g. Niedermair et al., 2010). If information on O_2 concentrations within the tissue are of interest, confocal laser scanning microscopy or two-photon phosphorescence lifetime microscopy may be a powerful alternative to sensPIV (see e.g. Moritomo et al., 2016; Shen et al., 2018). Finally, during the synthesis of sensor particles, the amount of dye embedded within individual sensor particles can vary. This can affect luminescence intensities and the ratiometric signal at constant O_2 concentrations (visible in figure Supplementary Figure 03b) and requires compensation by averaging spatially, or across image ensembles. Particle synthesis can also be improved through the covalent coupling of PtTFPP and the reference dye (e.g. Koren et al., 2012), resulting in improved resonance energy transfer and an improved referencing in ratiometric imaging approaches.

Acknowledgements

We thank Volker Meyer, Paul Faerber and Gerhard Holst for technical support. We thank Claudio Richter for providing the coral *Porites lutea*. We thank Sina Schorn, Bram Vekeman and Juliane Schoetz for support in the laboratory. We thank Dirk de Beer for valuable discussions and comments. D.R.B. was supported by an Australian Research Council (ARC) Discovery Early Career Researcher Award DE180100911, and a Gordon & Betty Moore Foundation Symbiosis in Aquatic Systems grant. C.O.P. acknowledges funding from the Helmholtz Association (Alfred Wegener Institute, Helmholtz Centre for Polar and Marine Research). F.M.J received funding from the Cluster of Excellence "The Ocean Floor—Earth's Uncharted Interface" (Germany's Excellence Strategy-EXC-2077-390741603 of the DFG). L.B. and Y.C. were supported by grants from the Swedish Research Council (2019-04401) and the Science for Life Laboratory. R.S. acknowledges funding from the Simons Foundation through the Principles of Microbial Ecosystems (PriME) Collaborative (grant 542395). K.K. acknowledges financial support by research grants from the Grundfos Foundation and a Sapere Aude grant from the Independent Research Fund Denmark (IRFD): DFF-8048-00057B. The study was funded by the Max Planck Society (MPG) through the "Multiscale Approach on the Role of Marine Aggregates" (MARMA) project.

Star Methods

Resource Availability

Lead contact

Further information and requests for resources and reagents should be directed to and will be fulfilled by the lead contact, Soeren Ahmerkamp (sahmerka@mpi-bremen.de).

Materials availability

This study did not generate new unique reagents.

Data and Code availability

- All data reported in this paper will be shared by the lead contact upon request. Raw data is available in the supplementary information and as supplementary videos
- Links to programs and codes are provided in the Key Resources Table (DOI: 10.6084/m9.figshare.19614273.v1).
- Any additional information required to reanalyze the data reported in this paper is available from the lead contact upon request.

Experimental Model and Subject Details

Porites lutea colonies reared at the aquaria facilities of the Alfred Wegener Institute were used as fragment source. The colonies were kept in artificial seawater (salinity 32.6 ± 0.26) (Dupla Marine Premium Reef Salt Natural Balance), under 25.2 ± 0.07 °C temperature, a 12-h light-dark cycle, light intensity of 75 and 80 µmol quanta m^{-2} s^{-1} (LI-COR LI-192, USA) and pH of 7.9 ± 0.09 (YSI, USA). Food was provided in the form of freshly hatched *Artemia nauplii* every second day. Before the start of the experiments small fragments (1.5 cm long, 1 cm wide) were cut out from the source colonies and allowed to heal for at least two weeks in the culturing tank.

Detailed Method

Sensor Particle Production

For ratiometric and lifetime imaging, sensor particles were prepared as described earlier via precipitation (Koren et al., 2015, 2016; Mistlberger et al., 2010) with minor specific modifications as described in the following. Briefly, 100 mg of the polymer PSMA (styrene maleic anhydride copolymer with 8% MA, Mw: 250000 g mol^{-1}; generously provided by Polyscope), 1.5 mg of the reference dye Macrolex fluorescence yellow 10GN (MY) obtained from Lanxess (Köln, Germany) and 1.5 mg of the O_2 indicator Platinum(II) meso- (2,3,4,5,6-pentafluoro)phenyl porphyrin (PtTFPP, Frontier Scientific) were dissolved in 10 g of tetrahydrofuran (THF). This solution was then rapidly poured into 200 mL of vigorously stirred MQ water. After evaporating the THF under an airstream, the particle suspension was further concentrated at elevated temperature (around 60 °C) until a concentration of 5 mg mL^{-1} was reached. The final concentration was measured by drying and subsequent weighing of 1 mL of the particle suspension. A small sample was dried on an indium tin oxide coated glass slide for further inspection using a scanning electron microscope (FEI, Quanta 250 FEG scanning electron microscope) combined with a fluorescence microscope (Seacom, Delmic, Netherlands). It was ensured, that fluorescent signals based on a 392 nm excitation strongly correlated with the particles' positions on the glass side (Figure 01a).

Alternatively, particles were prepared by staining FluoSpheres™ Polystyrene Microspheres (Thermo Scientific; catalogue number F13080). One milliliter of the bead suspension was mixed with 1 mL of acetone (Sigma Aldrich) for a duration of 2 min. Afterwards, 1 mg mL^{-1} PtTFPP dissolved in acetone was added and mixed for another 2 min. Subsequently, the acetone was slowly removed from the

solution by gently blowing nitrogen over the stirred solution. While the acetone evaporated, the dye became entrapped within the particles.

In all test cases, particles were centrifuged before each use. For this purpose, sensor particles at the target concentration were placed in centrifugation vessels containing the medium of the experiments. Sensor particles were then centrifuged at 3000 rpm for 5 minutes. For coral experiments, the sensor particles were repeatedly centrifuged in the seawater medium at a salinity of 33 PSU. Prior to experiments, the vessels were sonicated for 2 minutes to avoid larger aggregates. For microfluidic experiments, the supernatant was replaced with MQ water with 0.05 % surfactant (Tween 20, Sigma-Aldrich Co., Germany). Before sensor particles were injected into the system, they were sonicated for 15 minutes to decrease aggregate formation. Producing particles with the precipitation and staining method results in a large variety of particle sizes. To optimize the size distribution, the sensor particles were gently shaken and left for a time period of 24-48 h. In this way, sensor particle sizes separated by their density and can be pipetted from specific depths. For microfluidic test-case, we only sampled sensor particles which stayed dissolved for a time period of 48 h. Similarly, centrifugation was applied to sensor particles in the aggregate test-case. We note that, in addition to this study, the biocompatibility of similar sensor particles was previously tested in different applications for algae, other colony-forming corals and seagrass roots (Koren et al., 2015, 2016; Trampe et al., 2018).

Exciting and measuring sensPIV particles

In order to meet the illumination requirements for sensPIV imaging (≥10 Hz), high light intensities are required. In the past, such requirements were only fulfilled by high-energy continuous-wave or pulsed laser diodes, however, those limit the applicability as the costs are high, special requirements for safe operation are needed and experimental designs can become very complex. These

methodological limitations can be overcome with new ultra-bright light emitting diode (LED) systems that can reach light intensities similar to laser diodes. The commercially available LED systems applied in the coral and particle test case have powers ranging between 2.5 W (Wavelength dependent, Omicron, LedHUB, here used for rapid lifetime imaging) and 5 W (LPS3, ILA5150 GmbH, here used for ratiometric imaging). Collimation of LED light is challenging but using state-of-the-art optics, light sheets with widths of 500 µm - 1000 µm can be generated (Willert et al., 2010). To achieve this, the LED light was directed via a fiber bundle into the light sheet optics. In front of a cylindrical lens, the fiber bundle was aligned in a linear arrangement resulting in a light-sheet thickness of ~1000 µm (e.g. Figure 01 j). A second cylindrical lens was applied to yield a converging light sheet that minimizes the light sheet to a thickness of < 500 µm over a depth of ~ 2 mm. In many systems it is important to limit the total light exposure to avoid thermal convection or avoid substantial photosynthetic activity, therefore we triggered the light source via the camera and reduced the recording period to less than 5 s. However, to test if the high excitation light intensity affected the O_2 measurements within the coral test-case, we implanted a microsensor into the tissue where the photosynthetic symbionts are located, and observed an O_2 production of less than 10 µmol L^{-1} within the 2 s recording period with light exposure.

It should be noted that the optimal imaging frequency depends on the system of interest. In some microscale applications, such as the beating of cilia or flagella, recording frequencies of more than 100 Hz have to be achieved. In this case, the response-time of the sensor particles has to be considered. The O_2-dependent quenching of the sensor particles is diffusion limited and, thus, depends on the size of the particles. For the precipitated particles, the median size was 590 ± 360 nm resulting in the diffusion time-scale of $\tau = a^2 D^{-1} = 0.4\ \mathrm{ms} - 1\ \mathrm{ms}$. This implies that at recording frequencies of below 1000 Hz the sensor particles adapt quasi-instantaneously (compare Supplementary Video 1). However, as the sensor-

particle distribution is relatively wide, up to 5 µm, care has to be taken that the response-time of the sensor particles is not affecting the interpretation of results obtained through high-speed imaging (see also section on the limitations of sensPIV).

The lifetime of the O_2-sensitive dye (~60 µs) can be estimated via repeated imaging of the declining fluorescence intensity after light exposure (see for example (Koren et al., 2019)). This requires shutter-modulated cameras with a temporal resolution of order 10-100 s due to relatively slow sensor readout times and low light intensities employed in most experiments. Recent technical advances, namely a two-tap QMFLIM2 image sensor (pco.FLIM, PCO AG) allows to estimate the lifetime τ (~60 µs) in the frequency domain based on the frequency-shift, $\Delta\Phi$, induced by the quencher (O_2). Applying the camera allows us to keep light-intensities at a high level. Lifetime and frequency-shift are directly related through the equation $\tau=\tan(\Delta\Phi)/(2\pi f_{mod})$, where f_{mod} is the modulation frequency (~ 5 kHz). This method improves temporal resolution and lifetime images can be recorded in less than 10s (Koren et al., 2019). In order to improve the temporal resolution further, and to meet the requirements for particle velocimetry (recording frequencies above 10 Hz), we adapted the two-tap QMFLIM2 camera chip (pco.FLIM, PCO AG, Germany), which has in each pixel an in-pixel charge swing separating two taps. Each tap records half the period of the excitation signal, which is a sinus function. In reference experiments, the integration windows of the taps were temporally shifted to maximize the difference between the taps at 100 % O_2. The normalized difference of the taps will change with the O_2 concentrations and follows the rising flank of the sinus wave which is well represented by a second-order polynomial fit (see also Supplementary Figure 03). It has to be ensured that the expected quenching through O_2 results in a phase of much less than 90° at the given modulation frequency. Further, the in-pixel swing leads to an asymmetry of the two in-pixel taps that is intensity-dependent. This

asymmetry was corrected by recording a homogeneously illuminated object with a wavelength matching the emission wavelength of the O2-sensitive dye. A telecentric lens (TEC – V7X, Computar, USA) was fitted to the camera and a polyester filter (Lee filter, 101 Yellow, Canada) was used to filter the blue excitation light. Sensor particle excitation was achieved through a light sheet using a LedHUB attached to customized light sheet optics (see above).

SensPIV under well-defined O_2 gradients within microfluidic devices

A published microfluidic device design (Rusconi et al., 2014) was adapted to generate known linear O_2 gradients and validate the sensor particle response in heterogeneous conditions. The device consists of two parallel side channels that act as the O_2 source and sink, respectively, and a central channel where the O_2 gradient develops. See the device dimension and channel system cross-section in Figure 02.

The micro-channel system was designed with AutoCAD software (Autodesk, USA) and printed on a plastic photolithography mask (microlitho.co.uk). Then, a silicon wafer was spin coated with SU-8 photoresist (SU-8 2150, MicroChem company, US) and baked according to manufacturer recommendations to allow the formation of a cross-link between the photoresist and the silicon substrate. This step was repeated until the desired photoresist thickness (here 750 μm) was achieved. The photolithography mask was placed upon the photoresist-wafer complex in an alignment machine and exposed to UV light. After removing the mask from the photoresist, the whole wafer was submerged in an organic solvent (mr-DEV 600, micro resist technology) to dissolve the portions of the photoresist which were not cross-linked. A master was formed with the polymerized features on the silicon wafer.

The device was fabricated using standard PDMS replica molding procedures. Briefly, a 1:10 vacuum degassed PDMS solution consisting of curing agent: PDMS base (SYLGARD 184 Silicon Elastomer Base, Sigma-Aldrich Co., US) was poured onto the mold and thermally cured for at least 8 h at 80 °C. After curing, devices with a thickness of 5 mm were cut using a scalpel and peeled away. The PDMS device was plasma treated for 30 s (Zepto, Diener electronic GmbH, Germany) and bonded onto a 75 mm × 50 mm microscopy slide (2947-75×50, Corning Inc., US). Inlet and outlet ports were punched using a biopsy punch (Miltex Biopsy Punch, Integra LifeSciences Co., US). The resulting device was placed onto a heating plate set to 80 °C for 5 hours to improve bonding. Final channel widths and heights were 400 µm and 750 µm, respectively. The PDMS wall separating the fluidic test channel from the gas channels was 400 µm. The overall length of the serpentine pattern was 532 mm.

PtTFPP sensor particles, produced via the staining method, were calibrated under two O_2 levels within the microfluidic device. Before experiments, the two side channels were connected to two high-precision flow controllers (Cole Parmer, IL) via O_2 impermeable tubing (Masterflex 06404-14, Norprene, Saint-Gobain, France) and a small connecting piece (~10 cm) of Tygon tubing (Tygon, inner diameter 0.5 mm, outer diameter 1.5 mm, Saint-Gobain, France). The inlet of the central channel was connected to a 1 mL gas-tight syringe (Hamilton #1001, Reno, NV) mounted onto a syringe pump (neMESYS, CETONI GmbH, Germany) in order to control particle flow rates. First, N_2 was supplied into both side channels for 40 minutes to reach 0% air saturation within the gas permeable PDMS device. After this equilibration period, a solution of sensPIV particles was introduced into the central channel filled with MQ water and thereafter the flow was stopped to keep particles still. Particles in the main channel were then equilibrated to 0% air saturation for 20 minutes and imaged using an inverted Nikon Ti-E microscope (Nikon inc., Tokyo, Japan) and an sCMOS camera (Andor Zyla 4.2, Oxford

instruments, Belfast, UK); first by phase contrast using an LED white-light illuminator and then in fluorescence by excitation at 392 nm (Spectra X light engine, Lumencor Inc., Beaverton, OR, US). This was repeated for several locations along the central channel to obtain the calibration of particles for 0% O_2. To calibrate particles at 100% air saturation, compressed air was supplied to both side channels and the above calibration procedure was repeated again. In order to identify particles and relate the O_2 concentration to their fluorescence intensity, we applied a particle boundary tracing algorithm. First, brightfield images were pre-processed by tuning brightness, contrast and background subtraction. Then particles were identified through intensity thresholding and only particles with a circularity larger than 0.7 were included in the post-processing.

Experiments in microfluidic devices were performed with sensPIV particles under flow as well as no-flow conditions. In order to study the evolution of dissolved-O_2 over time, we simulated the dissolved-O_2 transport inside the microfluidic chips using a multiphysics COMSOL model based on the 3D microfluidic channel geometry. The flow field was simulated by solving the Stokes equations:

$$0 = -\nabla p + \mu \nabla^2 \boldsymbol{u} \qquad \text{(equation 02)}$$

where $\boldsymbol{u}$ is the velocity vector, p the pressure, μ dynamic viscosity and ∇ the gradient operator. The continuity equation for incompressible fluids reads:

$$\nabla \cdot \boldsymbol{u} = 0 \qquad \text{(equation 03)}$$

The O_2 distribution in the microfluidic chip was then calculated solving the advection-diffusion equation:

$$\frac{\partial C}{\partial t} = D \nabla^2 C - \boldsymbol{u} \cdot \nabla C \qquad \text{(equation 04)}$$

where *D* is the diffusion coefficient for O_2 in PDMS and water ($D_{O2,PDMS}$=3.25·10^{-9} m^2 s^{-1}, $D_{O2,water}$=2.01·10^{-9} m^2 s^{-1} based on a temperature of T = 293.15 K (Markov et al., 2014)) and C is the O_2 concentration. For all walls we assumed no-slip boundary conditions. The flow field was driven by the prescribed flow rate set by the syringe pump. To achieve a realistic O_2 distribution, the gas concentration of the outer channels was imposed at the boundary and saturated O_2 concentrations at the inlet were assumed.

Measuring the dynamic O_2 exchange around a model laboratory aggregate.

Model laboratory aggregates were prepared by mixing 2.48 mg mL^{-1} of sensor particles (produced via the precipitation method) with 0.7% agarose (Biozym, Germany). Agarose was dissolved in Milli-Q (MQ) water by boiling the mixture in a microwave. Subsequently, the solution was cooled down to ~40°C and sensPIV particles were added and thoroughly mixed. In order to form spherical particles the prepared agarose solution was pipetted into a glass beaker containing MQ water overlaid with cold canola oil (Ja! Canola Oil, Rewe). While cooling, the oil induced the formation of spherical model particles that subsequently sank from the oil layer into the MQ water. Particles were filtered using a 100 µm plankton mesh (Hydro-Bios, Germany), washed in MQ water and stored in the dark.

Experiments with model aggregates were performed in a recirculating glass flow chamber (height: 10.7 cm; diameter: 2.5 cm). To provide a homogeneous flow field, the glass chamber was connected via a 3D-printed polyether ether ketone (PEEK, FKM Sintertechnik Gmbh, Germany) inlet which had 1 mm capillaries, to a gear pump (ISMATEC, ISM901B, Germany). The pump volume was adjusted to achieve a flow velocity of 2.1 mm s^{-1} inside the flow chamber. The entire chamber was immersed in an aquarium filled with MQ water (dimensions: 18.4 x 9.7 x 9.7 cm) to stabilize the temperature at 20°C. Prior to all experiments, the particle was

degassed overnight using N_2 gas and only then attached to a needle connected to a motorized linear drive (Faulhaber, T-LSR75A, Germany). This allowed for the precise positioning of the agarose particle into the center of the recirculating glass flow chamber.

Calibration of the sensor particles was performed in the flow chamber via a degassing setup at ten different O_2 concentrations under the same conditions as in the experiments. The target O_2 concentrations were cross-checked with a microsensor (OXR430, Pyroscience, Germany). The O_2 concentration was reconstructed by decomposing the field of view into the interior of the aggregate and the outside of the aggregate. Care had to be taken to ensure that the darker image I_{T2} did not fall below the noise level, in which case the normalized intensity would not be uniquely associated with a specific O_2 concentration. In case I_{T2} fell below the noise level we performed calibration based on the difference of I_{T2} and I_{T1} which yielded good results. Flow fields were determined using a kinematic prediction algorithm (https://web.stanford.edu/~nto/LPT.shtml, Last Visit: 8/9/2021) in Matlab (2018b, Mathworks). In each image, 1154 ± 23 sensor particles were tracked and the reconstructed PTV tracks ranged between 5 - 463 individual data points.

SensPIV for the visualization of O_2 dynamics and vortical flows around the coral Porites lutea

We adapted a custom-built light sheet microscopy recirculating flow chamber setup (see (Pacherres et al., 2020) for details, schematic in Figure 04) with which we performed ratiometric O_2 measurements, PIV and PTV around a live coral specimen. A small fragment of the coral *Porites lutea,* roughly 2 cm in size, was placed into the flow chamber and a free-flow velocity of 1500 µm s^{-1} was imposed. After an equilibration period of 10 min, 1 mL of sensPIV particle stock solution (1 mg mL^{-1}) was added to the flow-chamber resulting in a final concentration of

0.025 mg mL^{-1}. In order to minimize mucus production, the coral was only exposed for short time periods (< 2 min) to sensor particles before filtering away the remaining particles via a syringe filter (0.22 µm, Millex) placed into the recirculation system. All experiments were performed in a temperature controlled room at 25° C. The sensor particles were illuminated with a blue LED (450 nm ± 30nm, LPS3, ILA GmbH, Germany) using light sheet optics (see also Figure 04a). Imaging was performed using an RGB camera (Grasshopper3, SONY ICX625, FLIR) through a custom-built microscopic lens array (based on Qioptiq Optem-Fusion System, Germany). Exposure times were reduced to below 20 ms and the light was triggered by the camera to minimize light exposure to the coral. The blue channel was used to determine the surface of the coral using an in-house developed tracking algorithm. PIV was performed based on the red channel (Em. > 550 nm) of the camera chip using standard cross-correlation techniques of two subsequent images using the software PIVView (Pivtec GmbH, Germany, see also Supplementary 1), and PTV was performed based on a kinematic prediction algorithm (https://web.stanford.edu/~nto/LPT.shtml, Last Visit: 8/9/2021) in Matlab (2018b, Mathworks). For both techniques, the images were pre-processed with a 5 px kernel gaussian high-pass filter to remove the background noise and signals of smaller particles. For PIV, we applied a multi-grid refinement technique with an initial window size of 256 px (approx. 460 µm for the coral test-case) and final window size of 64 px (approx. 115 µm). The window sizes were adjusted to achieve a sufficient particle density (7-9 particles) of larger sensor particles in each interrogation window. Depending on the flow features, it may be desirable to increase the particle density which can be achieved by increasing sensor-particle concentrations which will not affect calibration (compare Figure 1g). O_2 concentrations were determined based on ratiometric measurements of the red and green channel: I_R = R/G after calibration at various O_2 concentrations using Eq. (1). All image post-processing was performed in Matlab (2018b, Mathworks).

The boundary layer thickness was determined based on the average location where O_2 decreases to 10% of the surface concentration (compare also Supplementary Figure 05).

It should be noted that during the calibration procedure, we observed an emission of schott-glass filters that can affect the ratiometric measurements and corrections would require an additional light-dependent referencing of the applied filter. However, the problem can be overcome by using polyester filters (e.g. Lee filters, Canada). In addition to the sensPIV measurements, an electrochemical microsensor with a tip size of 20 µm (Unisense, Denmark) was used for comparison and to cross-reference the measurements. The microsensor was attached to a XYZ- micromanipulator (Unisense, Denmark) to perform profiles for comparison. O_2 measurements were performed in 20 µm steps.

Quantification and Statistical Analysis

Details of the statistical methods used in this study, such as the averaging procedure for improving signals of sensor particles, are described in detail in the respective sections and in the supplementary information that is available below. The number of replications for the measured parameters are described along with the presented means, or/and presented as distributions if sample size was sufficient. For linear regressions the fitting parameters along with statistical measures are present in the main text or in the supplementary information. Experimental results are cross-compared with numerical models or other methods such as O_2-microsensor measurements.

Video S1, related to Figure 04 and Figure 05: Response of sensor particles in flow to changing O_2 concentrations (see also STAR Methods section) where the scalebar indicates 5 mm. Similar sensor particles were applied in the aggregate test case (see Figure 04) and coral test case (see Figure 05)

Video S2, related to Figure 05: Raw recorded data of the coral test case (see Figure 05).

Declaration of interests

The authors declare no competing interests.

Supplementary Data

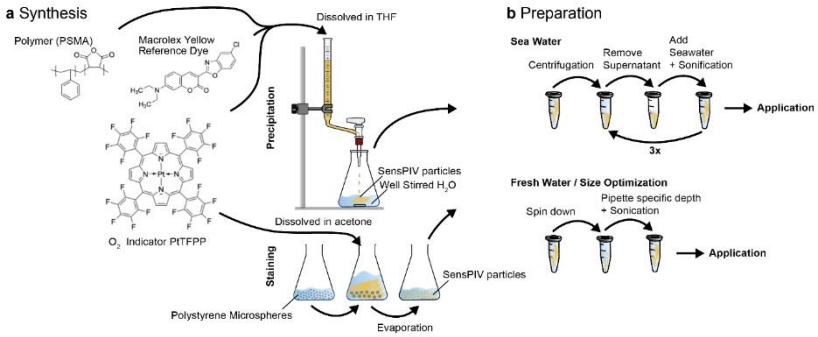

Supplementary Figure 01: Synthesis and preparation of sensPIV particles, related to Figures 1, 4 and 5. a sensPIV particles are produced using an O_2 indicator (PtTFPP) via, (i) a precipitation method (used for data shown in Figures 1, 4, 5) or (ii), the staining of polystrene microspheres (used for data shown in Figure 03). For the precipitation method, PtTFPP is dissolved in tetrahydrofuran (THF) and mixed with the reference dye macrolex yellow and the polymer styrene maleic anhydride (PSMA). Subsequently, the solution is carefully released into well-stirred water which results in the spontaneous forming of precipitates with the dyes embedded. For the staining method, commercially available polystyrene microspheres are mixed with PtTFPP and acetone, resulting in the swelling of the microspheres. After evaporation of acetone, the microsphere shrink and the PtTFPP dye becomes embedded. **b** Different preparation methods are used to transfer sensor particles to liquid medium (in this case sea water) (i) or optimize their size distribution (ii). To use sensPIV particles in saline liquids or sea-water (i), the sensor particles were first centrifuged, then the supernatant was removed. Subsequently, medium was added and the mixture was sonicated. This procedure was repeated at least 3 times. To optimize the particle size spectrum (ii), sensPIV-particles were either centrifuged or left to settle by gravity. In both cases, larger

sensPIV-particle aggregates sink towards the bottom which makes smaller particle sizes accessible by pipetting them from a specific depth.

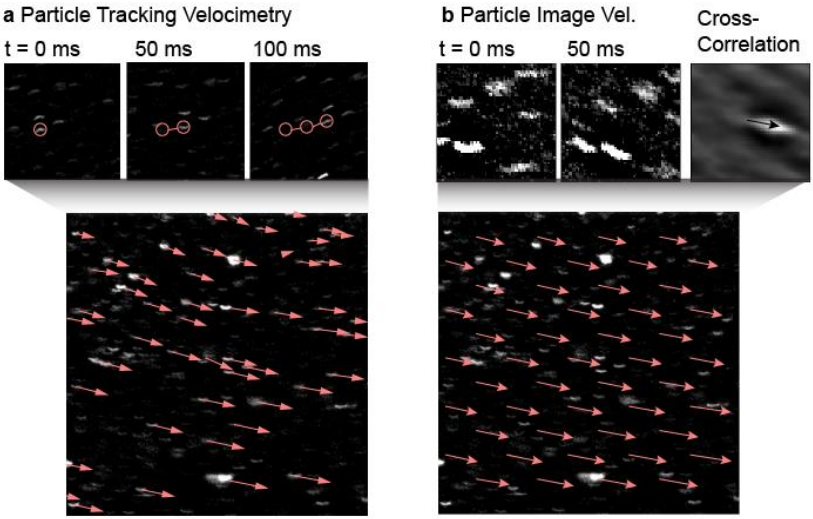

Supplementary Figure 02: The application of particle tracking velocimetry (PTV) and particle image velocimetry (PIV) to sensPIV particles, related to Figure 04 and Figure 05. a Example of PTV applied on sensPIV particles (e.g. see also Figure 04b). Here individual particles were tracked using intensity thresholding and by determining the trajectories of the particle (see methods for details). Red circles indicate a representative tracked particle while the time above the panels refer to the time when the camera was triggered and then caused the exposure of particles for 10-20 ms. b Example of PIV applied on sensPIV particles (see also test-case in Figure 05c). Here, an ensemble of 7-9 particles was used to calculate one velocity vector (see Figure 04c). The images were decomposed into small interrogation windows (b, upper panels) to ensure that 7-9 individual

particles were present in the same interrogation window (see methods). Each interrogation window was cross-correlated with the subsequent image, i.e. the image pairs were translated with respect to one another until the best match was found. This revealed the displacement of the particles within each window at every time step. The velocity for each interrogation window (right upper panel in b) was then calculated based on the peak of the cross-correlation and the known time step. For PIV and PTV, the red channel (Em. ≳ 550 nm) was extracted from RGB images and background noise and O_2 signals from small particles (≲ 2 µm) were removed via a Gaussian high-pass filter.

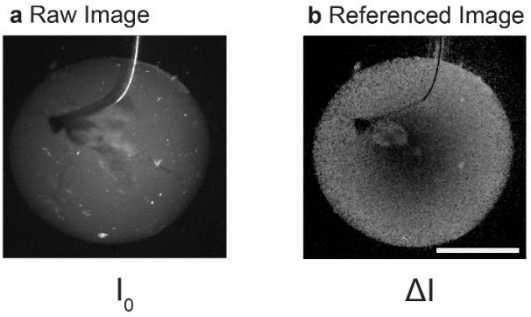

Supplementary Figure 03: Referencing of luminescence intensity via rapid lifetime imaging, related to Figure 04. a Raw image of an agarose aggregate where the core is anoxic and oxygen gradually increases towards the surface (processed data shown in Figure 04). The intensity image I_0 is O_2-dependent, but brighter spots originating from large sensor particles could be falsely interpreted as regions of low O_2 concentrations. **b** Referenced image of an agarose aggregate. Here the normalized intensity (ΔI) mostly compensates for size-dependent emission of sensor particles, despite a very short exposure time of 100 ms. The scalebar represents 2 mm.

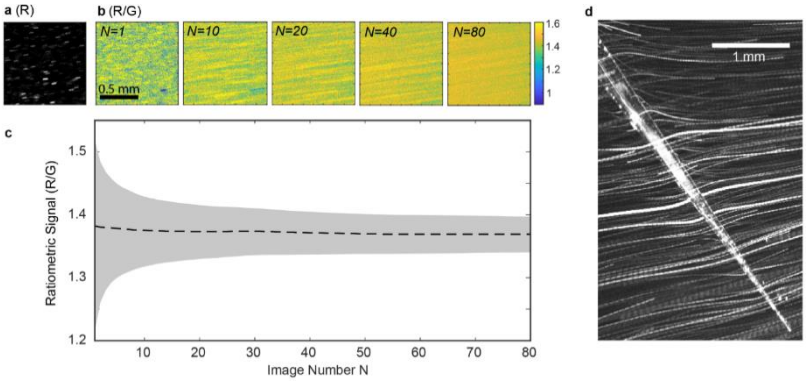

Supplementary Figure 04. Averaging image ensembles increases the accuracy of ratiometric signals, related to Figure 05. a A snapshot of a red channel image from which the flow field was reconstructed**. b** Average projection of increasing numbers of sensPIV images obtained from ratiometric imaging (R/G, pixel-wise division of the red and green channel). *N* represents the number of images which were averaged. O_2 concentrations were calculated from an average of at least 40 images for all experiments (for example test-cases in Figure 05). **c** Averaging of images leads to the convergence of ratiometric signals (R/G). The gray boundaries represent the 75% and 25% percentile of values within the test window (randomly chosen frame consisting of 400 x 400 px, approx. 720 µm) and the dashed line represents the mean. **d** Flow disturbances imposed by an electrochemical sensor in homogeneous bulk flow. Image is a maximum intensity projection of 100 sensPIV images.

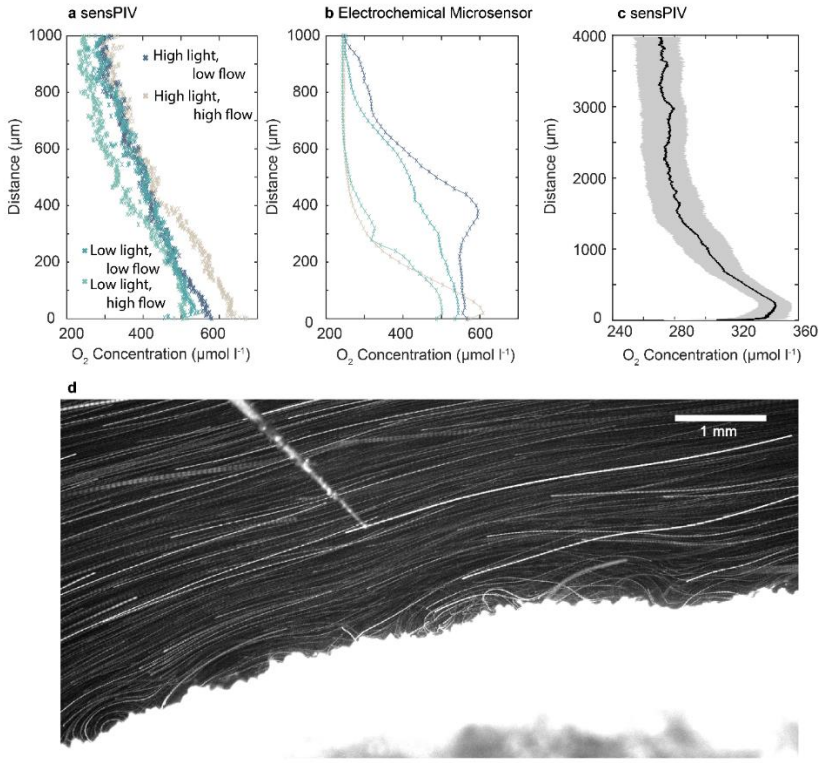

Supplementary Figure 05: Comparison of O_2 concentration profiles around the coral *Porites lutea* obtained from sensPIV particles vs. amperometric microsensors, related to Figure 05. a One-dimensional profiles extracted from sensPIV results (shown in Figure 05) along the row of pixels along the location of the microsensor. Data was recorded within a time window of 2 seconds. The coral was exposed to, i) low flow (300 µm s^{-1}) + low light (80 µmol quanta m^{-2} s^{-1}), ii) high flow (1500 µm s^{-1}) + low light (80 µmol quanta m^{-2} s^{-1}), iii) low flow (300 µm s^{-1}) + high light (160 µmol quanta m^{-2} s^{-1}), iv) high flow (1500 µm s^{-1}) + high light (160 µmol quanta m^{-2} s^{-1}). Each data point represents the O_2 value in one 1.8 µm pixel containing approximately 200 sensor particles. **b** O_2 concentrations

recorded close to the same location as used in **(a)** but using an electrochemical microsensor with a spatial resolution of 20 µm. Microsensor profiles were recorded within a time window of 5 min. Similar colors refer to the same experiment as in **(a)**. **c** Reconstructed O_2 concentrations along the entire surface of the coral for high light, low flow conditions. Here the gray boundaries represent the 75% and 25% percentile. **a-c** 0 on the y-axis represents the interface between coral tissue and sea water. **d** The flow field around the coral *P. lutea*. Maximum intensity projection for each pixel based on an ensemble of 100 individual images in the red channel (same data as shown in Figure 05).

Supplementary Table 1: Correlation coefficients comparing modelling results and measurements in the microfluidics experiment, related to Figure 03.

Overview of correlation coefficients (for data shown in Figure 03b,c) between measured and modelled concentration gradients ($R_{gradient}$) as well as between measured and modelled velocities ($R_{gradient}$). Measurements were performed at time 40 s, 1 min 10 s,1 min 40 s and 12 min 25 s under no flow conditions (left columns) and at time 50 s, 1 min 20 s,1 min 50 s and 12 min 35 s for flow conditions (right columns).

No flow conditions	Flow conditions
$R_{gradient,\ 12'\ 25''}=0.7569$ $R_{gradient,\ 1'\ 40''}=0.8347$ $R_{gradient,\ 1'\ 10''}=0.7963$ $R_{gradient,\ 40''}=0.5565$	$R_{gradient,\ 12'\ 35''}=0.7920$ $R_{gradient,\ 1'\ 50''}=0.8461$ $R_{gradient,\ 1'\ 10''}=0.8577$ $R_{gradient,\ 40''}=0.6423$ $R_{velocity}=0.8322$

Bibliography

Abe, S., Okamoto, K., & Madarame, H. (2004). The development of PIV–PSP hybrid system using pressure sensitive particles. *Measurement Science and Technology*, *15*(6), 1153–1157. https://doi.org/10.1088/0957-0233/15/6/016

Ahmerkamp, S., Winter, C., Janssen, F., Kuypers, M. M. M., & Holtappels, M. (2015). The impact of bedform migration on benthic oxygen fluxes. *Journal of Geophysical Research: Biogeosciences*, *120*(11), 2229–2242. https://doi.org/10.1002/2015JG003106

Ahmerkamp, S., Winter, C., Krämer, K., Beer, D. de, Janssen, F., Friedrich, J., Kuypers, M. M. M., & Holtappels, M. (2017). Regulation of benthic oxygen fluxes in permeable sediments of the coastal ocean. *Limnology and Oceanography*, *62*(5), 1935–1954. https://doi.org/10.1002/lno.10544

Batchelor, G. K. (1967). *An Introduction to Fluid Dynamics*. Cambridge University Press.

Behrendt, L., Salek, M. M., Trampe, E. L., Fernandez, V. I., Lee, K. S., Kühl, M., & Stocker, R. (2020). PhenoChip: A single-cell phenomic platform for high-throughput photophysiological analyses of microalgae. *Science Advances*, *6*(36). https://doi.org/10.1126/sciadv.abb2754

Bein, A., Shin, W., Jalili-Firoozinezhad, S., Park, M. H., Sontheimer-Phelps, A., Tovaglieri, A., Chalkiadaki, A., Kim, H. J., & Ingber, D. E. (2018). Microfluidic Organ-on-a-Chip Models of Human Intestine. *Cellular and Molecular Gastroenterology and Hepatology*, *5*(4), 659–668. https://doi.org/10.1016/j.jcmgh.2017.12.010

Bekker, A., Holland, H. D., Wang, P.-L., Rumble, D., Stein, H. J., Hannah, J. L., Coetzee, L. L., & Beukes, N. J. (2004). Dating the rise of atmospheric oxygen. *Nature*, *427*(6970), 117–120. https://doi.org/10.1038/nature02260

Bianchi, D., Weber, T. S., Kiko, R., & Deutsch, C. (2018). Global niche of marine anaerobic metabolisms expanded by particle microenvironments. *Nature Geoscience*, *11*(4), 263–268. https://doi.org/10.1038/s41561-018-0081-0

Borisov, S. M., Mayr, T., & Klimant, I. (2008). Poly(styrene- block - vinylpyrrolidone) Beads as a Versatile Material for Simple Fabrication of Optical Nanosensors. *Analytical Chemistry*, *80*(3), 573–582. https://doi.org/10.1021/ac071374e

Broomé, M., Maksuti, E., Bjällmark, A., Frenckner, B., & Janerot-Sjöberg, B. (2013). Closed-loop real-time simulation model of hemodynamics and oxygen transport in the cardiovascular system. *BioMedical Engineering OnLine*, *12*(1), 69. https://doi.org/10.1186/1475-925X-12-69

Byatt-Smith, J. G., Leese, H. J., & Gosden, R. G. (1991). An investigation by mathematical modelling of whether mouse and human preimplantation embryos in static culture can satisfy their demands for oxygen by diffusion. *Human Reproduction*, *6*(1), 52–57. https://doi.org/10.1093/oxfordjournals.humrep.a137258

Clark, L. C., Wolf, R., Granger, D., & Taylor, Z. (1953). Continuous Recording of Blood Oxygen Tensions by Polarography. *Journal of Applied Physiology*, *6*(3), 189–193. https://doi.org/10.1152/jappl.1953.6.3.189

Costello, J. H., Colin, S. P., Dabiri, J. O., Gemmell, B. J., Lucas, K. N., & Sutherland, K. R. (2021). The Hydrodynamics of Jellyfish Swimming. *Annual Review of*

Marine Science, *13*(1), 375–396. https://doi.org/10.1146/annurev-marine-031120-091442

de Beer, D., Kühl, M., Stambler, N., & Vaki, L. (2000). A microsensor study of light enhanced Ca2+ uptake and photosynthesis in the reef-building hermatypic coral Favia sp. *Marine Ecology Progress Series*, *194*, 75–85. https://doi.org/10.3354/meps194075

Drescher, K., Goldstein, R. E., Michel, N., Polin, M., & Tuval, I. (2010). Direct Measurement of the Flow Field around Swimming Microorganisms. *Physical Review Letters*, *105*(16), 168101. https://doi.org/10.1103/PhysRevLett.105.168101

Enuka, Y., Hanukoglu, I., Edelheit, O., Vaknine, H., & Hanukoglu, A. (2012). Epithelial sodium channels (ENaC) are uniformly distributed on motile cilia in the oviduct and the respiratory airways. *Histochemistry and Cell Biology*, *137*(3), 339–353. https://doi.org/10.1007/s00418-011-0904-1

Fabricius-Dyg, J., Mistlberger, G., Staal, M., Borisov, S. M., Klimant, I., & Kühl, M. (2012). Imaging of surface O2 dynamics in corals with magnetic micro optode particles. *Marine Biology*, *159*(7), 1621–1631. https://doi.org/10.1007/s00227-012-1920-y

Falkowski, P. G. (2006). Tracing Oxygen's Imprint on Earth's Metabolic Evolution. *Science*, *311*(5768), 1724–1725. https://doi.org/10.1126/science.1125937

Frederiksen, M. S., & Glud, R. N. (2006). Oxygen dynamics in the rhizosphere of Zostera marina: A two-dimensional planar optode study. *Limnology and Oceanography*, *51*(2), 1072–1083.

https://doi.org/10.4319/lo.2006.51.2.1072

Garren, M., Son, K., Raina, J.-B., Rusconi, R., Menolascina, F., Shapiro, O. H., Tout, J., Bourne, D. G., Seymour, J. R., & Stocker, R. (2014). A bacterial pathogen uses dimethylsulfoniopropionate as a cue to target heat-stressed corals. *The ISME Journal*, *8*(5), 999–1007. https://doi.org/10.1038/ismej.2013.210

Gemmell, B. J., Colin, S. P., Costello, J. H., & Dabiri, J. O. (2015). Suction-based propulsion as a basis for efficient animal swimming. *Nature Communications*, *6*(1), 8790. https://doi.org/10.1038/ncomms9790

Gemmell, B. J., Jiang, H., & Buskey, E. J. (2014). A new approach to micro-scale particle image velocimetry (μPIV) for quantifying flows around free-swimming zooplankton. *Journal of Plankton Research*, *36*(5), 1396–1401. https://doi.org/10.1093/plankt/fbu067

Gilpin, W., Bull, M. S., & Prakash, M. (2020). The multiscale physics of cilia and flagella. *Nature Reviews Physics*, *2*(2), 74–88. https://doi.org/10.1038/s42254-019-0129-0

Gilpin, W., Prakash, V. N., & Prakash, M. (2017). Vortex arrays and ciliary tangles underlie the feeding–swimming trade-off in starfish larvae. *Nature Physics*, *13*(4), 380–386. https://doi.org/10.1038/nphys3981

Gregory, J. W., Asai, K., Kameda, M., Liu, T., & Sullivan, J. P. (2008). A review of pressure-sensitive paint for high-speed and unsteady aerodynamics. *Proceedings of the Institution of Mechanical Engineers, Part G: Journal of Aerospace Engineering*, *222*(2), 249–290. https://doi.org/10.1243/09544100JAERO243

Guasto, J. S., Rusconi, R., & Stocker, R. (2012). Fluid Mechanics of Planktonic Microorganisms. *Annual Review of Fluid Mechanics*, *44*(1), 373–400. https://doi.org/10.1146/annurev-fluid-120710-101156

Kanso, E. A., Lopes, R. M., Strickler, J. R., Dabiri, J. O., & Costello, J. H. (2021). Teamwork in the viscous oceanic microscale. *Proceedings of the National Academy of Sciences*, *118*(29). https://doi.org/10.1073/pnas.2018193118

Karthäuser, C., Ahmerkamp, S., Marchant, H. K., Bristow, L. A., Hauss, H., Iversen, M. H., Kiko, R., Maerz, J., Lavik, G., & Kuypers, M. M. M. (2021). Small sinking particles control anammox rates in the Peruvian oxygen minimum zone. *Nature Communications*, *12*(1), 3235. https://doi.org/10.1038/s41467-021-23340-4

Katija, K., & Dabiri, J. O. (2008). In situ field measurements of aquatic animal-fluid interactions using a Self-Contained Underwater Velocimetry Apparatus (SCUVA). *Limnology and Oceanography: Methods*, *6*(4), 162–171. https://doi.org/10.4319/lom.2008.6.162

Kheradvar, A., Houle, H., Pedrizzetti, G., Tonti, G., Belcik, T., Ashraf, M., Lindner, J. R., Gharib, M., & Sahn, D. (2010). Echocardiographic Particle Image Velocimetry: A Novel Technique for Quantification of Left Ventricular Blood Vorticity Pattern. *Journal of the American Society of Echocardiography*, *23*(1), 86–94. https://doi.org/10.1016/j.echo.2009.09.007

Khosravi, Y., Kandukuri, R. D. P., Palmer, S. R., Gloag, E. S., Borisov, S. M., Starke, E. M., Ward, M. T., Kumar, P., de Beer, D., Chennu, A., & Stoodley, P. (2020). Use of an oxygen planar optode to assess the effect of high velocity microsprays on oxygen penetration in a human dental biofilms in-vitro.

BMC Oral Health, *20*(1), 230. https://doi.org/10.1186/s12903-020-01217-0

Kim, H. D., Yi, S. J., & Kim, K. C. (2013). Simultaneous measurement of dissolved oxygen concentration and velocity field in microfluidics using oxygen-sensitive particles. *Microfluidics and Nanofluidics*, *15*(2), 139–149. https://doi.org/10.1007/s10404-012-1130-4

Kiørboe, T., & Thygesen, U. (2001). Fluid motion and solute distribution around sinking aggregates. II. Implications for remote detection by colonizing zooplankters. *Marine Ecology Progress Series*, *211*, 15–25. https://doi.org/10.3354/meps211015

Klimant, I., Meyer, V., & Kühl, M. (1995). Fiber-optic oxygen microsensors, a new tool in aquatic biology. *Limnology and Oceanography*, *40*(6), 1159–1165. https://doi.org/10.4319/lo.1995.40.6.1159

Koch, C. J. (2002). *Measurement of absolute oxygen levels in cells and tissues using oxygen sensors and 2-nitroimidazole EF5* (pp. 3–31). https://doi.org/10.1016/S0076-6879(02)52003-6

Koren, K., Borisov, S. M., & Klimant, I. (2012). Stable optical oxygen sensing materials based on click-coupling of fluorinated platinum(II) and palladium(II) porphyrins—A convenient way to eliminate dye migration and leaching. *Sensors and Actuators B: Chemical*, *169*, 173–181. https://doi.org/10.1016/j.snb.2012.04.062

Koren, K., Brodersen, K. E., Jakobsen, S. L., & Kühl, M. (2015). Optical Sensor Nanoparticles in Artificial Sediments–A New Tool To Visualize O 2 Dynamics around the Rhizome and Roots of Seagrasses. *Environmental*

Science & Technology, *49*(4), 2286–2292. https://doi.org/10.1021/es505734b

Koren, K., Jakobsen, S. L., & Kühl, M. (2016). In-vivo imaging of O2 dynamics on coral surfaces spray-painted with sensor nanoparticles. *Sensors and Actuators B: Chemical*, *237*, 1095–1101. https://doi.org/10.1016/j.snb.2016.05.147

Koren, K., Moßhammer, M., Scholz, V. V., Borisov, S. M., Holst, G., & Kühl, M. (2019). Luminescence Lifetime Imaging of Chemical Sensors—A Comparison between Time-Domain and Frequency-Domain Based Camera Systems. *Analytical Chemistry*, *91*(5), 3233–3238. https://doi.org/10.1021/acs.analchem.8b05869

Krishnamurthy, D., Li, H., Benoit du Rey, F., Cambournac, P., Larson, A. G., Li, E., & Prakash, M. (2020). Scale-free vertical tracking microscopy. *Nature Methods*, *17*(10), 1040–1051. https://doi.org/10.1038/s41592-020-0924-7

Krzic, U., Gunther, S., Saunders, T. E., Streichan, S. J., & Hufnagel, L. (2012). Multiview light-sheet microscope for rapid in toto imaging. *Nature Methods*, *9*(7), 730–733. https://doi.org/10.1038/nmeth.2064

Kühl, M., Trampe, E., Mosshammer, M., Johnson, M., Larkum, A. W., Frigaard, N.-U., & Koren, K. (2020). Substantial near-infrared radiation-driven photosynthesis of chlorophyll f-containing cyanobacteria in a natural habitat. *ELife*, *9*. https://doi.org/10.7554/eLife.50871

Liao, Q., Bootsma, H. A., Xiao, J., Klump, J. V., Hume, A., Long, M. H., & Berg, P. (2009). Development of an in situ underwater particle image velocimetry

(UWPIV) system. *Limnology and Oceanography: Methods*, *7*(2), 169–184. https://doi.org/10.4319/lom.2009.7.169

Loiseau, E., Gsell, S., Nommick, A., Jomard, C., Gras, D., Chanez, P., D'Ortona, U., Kodjabachian, L., Favier, J., & Viallat, A. (2020). Active mucus–cilia hydrodynamic coupling drives self-organization of human bronchial epithelium. *Nature Physics*, *16*(11), 1158–1164. https://doi.org/10.1038/s41567-020-0980-z

Markov, D. A., Lillie, E. M., Garbett, S. P., & McCawley, L. J. (2014). Variation in diffusion of gases through PDMS due to plasma surface treatment and storage conditions. *Biomedical Microdevices*, *16*(1), 91–96. https://doi.org/10.1007/s10544-013-9808-2

Mayr, T., Borisov, S. M., Abel, T., Enko, B., Waich, K., Mistlberger, G., & Klimant, I. (2009). Light Harvesting as a Simple and Versatile Way to Enhance Brightness of Luminescent Sensors. *Analytical Chemistry*, *81*(15), 6541–6545. https://doi.org/10.1021/ac900662x

Menolascina, F., Rusconi, R., Fernandez, V. I., Smriga, S., Aminzare, Z., Sontag, E. D., & Stocker, R. (2017). Logarithmic sensing in Bacillus subtilis aerotaxis. *Npj Systems Biology and Applications*, *3*(1), 16036. https://doi.org/10.1038/npjsba.2016.36

Merl, T., & Koren, K. (2020). Visualizing NH3 emission and the local O2 and pH microenvironment of soil upon manure application using optical sensors. *Environment International*, *144*, 106080. https://doi.org/10.1016/j.envint.2020.106080

Meysman, F. J. R., Galaktionov, O. S., Glud, R. N., & Middelburg, J. J. (2010). Oxygen

penetration around burrows and roots in aquatic sediments. *Journal of Marine Research*, *68*(2), 309–336. https://doi.org/10.1357/002224010793721406

Mistlberger, G., Koren, K., Scheucher, E., Aigner, D., Borisov, S. M., Zankel, A., Pölt, P., & Klimant, I. (2010). Multifunctional Magnetic Optical Sensor Particles with Tunable Sizes for Monitoring Metabolic Parameters and as a Basis for Nanotherapeutics. *Advanced Functional Materials*, *20*(11), 1842–1851. https://doi.org/10.1002/adfm.201000321

Moradi, N., Liu, B., Iversen, M., Kuypers, M. M., Ploug, H., & Khalili, A. (2018). A new mathematical model to explore microbial processes and their constraints in phytoplankton colonies and sinking marine aggregates. *Science Advances*, *4*(10). https://doi.org/10.1126/sciadv.aat1991

Moritomo, H., Fujii, A., Suzuki, Y., Yoshihara, T., Tobita, S., & Kawamata, J. (2016). Biological oxygen sensing via two-photon absorption by an Ir(III) complex using a femtosecond fiber laser. *Japanese Journal of Applied Physics*, *55*(9), 092401. https://doi.org/10.7567/JJAP.55.092401

Morris, M. J., Donovan, J. F., Kegelman, J. T., Schwab, S. D., Levy, R. L., & Crites, R. C. (1993). Aerodynamic applications of pressure sensitive paint. *AIAA Journal*, *31*(3), 419–425. https://doi.org/10.2514/3.11346

Moßhammer, M., Brodersen, K. E., Kühl, M., & Koren, K. (2019). Nanoparticle- and microparticle-based luminescence imaging of chemical species and temperature in aquatic systems: a review. *Microchimica Acta*, *186*(2), 126. https://doi.org/10.1007/s00604-018-3202-y

Murniati, E., Gross, D., Herlina, H., Hancke, K., Glud, R. N., & Lorke, A. (2016).

Oxygen imaging at the sediment-water interface using lifetime-based laser induced fluorescence (τLIF) of nano-sized particles. *Limnology and Oceanography: Methods*, *14*(8), 506–517. https://doi.org/10.1002/lom3.10108

Nelson, H. R., & Altieri, A. H. (2019). Oxygen: the universal currency on coral reefs. *Coral Reefs*, *38*(2), 177–198. https://doi.org/10.1007/s00338-019-01765-0

Niedermair, F., Borisov, S. M., Zenkl, G., Hofmann, O. T., Weber, H., Saf, R., & Klimant, I. (2010). Tunable Phosphorescent NIR Oxygen Indicators Based on Mixed Benzo- and Naphthoporphyrin Complexes. *Inorganic Chemistry*, *49*(20), 9333–9342. https://doi.org/10.1021/ic100955z

Nielsen, L. T., & Kiørboe, T. (2021). Foraging trade-offs, flagellar arrangements, and flow architecture of planktonic protists. *Proceedings of the National Academy of Sciences*, *118*(3). https://doi.org/10.1073/pnas.2009930118

Okkelman, I. A., Neto, N., Papkovsky, D. B., Monaghan, M. G., & Dmitriev, R. I. (2020). A deeper understanding of intestinal organoid metabolism revealed by combining fluorescence lifetime imaging microscopy (FLIM) and extracellular flux analyses. *Redox Biology*, *30*, 101420. https://doi.org/10.1016/j.redox.2019.101420

P. J., S. (1998). Measuring tissue oxygen tension: A review. *Undersea and Hyperbaric Medicine*, *25*(3), 179–188. https://www.scopus.com/record/display.uri?eid=2-s2.0-0032163903&origin=inward

Pacherres, C. O., Ahmerkamp, S., Koren, K., Richter, C., & Holtappels, M. (2022).

Ciliary Flows in Corals Ventilate Target Areas of High Photosynthetic Oxygen Production. *SSRN Electronic Journal*. https://doi.org/10.2139/ssrn.4058690

Pacherres, C. O., Ahmerkamp, S., Schmidt-Grieb, G. M., Holtappels, M., & Richter, C. (2020). Ciliary vortex flows and oxygen dynamics in the coral boundary layer. *Scientific Reports*, *10*(1), 7541. https://doi.org/10.1038/s41598-020-64420-7

Pedersen, O., Borum, J., Duarte, C., & Fortes, M. (1998). Oxygen dynamics in the rhizosphere of Cymodocea rotundata. *Marine Ecology Progress Series*, *169*, 283–288. https://doi.org/10.3354/meps169283

Ploug, H. (2001). Small-scale oxygen fluxes and remineralization in sinking aggregates. *Limnology and Oceanography*, *46*(7), 1624–1631. https://doi.org/10.4319/lo.2001.46.7.1624

Quaranta, M., Borisov, S. M., & Klimant, I. (2012). Indicators for optical oxygen sensors. *Bioanalytical Reviews*, *4*(2–4), 115–157. https://doi.org/10.1007/s12566-012-0032-y

Raffel, M., Willert, C. E., & Kompenhans, J. (1998). Particle Image Velocimetry: A Practical Guide, 2. In *Springer*.

Revsbech, N. P., & Jørgensen, B. B. (1986). Microelectrodes: their use in microbial ecology. In *Advances in Microbial Ecology* (pp. 293–352). https://doi.org/10.1007/978-1-4757-0611-6_5

Rusconi, R., Guasto, J. S., & Stocker, R. (2014). Bacterial transport suppressed by fluid shear. *Nature Physics*, *10*(3), 212–217.

https://doi.org/10.1038/nphys2883

Seidel, S., Maschke, R. W., Werner, S., Jossen, V., & Eibl, D. (2021). Oxygen Mass Transfer in Biopharmaceutical Processes: Numerical and Experimental Approaches. *Chemie Ingenieur Technik*, *93*(1–2), 42–61. https://doi.org/10.1002/cite.202000179

Shapiro, O. H., Fernandez, V. I., Garren, M., Guasto, J. S., Debaillon-Vesque, F. P., Kramarsky-Winter, E., Vardi, A., & Stocker, R. (2014). Vortical ciliary flows actively enhance mass transport in reef corals. *Proceedings of the National Academy of Sciences*, *111*(37), 13391–13396. https://doi.org/10.1073/pnas.1323094111

Shen, N., Riedl, J. A., Carvajal Berrio, D. A., Davis, Z., Monaghan, M. G., Layland, S. L., Hinderer, S., & Schenke-Layland, K. (2018). A flow bioreactor system compatible with real-time two-photon fluorescence lifetime imaging microscopy. *Biomedical Materials*, *13*(2), 024101. https://doi.org/10.1088/1748-605X/aa9b3c

Sleigh, M. A. (1962). The Biology of Cilia and Flagella: International Series of Monographs on Pure and Applied Biology. In *Zoology, 12 (Elsevier)*.

Sommer, T., Danza, F., Berg, J., Sengupta, A., Constantinescu, G., Tokyay, T., Bürgmann, H., Dressler, Y., Sepúlveda Steiner, O., Schubert, C. J., Tonolla, M., & Wüest, A. (2017). Bacteria-induced mixing in natural waters. *Geophysical Research Letters*, *44*(18), 9424–9432. https://doi.org/10.1002/2017GL074868

Son, K., Brumley, D. R., & Stocker, R. (2015). Live from under the lens: exploring microbial motility with dynamic imaging and microfluidics. *Nature Reviews*

Microbiology, *13*(12), 761–775. https://doi.org/10.1038/nrmicro3567

Spencer, J. A., Ferraro, F., Roussakis, E., Klein, A., Wu, J., Runnels, J. M., Zaher, W., Mortensen, L. J., Alt, C., Turcotte, R., Yusuf, R., Côté, D., Vinogradov, S. A., Scadden, D. T., & Lin, C. P. (2014). Direct measurement of local oxygen concentration in the bone marrow of live animals. *Nature*, *508*(7495), 269–273. https://doi.org/10.1038/nature13034

Speth, D. R., in 't Zandt, M. H., Guerrero-Cruz, S., Dutilh, B. E., & Jetten, M. S. M. (2016). Genome-based microbial ecology of anammox granules in a full-scale wastewater treatment system. *Nature Communications*, *7*(1), 11172. https://doi.org/10.1038/ncomms11172

Stockdale, A., Davison, W., & Zhang, H. (2009). Micro-scale biogeochemical heterogeneity in sediments: A review of available technology and observed evidence. *Earth-Science Reviews*, *92*(1–2), 81–97. https://doi.org/10.1016/j.earscirev.2008.11.003

Stocker, R. (2012). Marine Microbes See a Sea of Gradients. *Science*, *338*(6107), 628–633. https://doi.org/10.1126/science.1208929

Tobita, S., & Yoshihara, T. (2016). Intracellular and in vivo oxygen sensing using phosphorescent iridium(III) complexes. *Current Opinion in Chemical Biology*, *33*, 39–45. https://doi.org/10.1016/j.cbpa.2016.05.017

Trampe, E., Koren, K., Akkineni, A. R., Senwitz, C., Krujatz, F., Lode, A., Gelinsky, M., & Kühl, M. (2018). Functionalized Bioink with Optical Sensor Nanoparticles for O 2 Imaging in 3D-Bioprinted Constructs. *Advanced Functional Materials*, *28*(45), 1804411. https://doi.org/10.1002/adfm.201804411

Wan, K. Y. (2018). Coordination of eukaryotic cilia and flagella. *Essays in Biochemistry*, *62*(6), 829–838. https://doi.org/10.1042/EBC20180029

Wang, X., & Wolfbeis, O. S. (2014). Optical methods for sensing and imaging oxygen: materials, spectroscopies and applications. *Chem. Soc. Rev.*, *43*(10), 3666–3761. https://doi.org/10.1039/C4CS00039K

Westerweel, J., Elsinga, G. E., & Adrian, R. J. (2013). Particle Image Velocimetry for Complex and Turbulent Flows. *Annual Review of Fluid Mechanics*, *45*(1), 409–436. https://doi.org/10.1146/annurev-fluid-120710-101204

Willert, C., Stasicki, B., Klinner, J., & Moessner, S. (2010). Pulsed operation of high-power light emitting diodes for imaging flow velocimetry. *Measurement Science and Technology*, *21*(7), 075402. https://doi.org/10.1088/0957-0233/21/7/075402

Yawata, Y., Cordero, O. X., Menolascina, F., Hehemann, J.-H., Polz, M. F., & Stocker, R. (2014). Competition–dispersal tradeoff ecologically differentiates recently speciated marine bacterioplankton populations. *Proceedings of the National Academy of Sciences*, *111*(15), 5622–5627. https://doi.org/10.1073/pnas.1318943111

Yousif, M. Y., Holdsworth, D. W., & Poepping, T. L. (2011). A blood-mimicking fluid for particle image velocimetry with silicone vascular models. *Experiments in Fluids*, *50*(3), 769–774. https://doi.org/10.1007/s00348-010-0958-1

Zetsche, E., Larsson, A. I., Iversen, M. H., & Ploug, H. (2020). Flow and diffusion around and within diatom aggregates: Effects of aggregate composition and shape. *Limnology and Oceanography*, *65*(8), 1818–1833.

https://doi.org/10.1002/lno.11420

Zhdanov, A. V., Golubeva, A. V., Okkelman, I. A., Cryan, J. F., & Papkovsky, D. B. (2015). Imaging of oxygen gradients in giant umbrella cells: an ex vivo PLIM study. *American Journal of Physiology-Cell Physiology*, *309*(7), C501–C509. https://doi.org/10.1152/ajpcell.00121.2015

Chapter 4

Single cell growth rates in well-defined oxygen gradients using a novel microfluidic device

Farooq Moin Jalaluddin*[1], Juliane Schoetz*[1], Soeren Ahmerkamp[1], Hannah K. Marchant[1], Wiebke Mohr[1], Marcel M.M. Kuypers[1]

* Authors contributed equally

potential co-authors who were involved in the presented work but have not yet read the manuscript:
Jana Milucka[1], Lars Behrendt[2], Simon van Vliet[4], Klaus Koren[3], Sten Littmann[1]

Authors Affiliations

[1] Max Planck Institute for Marine Microbiology, 28359 Bremen, Germany

[2] Science for Life Laboratory, Department of Organismal Biology, Uppsala University, Norbyvägen 18A, SE-752 36 Uppsala, Sweden

[3] Institute for Environmental Engineering, Department of Civil, Environmental and Geomatic Engineering, ETH Zurich, 8093 Zurich, Switzerland

[4] University of Basel, 4001 Basel, Switzerland

Manuscript in preparation

Abstract

The metabolism of microorganisms is intricately regulated by the chemical conditions in their surrounding microenvironment. Yet, most biogeochemical studies focus on bulk incubations in which the specific microenvironments and conditions to which microorganisms are exposed are poorly constrained. Here we developed and implemented a newly designed microfluidics platform in which single cells can be exposed to controlled chemical gradients. The microfluidic device allows cells to be trapped and grown within 16,000 growth traps of various sizes, accommodating at least eight different gas (e.g. oxygen) concentrations simultaneously with a solute gradient. We demonstrated that predictable and replicable chemical gradients can be achieved within the microfluidic device using oxygen (O_2) sensitive sensor particle experiments. Subsequently we developed a multiphysics model that accurately predicted O_2 and solute concentrations in each channel. In a proof-of-principle application, we inoculated *Photobacterium aquimaris* in the microfluidic device, a facultative anaerobe marine bacterium. Growing cells were subjected to an O_2 gradient amongst the growth traps and 17,092 individual cells were tracked over a 48-hour period using cell-segmentation. We show that average growth rates differed dependent on O_2 concentration (1.4 d^{-1} and 1.0 d^{-1}, under oxic and anoxic conditions, respectively), which was accompanied by distinct morphological differences (rod vs coccoid cells). The changes of the growth rate likely originate from switching the metabolism from oxic respiration to fermentation. Our newly developed microfluidic device allows observation of biological adaptations of growing cells under well-defined gas and solute concentrations. The microfluidic device will allow accurate estimation of metabolic thresholds, particularly in the context of respiratory switches, enabling new insights into the metabolic activities of single cells and their interactions with their microenvironment.

Introduction

Marine microorganisms play a vital role in the ocean by maintaining the health and stability of marine ecosystems, regulating global climate patterns, supporting the production of oxygen (O_2) and controlling nutrient availability and greenhouse gas emissions (Duce et al., 2008; Falkowski et al., 2008; Gruber & Galloway, 2008). Although microbial processes have planetary scale implications, it is the chemical conditions within the immediate surroundings of microorganisms that control microbial growth and turnover (Fenchel, 2002; Stocker, 2012). So far however, biogeochemical approaches have typically evaluated microbial activity at the relatively large scales, which average out, or neglect variations that occur over micrometers or millimeters. Chemical conditions at these scales are directly influenced by mass transfer induced by flow (at the millimeter to meter scale) and diffusion (at the micrometer scale), as well as microbial activity itself (Ceriotti et al., 2022; Depetris et al., 2021). Due to the spatial and temporal variability of these processes, the conditions experienced by individual microorganisms can substantially differ from bulk conditions (Rusconi et al., 2014). Bulk experiments therefore only provide limited insights into substrate preferences of specific microorganisms, the threshold concentrations at which enzymes can efficiently function (Berg et al., 2022), and the extent to which metabolic activity is influenced by mass transfer (Chapter 02).

In the oceans, O_2 is the primary electron acceptor for most marine microorganisms and plays a crucial role in driving organic carbon remineralization (Azam, 1998; Azam & Malfatti, 2007). Within the last century, the global ocean O_2 inventory has declined by 1-2%, with coastal systems becoming increasingly susceptible to low O_2 conditions (Limburg et al., 2020). Yet, our understanding of how and when O_2 reaches threshold levels for anaerobic microbial respiration is hindered by a lack of knowledge regarding the actual O_2 concentrations experienced by the

microorganisms (Canfield & Kraft, 2022; Stolper et al., 2010). In order to fill this knowledge gap, we need to understand the microenvironments around cells, which have so far been difficult to study - as most incubation methods do not allow for the precise control and measurement of the chemical microenvironments surrounding individual microorganisms. However, recent technological developments in microfluidics have enabled the microscale control of substrate concentrations, potentially allowing us to unravel how microbes respond to changes in their environment (Zhou et al., 2022). For example, innovative microfluidic devices can trap cells while ensuring a continuous influx of growth media (Dal Co et al., 2019; Kasahara et al., 2023). However, these devices so-far lack the ability to simultaneously expose and study single-cells to well-defined gas and solute concentration gradients.

To overcome the limitations of existing methods, we developed a microfluidic device that allows the study of single cells exposed to precise solute and gas concentrations, while simultaneously enabling cell observation. As a proof-of-principle, we examined the biological response of a marine microorganism (*Photobacterium aquimaris*) to an O_2 gradient. Our results show that this newly developed microfluidic system can provide insights into cell growth, replication times, and morphology changes in response to O_2 availability and can be used to gain a deeper understanding of the microscale biochemical interactions between microorganisms and their microenvironment.

Results

Novel microfluidic platform to study single-cell activity under well-defined gas and solute gradients

We developed a novel microfluidic platform “Christmas-bug” based on the combination of the well-established designs of phenoChip (Behrendt et al., 2020) and dual-input mother machine (Kaiser et al., 2018). The Christmas-bug design

consists of a mixing tree for two solute inputs, connected to eight pairs of main channels surrounded by two gas reservoirs (Figure 01a). Each channel consists of multiple dead-end growth traps containing cells (Figure 01b). The cells in the growth traps are exposed to a precisely controlled set of varying gas and solute concentrations (Figure 01c). Cells from the main channels in the Christmas-bug are trapped in the growth traps through three processes: Passive sampling by Brownian motion (i.e., the random movement of particles caused by collisions with atoms in the surrounding fluid), the motility of the organisms themselves, or by introducing air bubbles through which cells are pushed into the growth traps by applying low pressure.

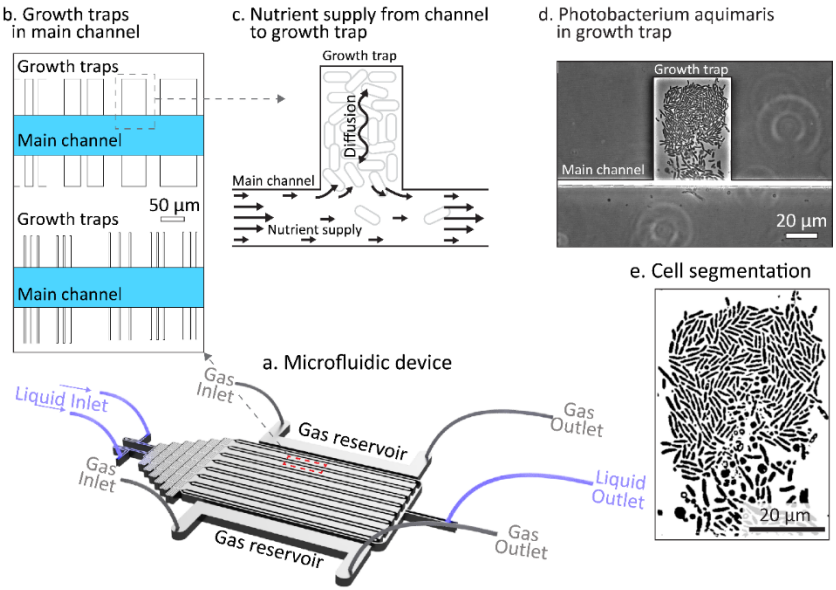

Figure 01: Schematic design of the novel microfluidic device (Christmas Bug) which allows individual cells to be trapped and exposed to well-defined solute and gas gradients. **a** Overview of the microfluidic device developed and used in this study, consisting two inputs for liquid solute, with two gas reservoirs alongside the main channel. **b** The main channels have dead-end growth traps with various widths and a height of 0.9 µm to trap cells. **c** Supply of medium from the main channel to the trapped cells in the growth trap is diffusion mediated to avoid exposing cells to shear. **d** Phase contrast image of *Photobacterium aquimaris* cells with various morphological shapes, which are located in a growth trap, **e** along with a result of image segmentation.

O_2 gas concentration gradient across the microfluidic device

Two gas reservoirs are aligned next to the outermost main channels in the Christmas-bug. These gas reservoirs are continuously flushed with either N_2 gas (anoxic channel) or air (oxic channel), establishing an O_2 gradient within the system (Figure 02b). It is essential that this gradient can be precisely predicted in order to know the conditions that microorganisms in each growth trap are exposed to. Therefore, we developed a two-dimension model that includes the microchannel geometry to predict O_2 (and other gas) gradients within the microfluidic device (Figure 02a), subsequently comparing it with O_2 concentration measurements (Figure 02c). The model simulates diffusion of O_2 between the two end channels (anoxic to oxic) and showed a that a gas concentration gradient should be established within hours in the microfluidic device. The equilibrium state for the gas gradient is reached after 5 hours in the model; slightly longer compared to the theoretical diffusion timescale of tau = d^2 / (2*D) = 4 hours , where d is the distance between the gas channels (7.3 mm) and D is the diffusion constant of O_2 in PDMS and water. It is important to note that the diffusion of gases in the PDMS and the solute in channels differ as a result of the different diffusion coefficients of O_2 in PDMS (D = $3.3 \cdot 10^{-09}$ m^2 s^{-1}) and in liquid phase (D = $2.0 \cdot 10^{-09}$ m^2 s^{-1}). To experimentally verify the model, we applied the sensPIV technology to measure the O_2 concentration in the main channels (Ahmerkamp et al., 2022). This technology allows for precise determination of oxygen concentrations within the chip, however, sensPIV measurements would be impractical to carry out every time the chip is used.

Both qualitatively and quantitatively, the mapped O_2 concentrations in the main channels as well as the the median O_2 concentration correspond well to the modeling results (Figure 02c). Therefore, we are confident that the model can be used to predict the concentration and gradient of O_2, as well as other gases while the chip is used to carry out experiments. Interestingly, in both the model and the

experimental data, O_2 concentrations did not change linearly along the microfluidic device, which contrasts with the expectations from simple one-dimensional sink/source models. Instead, they displayed a pronounced non-linearity, which is due to the different diffusion coefficients between the PDMS and liquid phases.

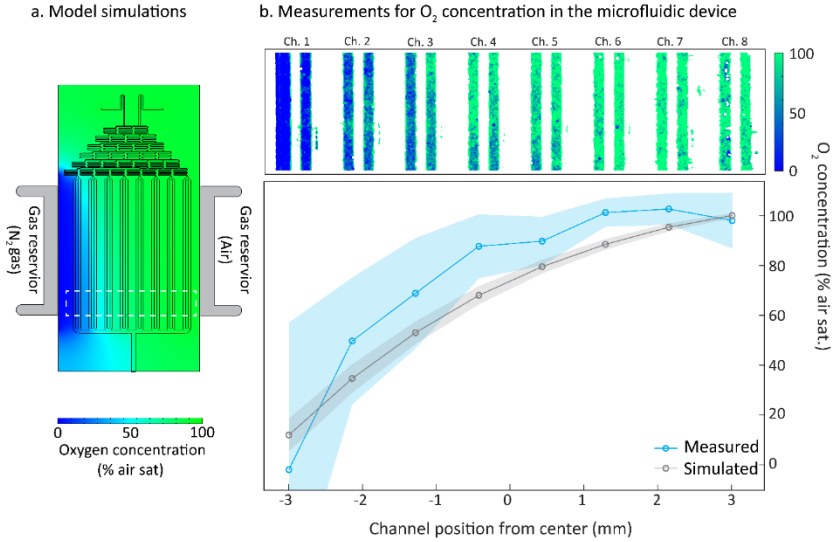

Figure 02: O_2 gradient within the microfluidic device. a Simulation of the O_2 distribution in the main channel and the surrounding PDMS of the microfluidic device. **b** O_2 concentrations in the main channels of the device determined using sensor particles, in agreement with the predicted concentrations from the model simulations. Note that as a result of variations of the diffusion coefficients of PDMS ($3.25 \cdot 10^{-09}$ m^2 s^{-1}) and water ($2.0 \cdot 10^{-09}$ m^2 s^{-1}), the O_2 gradient is non-linear.

Concentration gradients and flow visualization of liquid solute in the microfluidic device

To quantify that a linear solute gradient was established within the microfluidic device by mixing of the two liquid solutes, we extended the model for dual-solute input. Subsequently, we validated the model using experimental data obtained from mixing fluorescein with milliQ water in the microfluidic device. As expected the network of channels ("mixing-tree") and the associated folding of the two liquids at various concentrations in combination with the diffusive equilibration creates a linear gradient within the main channels (Figure 03a). Similar results were observed experimentally, with the fluorescent signal fluorescein gradually decreasing from channel 8 towards channel 1. In each channel, the concentration of the dye was homogenous, further validating the modeling results (Figure 03b,c).

The velocity magnitude profiles for each channel from the model simulations reveal constant velocities in all the main channels with highest velocity at the inlet and outlet resulting from the differences in channel widths (Figure 04a).

SensPIV particles used for O_2 concentration determination in the main channels were also used to visualize the flow field in the main channels to estimate the velocity. Particle tracking velocimetry using the sensPIV particles revealed an average velocity of 35 μm s^{-1} (± 5 μm s^{-1}) and was found to be largely consistent throughout the channels (Figure 04b,c) with a maximum deviation of 22%. The deviations in the velocity magnitude likely resulted from clogging of sensor-particles in the channel network and small variations in the applied pressure at the inlet. For future experiments, this can be improved by reducing the density of the sensPIV particles. By closer inspection of the velocity within individual channels we observed a parabolic velocity profile which is characteristic for a laminar channel flow.

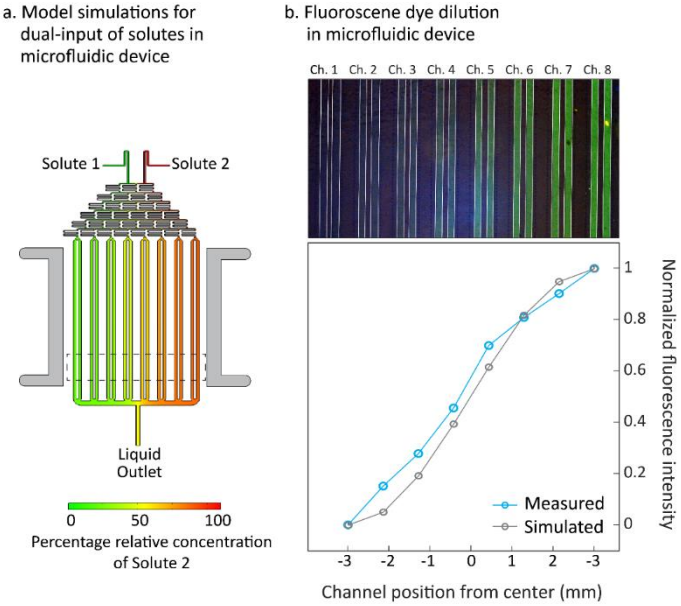

Figure 03: Liquid solute dilution in the microfluidic device. a Simulation of a solute gradient generated by mixing two liquid solutes in the main channel **b** Visualization of a solute gradient within the chip, visualized using two fluids; one with and one without a fluorescent dye, indicating that the produced gradient matches the modeling results.

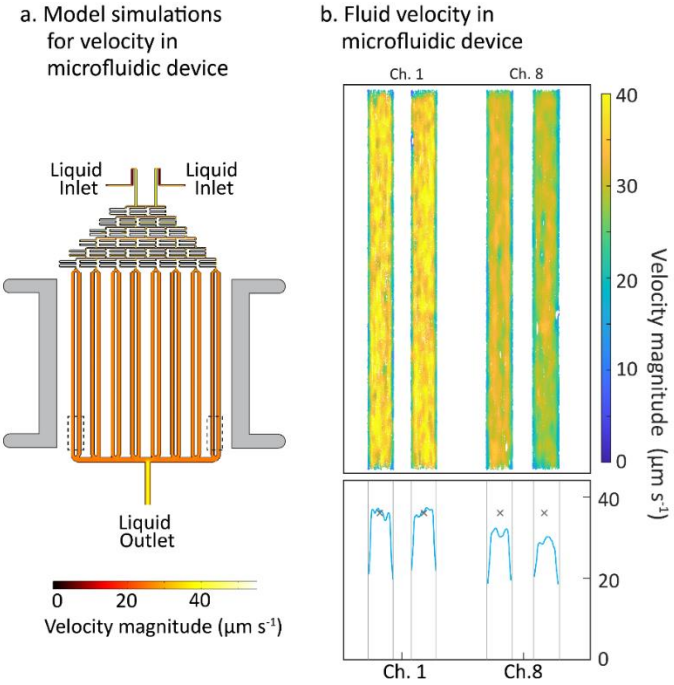

Figure 04: Flow visualization in the microfluidic device. a Simulated velocity in the main channels of the microfluidic device. **b** Measured flow velocities in the main channels, showing agreement with the modelling results. Measured velocities were relatively constant for the 8 main channels, as predicted by the model, with a maximum deviation of 22%, as depicted by the comparison of measurements from Ch.1 and Ch.8.

Growth rate of cell culture exposed to O_2 concentration gradient

To demonstrate how the microfluidic device can be used to incubate and study marine organisms, we used the facultative anaerobe marine bacterium *Photobacterium aquimaris* as a model organism to study the physiological responses of cells to different O_2 concentrations. Well-defined O_2 concentrations in the device were established by flushing the oxic gas reservoir with air (21% O_2) and the anoxic gas reservoir with N_2 gas. Prior to trapping, bacteria were grown in oxic liquid culture medium (marine broth) until exponential growth was reached. Subsequently, we pumped the liquid medium with cells at 10 µl h^{-1} into the microfluidic device and incubated the trapped cells in the well-developed O_2 concentration gradient for 48 hours. To avoid solute/substrate limitations within the microfluidic chip, we kept pumping fresh medium into the device after 24 hours. Following this, we examined the growth of cells within both the oxic and anoxic traps (Figure 05).

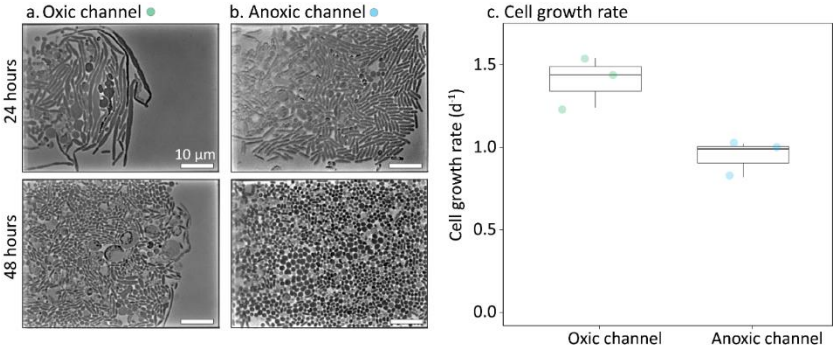

Figure 05: Growth of cell (*Photobacterium aquimaris*) in oxic and anoxic trap chambers. Visible differences in the growth rate and morphology of the cells in **a** oxic (21% air saturation) and **b** anoxic channel (N_2 gas) of the microfluidic device. **c** Growth rates were calculated based on the number of cells in the growth traps, oxic channels were observed to have higher growth rates in comparison to the anoxic channels (Refer to Figure S02 for image segmentation).

Microscopy was performed on the growth traps of the microfluidic device, and images were recorded for 10 randomly selected growth traps after 24 and 48 hours (Figure 05a,b). We utilized a trained image segmentation algorithm to accurately identify and segment individual cells within the images (see methods; Figure S02). This allowed us to determine the cell numbers, calculate the cell area, and assess the cell circularity for morphology. We observed an increase of cell numbers in the oxic growth traps (n= 3) of the microfluidic chip from 720 cells at 24 hours to 12386 cells at 48 hours (median growth rate 1.4 d^{-1}) and from 1591 cells at 24 hours to 4110 cells at 48 hours in the anoxic growth traps (n= 3) (median growth rate 1.0 d^{-1}). In addition to observing variability in growth rates, we also noticed significant changes in the morphology of the cells (Figure 06). Specifically, after 24 hours of growth in the growth traps, both the oxic and anoxic conditions displayed a mixed morphology of rod-shaped and coccoid cells (~15%

above 0.9 circularity). However, after 48 hours of incubation, the cells in the anoxic channels predominantly exhibited a coccoid morphology, 58% coccoid (>0.9 circularity) in anoxic channel compared to 21% in the oxic channel.

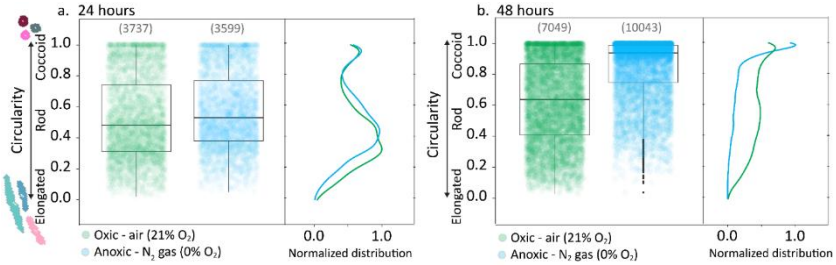

Figure 06: Comparative analysis of the cell morphology based on single cell circularity, under oxic and anoxic conditions. a After 24 hours of growth in the growth traps, the cells were imaged and found to exhibit a mixed morphology, with some cells appearing as rod-shaped and others as coccoid-shaped, under both oxic and anoxic conditions. **b** After 48 hours of incubation, the cells visualized in the anoxic channels were predominantly observed to be in coccoid shapes while incubated cells in oxic traps still had mixed morphologies. Each data point (circle) represents a single cell. Line plot in each side panel shows the normalized distribution of cell circularity. Y-axis includes illustrations showcasing the morphology of elongated and coccoid cells.

Discussion

We developed a versatile microfluidic device in which microorganisms can be studied under highly controllable and predictable gas and solute gradients. The "Christmas-bug" device facilitates direct observation of cells and enables investigations into cell growth, replication times, binary fission, and their reactions to gradients of both gases and solutes (Figure 01). Previously, similar microfluidic devices, which trap cells while ensuring a continuous influx of growth media, have often relied on a high mechanical pressure to trap cells (Chen et al., 2017; Lee et al., 2012). The high pressure could introduce biases in the results due to potential effects on cell metabolism and morphology (Delarue et al., 2017; Okumus et al., 2016). In contrast, the "Christmas-bug" approach achieves cell trapping through motility, Brownian motion or by introducing bubbles at low pressure. Furthermore, other devices are often constrained to either a single gas concentration or only a solute gradient, with replication often confined to a few growth traps. By combining both gas and solute gradients across 16,000 traps, our new device can accurately determine microbial activity and sensitivity thresholds, particularly in the context of aerobic and anaerobic microorganisms.

In a proof-of-principle application, we studied the marine bacterium *Photobacterium aquimaris* which is motile, has a fast doubling time, and can carry out both aerobic respiration and fermentation (Yoshizawa et al., 2009). After establishing an oxygen gradient within the microfluidic device, we were able to successfully trap *P. aquimaris* cells in the growth traps, and subsequently show that they were able to grow within them (Figure 05a,b). Here, we focus on how the growth characteristics of *P. aquimaris* differed between the fully oxic and fully anoxic traps. We found that the growth rate of the cells in the anoxic traps was around one-third lower than in the oxic chambers (Figure 05c), which is expected due to the lower Gibbs free energy yield of fermentation compared to aerobic

respiration. These results demonstrate the potential of the microfluidic device to track growth rates of microorganisms when they are provided with different substrates. The automated cell tracking algorithm that we used means that in future, growth rates can also be tracked at a higher temporal resolution and across the entire gas and solute gradient, which would subsequently provide important insights into the strategies that microorganisms use to obtain and manage energy. This will for example, facilitate accurate determination of the threshold concentration at which microorganisms switch between oxic and anoxic respiratory strategies.

We also examined the circularity as proxy for cell morphology in the oxic and anoxic growth traps. Pleomorphic cells (mixed morphology) were observed in the growth traps of both channels (oxic and anoxic) after 24 hours, with median circularity of ~0.5 (interquartile range 0.3 to 0.7) (rod- and coccoid-shaped cells). However after 48 hours, the majority of the cells in the anoxic growth-traps were coccoid (median circularity ~ 0.94 with interquartile range 0.7 to 0.9) (Figure 06) while cells in oxic growth-traps were still pleomorphic with median circularity ~ 0.6 (interquartile range 0.4 to 0.8). Based on the number of cells increased in the microfluidic chip, roughly 3 generations had elapsed in 24 hours before the physiological response to the anoxic conditions was observed. Morphological changes as a response to changing environmental conditions such as O_2 availability are common in bacteria, and have been attributed to adaptation of surface-to-volume ratio or length-to-width (aspect) ratio as a response to different substrate uptake mechanisms used during aerobic and anaerobic respiration (Harris & Theriot, 2016; Ojkic et al., 2019; van Teeseling et al., 2017). These adaptations are predicted to offer several benefits like increased uptake in low-nutrient conditions (Young, 2006) and allowing bacteria to maintain stable internal conditions amidst external fluctuations (Banerjee et al., 2017; Taheri-Araghi et al., 2015). Other studies have found that morphological adaptations can

be related to growth rate, wherein the size and shape of a bacterial cell is linked to membrane efficiency, ATP yield and therefore metabolic strategy (Schaechter et al., 1958; Szenk et al., 2017). Additionally, morphological adaptations to O_2 availability have been observed as a biological response of the cells towards stress and during spore formation (Pandey et al., 2013). Currently, it is difficult to determine which case might be more likely for the cells in the microfluidic chip. Intriguingly, however, in many previous modelling-based studies which link morphology to substrate availability, pleomorphic cells were rarely considered (Lopez-Garrido et al., 2018; Ojkic et al., 2016) as initial state of the cells (as we observed in the oxic condition).

In this study, we demonstrate how highly defined O_2 concentrations effect the growth rates and cell morphology of *Photobacterium aquimaris*. However, the applicability of the device extends to a diverse range of cells, making it valuable for conducting biogeochemical cycling relevant experiments involving different gas and solute concentrations. The microfluidic device could be used for determining the precise concentrations of nutrients and gas influencing the production and consumption rates of crucial electron acceptors like O_2 and nitrate (NO_3^-), as well as greenhouse gases such as nitrous oxide (N_2O) and methane (CH_4). By studying the cell activity, we can determine the apparent affinity values ($K_{m(app)}$ values - half-saturation constant for enzymatic uptake) for microbial respiration in response to different substrate concentrations. By conducting experiments using stable-isotope tracers (e.g. $^{15}NO_3$) in the microfluidic device we could potentially determine the relationship between O_2 concentration and the onset/inhibition of denitrification. Such values could then be integrated into modelling studies (Chapter 02) to better improve estimates of how and when denitrification occurs in environments with fluctuating O_2 concentrations.

In future applications, it will be beneficial to combine the incubations with further downstream analysis for more insights into the metabolic activity of single-cells. Recent advances in Raman spectroscopy would allow for direct measurements of stable isotope incorporation in the microfluidic chip (Weber et al., 2021). Advancements in electro-spray mass spectroscopy might be combined with the microfluidic device for high-sensitivity and high-throughput identification and quantification of metabolite exchange in cells (Giss et al., 2014; Smith et al., 2013; Smithers & Hayes, 2022). Further, the polydimethylsiloxane (PDMS) material used in microfluidics potentially allows the embedding of cells in LR White Resin (polyhydroxy-aromatic acrylic resin) and subsequent detachment of trapped cells, enabling subsequent physiological and biological analysis. Cells embedded in resin, could for example be analyzed in scanning electron microscopy (SEM) and energy-dispersive x-ray for elemental composition and combined with stable isotope derived cell uptake rates measured using nanoscale secondary ion mass spectrometry (Alcolombri et al., 2022). Combining the results together will enable us to understand differences in the microbial activity due to microscale variations experienced by the microbes in different microenvironments in the ocean.

Methods

Chip design

The chip is designed with eight pairs of main channels with multiple dead-end growth traps in all main channels (Figure 01a). The width of the main channels is 150 µm with a height of 15 µm and the dead-end growth traps have a length of 50 µm with a height of 0.9 µm. To ensure versatility and applicability to a broad range of microorganisms, the width of the growth traps varies from 1 to 120 µm along the main channel (Figure 01b). This variability enables the trapping of individual and multiple cells of different sizes. Within the microfluidic design, each pair of channels consists 2130 growth traps for trapping cells, of which over 70 growth

traps are specifically for multiple cell growth. Next to the main channels the chip has two gas reservoirs, to create a gas gradient in the chip. The device was designed using AutoCAD (v2022, Autodesk).

Silica wafer and microfluidic device fabrication

The two-layer fabrication of the wafer was outsourced to micro resist Technology. Briefly, the 4" silica-wafer was pre-treated with plasma. After adding an adherent layer, the SU-8 was spin coated in a 900 nm thick first layer onto the silica-wafer and pre-baked. To achieve the fine structures a fused silica negative-photomask was applied and the resist layer was exposed to UV-light resulting in the cross-linking of the resist. Post exposure bake was performed to complete crosslinking of resist structures and non-cross-linked material was removed using SU-8 developer. The procedure was repeated with a 15 µm layer and the main channels of the microfluidic design. Finally, a hard baking procedure was applied.

Microfluidic chips were produced in polydimethylsiloxane (PDMS) using the silica wafer mold. PDMS was prepared using Sylgard Elastomer Kit 18, by gently mixing a curing agent and pre-polymer at a ratio of 1:10. PDMS was gently poured on the photomask and was left in a vacuum-desiccator for 15 minutes or until bubble free. Silica waver along with PDMS was kept in the oven for 1 hour at 80°C for curing. PDMS embedded with design in the form of soft lithography was then cut and peeled off from the silica waver. Holes were punched for the in- and out-lets using 1.0 mm (I.D. 0.96 mm) biopsy punch (WellTech Rapid-core 15115-3) into the PDMS. PDMS was then carefully cleaned using a magic tape and pressured gas was blown to remove dust particles, followed by 1 minute treatment with plasma cleaner (Harrick Plasma Generator) for surface activation. PDMS was then attached to a glass slide and left in the oven at 80°C overnight for bonding.

Experimental setup for concentration measurement and incubations in the microfluidic device

The microfluidic device was placed in a temperature controlled incubation chamber and mounted on an inverted microscope (Leica DMI 6000B). The microscope was connected to two cameras: sCMOS camera (Excelitas PCO GmbH, pco.edge) for ratiometric imaging (see below) and CCD camera (Excelitas PCO GmbH, pco1600) for recording the images of the cells.

Dissolved O_2 concentration, liquid solute concentration and flow visualization in the microfluidic device

In order to test the performance of the microfluidic device we visualized oxygen gradients, flow field and liquid solute gradients within the microfluidic device. The oxygen gradient and flow was visualized by applying the novel SensPIV technology (Chapter 02; Ahmerkamp et al., 2022). Oxygen sensitive sensor particles were used for ratiometric imaging to measure the oxygen concentration and particle tracking for velocity measurements. Sensor particles used were prepared by precipitation, embedded with two types of dyes, platinum(II)-5,10,15,20-tetrakis-(2,3,4,5,6-penta- fluorophenyl)-porphyrin (PtTFPP; exci.: ~450 nm, em.: ~500-550 nm) and Macrolex fluorescent yellow 10GN (MY; exc.: ~450 nm, em.: ~480 nm) (Koren et al., 2015; Mistlberger et al., 2010). The stock solution was filtered using a 200 µm filter and sonicated before carefully filling in the syringes without bubbles. Loading of the microfluidic device with the sensPIV particles was performed by connecting the microfluidic device to a dual syringe pump (Harvard Apparatus, model: PHD Ultra) using PTFE tube natural (Adtech Polymer Engineering, diameter 0.30 mm) and 1 ml gas tight syringes (Hamilton Syringes).

The collected images with sensPIV particles were splitted into red (R) and green (G) channels to calculate the oxygen concentrations based on the ratiometric

signal (R/G) and a Stern-Volmer relationship (see Ahmerkamp et al., 2022). Calibration for the O_2 concentration was performed in the microfluidic chip based on the side channels, assuring constant supply of air (21% O_2, 78% N_2) and N_2 gas (0% O_2, 100% N_2). The sensor particles were tracked in the main channel to determine their flow direction and velocity. Additionally, to experimentally verify the dilution of two miscible solutes before reaching the main channels of the microfluidic device, a fluorescein dye and milli-Q water were pumped into inlet 1 and inlet 2, respectively. Green emission intensity signal from fluorescein was used to quantify the dilution. All image processing was carried out in Matlab (R2019a, Mathworks).

Model for diffusion time scales and mixing of liquids

To evaluate the predictability of the gas and solute gradient formation in the main channels of the microfluidic device, we employed a two-dimensional multiphysics model (Comsol Multiphysics 5.6). The two-dimensional design of the microfluidic device was imported as the model geometry. Inflow velocity of liquid was adjusted to the pumping velocity and the flow field was calculated by solving the Stokes equations:

$$0 = -\nabla p + \mu \nabla^2 \boldsymbol{u} \qquad \text{(equation 01)}$$

$$\nabla \cdot \boldsymbol{u} = 0 \qquad \text{(equation 02)}$$

where p is pressure gradient, μ is dynamic viscosity, ∇ is the gradient-operator, $\boldsymbol{u}$ is velocity vector field. Diffusion and advection equations were solved to study gradient formation:

$$\frac{\partial c}{\partial t} = \nabla \cdot (D \nabla c) - \nabla \cdot (\boldsymbol{u} c) \qquad \text{(equation 03)}$$

where ∇ represents gradient-operator, D is diffusion coefficient, ∇ is the del-operator, here, $\boldsymbol{u}$ is velocity vector and c is the gas/gradient concentration. The model domain represents to materials with different diffusion coefficients, namely PDMS ($D = 3.25 \cdot 10^{-09}$ m^2 s^{-1} at 25°C; Markov et al., 2014) which constituted the chip material and liquid medium ($D = 2.0 \cdot 10^{-09}$ m^2 s^{-1} at 25°C; Stewart, 2003) present in the channels and traps. By considering these material properties, we could accurately simulate the behavior of gas and solute mixing within the microfluidic device.

The model was simulated under two experimental conditions: (i) Solute concentration gradient: Two liquid media, mainly saturated water and anoxic water were pumped into the device, allowing formation of O_2 gradient. This condition was applied to test the predictability of solute mixing before reaching the main channels. (ii) Gas gradient formation: Air (21% O_2) and N_2 were introduced into the gas reservoirs, serving as oxic and anoxic end members for O_2 gradient formation, respectively. By analyzing the behavior of the gases within the microfluidic device, we aimed to confirm the predicted gas gradient formation.

Media preparation for bacterial culture and cell growth

For a first proof-of-principle application we trapped and cultivated *Photobacterium aquimaris* (DSMZ 2343) in the newly developed microfluidic device. Before trapping, the organism was cultured on marine broth agar plates (37.4 g L^{-1}). After colonies started to grow, they were carefully hand-picked and transferred using a sterile spatula to liquid medium (marine broth). The flask with the liquid culture was incubated overnight at room temperature until exponential growth (OD600 ~ 0.5-1.5) was attained. The culture was then pumped into the microfluidic device at a speed of 10 µl h^{-1}. After 24 hours, the majority of the growth traps were filled with cells and fresh marine broth medium was supplied

(Figure 01c). The growth rate of cells in the microfluidic chip were calculated using the equation (Fogg & Thake., 1987):

$$\text{Growth rate} = \frac{\ln(N_2) - \ln(N_1)}{t_2 - t_1} \qquad \text{(equation 04)}$$

where N_2 and N_1 are the number of cells at time t_2 and t_1, respectively.

Image segmentation

We used image segmentation for tracking the cells inside growth traps, to determine cell numbers and change in cell morphology. Two widely applied image segmentation platforms, namely Pancreatic phase contrast cell segmentation (Bioimage.io) and SuperSegger (Stylianidou et al., 2016), were tested on the recorded phase contrast images to distinguish cells from each other, to determine cell numbers and calculate cell morphological features such as cell area and shape. However, with these platforms we faced challenges in achieving accurate segmentation results due to the absence of fluorescence and cell morphology in the captured images and the difficulty in differentiating touching cells. To address these limitations, a machine learning-based bioimage analysis tool called ilastik (Berg et al., 2019) was employed. Briefly we trained a Random Forest algorithm (Breiman, 2001) based on pixel classification. We categorized the pixel based on the labels: (i) cells and (ii) background, where we put particular emphasis on touching cells. Visual inspection was carried out after training to assess unlabeled pixels and further data was iteratively added if needed. In total, 15 growth trap images were utilized along with 25 labels, each ranging from 15 to 100 pixels. This results in a training dataset of approximately 1500 data points. The trained model was then applied to segment a total of 50 images from different locations in the microfluidic chip. Post-processing of the segmented images was performed using ImageJ (Schindelin et al., 2012). The combination of ilastik machine learning and

ImageJ post-processing provided a robust and effective solution for accurate and reliable image segmentation, overcoming challenges associated with non-fluorescent cell images and segmentation of touching cells.

Acknowledgments

We thank D. Tienken, F. Schramm for technical assistance; G.Lavik, T. Ferdelman, B. Kartal, A. Chennu for valuable discussions; B. Vekeman, M. Kniaziuk for sharing information regarding culture work. H.K.M. and F.M.J. received funding from the DFG under Germany's Excellence Strategy (no. EXC-2077-390741603). S.H.A. and K.K. acknowledge funding by Novo Nordisk Fonden. The research was funded by the Max Planck Society.

Supplementary Figures

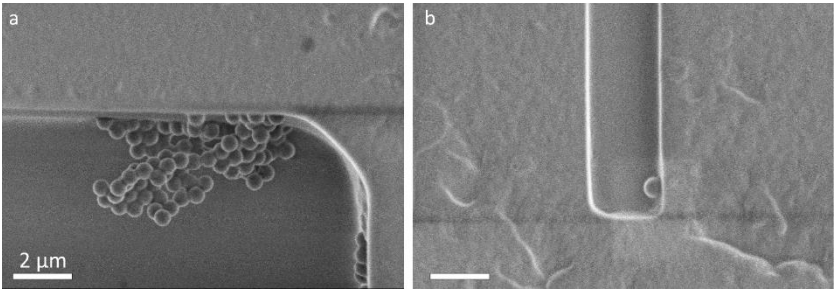

Figure S01: **Particles trapped in growth traps.** Scanning electron microscopic (SEM) images of the particles in the growth traps for multiple cells **(a)** and for single-cell traps **(b)**. Particles were used as representatives of the cells trapped and retained in growth traps, even after being detached from the device. Scale bar is 2 µm.

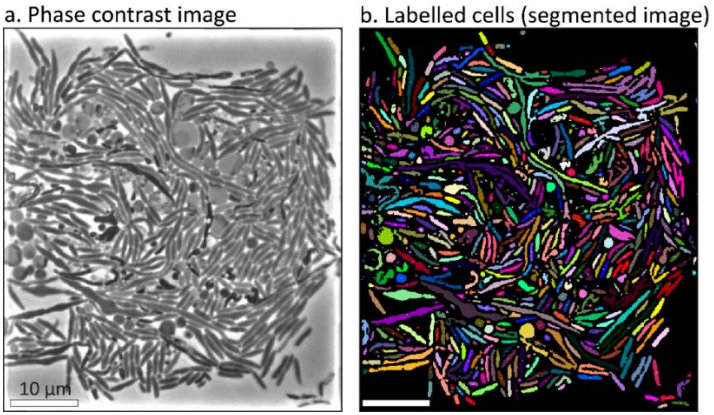

Figure S02: Comparison of the original image with cell segmentation using machine learning.

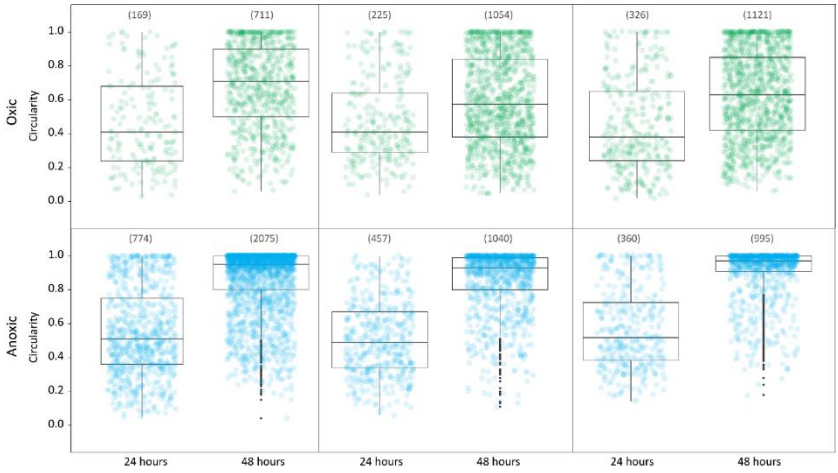

Figure S03: Cell morphology (circularity) under oxic and anoxic conditions in different growth traps, i.e. replicate measurements, for the 24 hours incubation and 48 hour incubation.

Bibliography

Ahmerkamp, S., Jalaluddin, F. M., Cui, Y., Brumley, D. R., Pacherres, C. O., Berg, J. S., Stocker, R., Kuypers, M. M. M., Koren, K., & Behrendt, L. (2022). Simultaneous visualization of flow fields and oxygen concentrations to unravel transport and metabolic processes in biological systems. *Cell Reports Methods*, *2*(5), 100216. https://doi.org/10.1016/j.crmeth.2022.100216

Alcolombri, U., Pioli, R., Stocker, R., & Berry, D. (2022). Single-cell stable isotope probing in microbial ecology. *ISME Communications*, *2*(1), 1–9. https://doi.org/10.1038/s43705-022-00142-3

Azam, F. (1998). Microbial Control of Oceanic Carbon Flux: The Plot Thickens. *Science*, *280*(5364), 694–696. https://doi.org/10.1126/science.280.5364.694

Azam, F., & Malfatti, F. (2007). Microbial structuring of marine ecosystems. *Nature Reviews Microbiology*, *5*(10), 782–791. https://doi.org/10.1038/nrmicro1747

Banerjee, S., Lo, K., Daddysman, M. K., Selewa, A., Kuntz, T., Dinner, A. R., & Scherer, N. F. (2017). Biphasic growth dynamics control cell division in Caulobacter crescentus. *Nature Microbiology*, *2*(9), 6–11. https://doi.org/10.1038/nmicrobiol.2017.116

Behrendt, L., Salek, M. M., Trampe, E. L., Fernandez, V. I., Lee, K. S., Kühl, M., & Stocker, R. (2020). PhenoChip: A single-cell phenomic platform for high-throughput photophysiological analyses of microalgae. *Science Advances*, *6*(36), 1–14. https://doi.org/10.1126/sciadv.abb2754

Berg, J. S., Ahmerkamp, S., Pjevac, P., Hausmann, B., Milucka, J., & Kuypers, M. M. M. (2022). How low can they go? Aerobic respiration by microorganisms under apparent anoxia. *FEMS Microbiology Reviews*, *46*(3), 1–14. https://doi.org/10.1093/femsre/fuac006

Berg, S., Kutra, D., Kroeger, T., Straehle, C. N., Kausler, B. X., Haubold, C., Schiegg, M., Ales, J., Beier, T., Rudy, M., Eren, K., Cervantes, J. I., Xu, B., Beuttenmueller, F., Wolny, A., Zhang, C., Koethe, U., Hamprecht, F. A., & Kreshuk, A. (2019). ilastik: interactive machine learning for (bio)image analysis. *Nature Methods*, *16*(12), 1226–1232. https://doi.org/10.1038/s41592-019-0582-9

Breiman, L. (2001). Random Forests. *Machine Learning*, *45*, 5–32. https://doi.org/10.1023/a:1010933404324

Canfield, D. E., & Kraft, B. (2022). The 'oxygen' in oxygen minimum zones. *Environmental Microbiology*, *24*(11), 5332–5344. https://doi.org/10.1111/1462-2920.16192

Ceriotti, G., Borisov, S. M., Berg, J. S., & De Anna, P. (2022). Morphology and Size of Bacterial Colonies Control Anoxic Microenvironment Formation in Porous Media. *Environmental Science and Technology*, *56*(23), 17471–17480. https://doi.org/10.1021/acs.est.2c05842

Chen, K. L., Crane, M. M., & Kaeberlein, M. (2017). Microfluidic technologies for yeast replicative lifespan studies. *Mechanisms of Ageing and Development*, *161*, 262–269. https://doi.org/10.1016/j.mad.2016.03.009

Dal Co, A., Ackermann, M., & Van Vliet, S. (2019). Metabolic activity affects the response of single cells to a nutrient switch in structured populations.

Journal of the Royal Society Interface, *16*(156). https://doi.org/10.1098/rsif.2019.0182

Delarue, M., Poterewicz, G., Hoxha, O., Choi, J., Yoo, W., Kayser, J., Holt, L., Hallatschek, O., & Weitz, D. A. (2017). SCWISh network is essential for survival under mechanical pressure. *Proceedings of the National Academy of Sciences of the United States of America*, *114*(51), 13465–13470. https://doi.org/10.1073/pnas.1711204114

Depetris, A., Peter, H., Bordoloi, A. D., Bernard, H., Niayifar, A., Kühl, M., de Anna, P., & Battin, T. J. (2021). Morphogenesis and oxygen dynamics in phototrophic biofilms growing across a gradient of hydraulic conditions. *IScience*, *24*(2). https://doi.org/10.1016/j.isci.2021.102067

Duce, R. A., LaRoche, J., Altieri, K., Arrigo, K. R., Baker, A. R., Capone, D. G., Cornell, S., Dentener, F., Galloway, J., Ganeshram, R. S., Geider, R. J., Jickells, T., Kuypers, M. M., Langlois, R., Liss, P. S., Liu, S. M., Middelburg, J. J., Moore, C. M., Nickovic, S., … Zamora, L. (2008). Impacts of atmospheric anthropogenic nitrogen on the open ocean. *Science*, *320*(5878), 893–897. https://doi.org/10.1126/science.1150369

Falkowski, P. G., Fenchel, T., & Delong, E. F. (2008). The microbial engines that drive earth's biogeochemical cycles. *Science*, *320*(5879), 1034–1039. https://doi.org/10.1126/science.1153213

Fenchel, T. (2002). Microbial Behavior in a Heterogeneous World. *Science*, *296*(5570), 1068–1071. https://doi.org/10.1126/science.1070118

Fogg, G. E., & Thake., B. (1987). *Algal cultures and phytoplankton ecology*. Univ of Wisconsin Press.

Giss, D., Kemmerling, S., Dandey, V., Stahlberg, H., & Braun, T. (2014). Exploring the interactome: Microfluidic isolation of proteins and interacting partners for quantitative analysis by electron microscopy. *Analytical Chemistry*, *86*(10), 4680–4687. https://doi.org/10.1021/ac4027803

Gruber, N., & Galloway, J. N. (2008). An Earth-system perspective of the global nitrogen cycle. *Nature*, *451*(7176), 293–296. https://doi.org/10.1038/nature06592

Harris, L. K., & Theriot, J. A. (2016). Relative rates of surface and volume synthesis set bacterial cell size. *Cell*, *165*(6), 1479–1492. https://doi.org/10.1016/j.cell.2016.05.045

Kaiser, M., Jug, F., Julou, T., Deshpande, S., Pfohl, T., Silander, O. K., Myers, G., & van Nimwegen, E. (2018). Monitoring single-cell gene regulation under dynamically controllable conditions with integrated microfluidics and software. *Nature Communications*, *9*(1), 212. https://doi.org/10.1038/s41467-017-02505-0

Kasahara, K., Leygeber, M., Seiffarth, J., Ruzaeva, K., Drepper, T., Nöh, K., & Kohlheyer, D. (2023). Enabling oxygen-controlled microfluidic cultures for spatiotemporal microbial single-cell analysis. *Frontiers in Microbiology*, *14*. https://doi.org/10.3389/fmicb.2023.1198170

Koren, K., Brodersen, K. E., Jakobsen, S. L., & Kühl, M. (2015). Optical sensor nanoparticles in artificial sediments-a new tool to visualize O2 dynamics around the rhizome and roots of seagrasses. *Environmental Science and Technology*, *49*(4), 2286–2292. https://doi.org/10.1021/es505734b

Lee, S. S., Vizcarra, I. A., Huberts, D. H. E. W., Lee, L. P., & Heinemann, M. (2012).

Whole lifespan microscopic observation of budding yeast aging through a microfluidic dissection platform. *Proceedings of the National Academy of Sciences of the United States of America*, *109*(13), 4916–4920. https://doi.org/10.1073/pnas.1113505109

Limburg, K. E., Breitburg, D., Swaney, D. P., & Jacinto, G. (2020). Ocean Deoxygenation: A Primer. *One Earth*, *2*(1), 24–29. https://doi.org/10.1016/j.oneear.2020.01.001

Lopez-Garrido, J., Ojkic, N., Khanna, K., Wagner, F. R., Villa, E., Endres, R. G., & Pogliano, K. (2018). Chromosome Translocation Inflates Bacillus Forespores and Impacts Cellular Morphology. *Cell*, *172*(4), 758-770.e14. https://doi.org/10.1016/j.cell.2018.01.027

Markov, D. A., Lillie, E. M., Garbett, S. P., & McCawley, L. J. (2014). Variation in diffusion of gases through PDMS due to plasma surface treatment and storage conditions. *Biomedical Microdevices*, *16*(1), 91–96. https://doi.org/10.1007/s10544-013-9808-2

Mistlberger, G., Koren, K., Scheucher, E., Aigner, D., Borisov, S. M., Zankel, A., Pölt, P., & Klimant, I. (2010). Multifunctional magnetic optical sensor particles with tunable sizes for monitoring metabolic parameters and as a basis for nanotherapeutics. *Advanced Functional Materials*, *20*(11), 1842–1851. https://doi.org/10.1002/adfm.201000321

Ojkic, N., López-Garrido, J., Pogliano, K., & Endres, R. G. (2016). Cell-wall remodeling drives engulfment during Bacillus subtilis sporulation. *ELife*, *5*(NOVEMBER2016), 1–30. https://doi.org/10.7554/eLife.18657

Ojkic, N., Serbanescu, D., & Banerjee, S. (2019). Surface-to-volume scaling and

aspect ratio preservation in rod-shaped bacteria. *ELife*, *8*, 1–11. https://doi.org/10.7554/eLife.47033

Okumus, B., Landgraf, D., Lai, G. C., Bakhsi, S., Arias-Castro, J. C., Yildiz, S., Huh, D., Fernandez-Lopez, R., Peterson, C. N., Toprak, E., El Karoui, M., & Paulsson, J. (2016). Mechanical slowing-down of cytoplasmic diffusion allows in vivo counting of proteins in individual cells. *Nature Communications*, *7*(May). https://doi.org/10.1038/ncomms11641

Pandey, R., Ter Beek, A., Vischer, N. O. E., Smelt, J. P. P. M., Brul, S., & Manders, E. M. M. (2013). Live Cell Imaging of Germination and Outgrowth of Individual Bacillus subtilis Spores; the Effect of Heat Stress Quantitatively Analyzed with SporeTracker. *PLoS ONE*, *8*(3). https://doi.org/10.1371/journal.pone.0058972

Rusconi, R., Garren, M., & Stocker, R. (2014). Microfluidics Expanding the Frontiers of Microbial Ecology. *Annual Review of Biophysics*, *43*(1), 65–91. https://doi.org/10.1146/annurev-biophys-051013-022916

Schaechter, M., Maaloe, O., & Kjeldgaard, N. (1958). Dependency on medium and temperature of cell size and chemical composition …. *Microbiology*. http://mic.sgmjournals.org/cgi/content/abstract/19/3/592

Schindelin, J., Arganda-Carreras, I., Frise, E., Kaynig, V., Longair, M., Pietzsch, T., Preibisch, S., Rueden, C., Saalfeld, S., Schmid, B., Tinevez, J.-Y., White, D. J., Hartenstein, V., Eliceiri, K., Tomancak, P., & Cardona, A. (2012). Fiji: an open-source platform for biological-image analysis. *Nature Methods*, *9*(7), 676–682. https://doi.org/10.1038/nmeth.2019

Smith, C. A., Li, X., Mize, T. H., Sharpe, T. D., Graziani, E. I., Abell, C., & Huck, W. T. S.

(2013). Sensitive, high throughput detection of proteins in individual, surfactant-stabilized picoliter droplets using nanoelectrospray ionization mass spectrometry. *Analytical Chemistry*, *85*(8), 3812–3816. https://doi.org/10.1021/ac400453t

Smithers, J. P., & Hayes, M. A. (2022). Interfacing microfluidics with information-rich detection systems for cells, bioparticles, and molecules. *Analytical and Bioanalytical Chemistry*, *414*(16), 4575–4589. https://doi.org/10.1007/s00216-022-04043-1

Stewart, P. S. (2003). Diffusion in Biofilms. *Journal of Bacteriology*, *185*(5), 1485–1491. https://doi.org/10.1128/JB.185.5.1485

Stocker, R. (2012). Marine Microbes See a Sea of Gradients. *Science*, *338*(6107), 628–633. https://doi.org/10.1126/science.1208929

Stolper, D. A., Peter, N. R., & Canfield, D. E. (2010). *Aerobic growth at nanomolar oxygen concentrations*. *107*, 44. https://doi.org/10.1073/pnas.1013435107

Stylianidou, S., Brennan, C., Nissen, S. B., Kuwada, N. J., & Wiggins, P. A. (2016). SuperSegger: robust image segmentation, analysis and lineage tracking of bacterial cells. *Molecular Microbiology*, *102*(4), 690–700. https://doi.org/10.1111/mmi.13486

Szenk, M., Dill, K. A., & de Graff, A. M. R. (2017). Why Do Fast-Growing Bacteria Enter Overflow Metabolism? Testing the Membrane Real Estate Hypothesis. *Cell Systems*, *5*(2), 95–104. https://doi.org/10.1016/j.cels.2017.06.005

Taheri-Araghi, S., Bradde, S., Sauls, J. T., Hill, N. S., Levin, P. A., Paulsson, J., Vergassola, M., & Jun, S. (2015). Cell-size control and homeostasis in bacteria. *Current Biology*, *25*(3), 385–391. https://doi.org/10.1016/j.cub.2014.12.009

van Teeseling, M. C. F., de Pedro, M. A., & Cava, F. (2017). Determinants of bacterial morphology: From fundamentals to possibilities for antimicrobial targeting. *Frontiers in Microbiology*, *8*(JUL), 1–18. https://doi.org/10.3389/fmicb.2017.01264

Weber, F., Zaliznyak, T., Edgcomb, V. P., & Taylor, G. T. (2021). Using Stable Isotope Probing and Raman Microspectroscopy To Measure Growth Rates of Heterotrophic Bacteria. *Applied and Environmental Microbiology*, *87*(22). https://doi.org/10.1128/AEM.01460-21

Yoshizawa, S., Wada, M., Kita-tsukamoto, K., Yokota, A., & Kogure, K. (2009). *Photobacterium aquimaris sp . nov ., a luminous marine bacterium isolated from seawater*. 1438–1442. https://doi.org/10.1099/ijs.0.004309-0

Young, K. D. (2006). The Selective Value of Bacterial Shape. *Microbiology and Molecular Biology Reviews*, *70*(3), 660–703. https://doi.org/10.1128/mmbr.00001-06

Zhou, P., He, H., Ma, H., Wang, S., & Hu, S. (2022). A Review of Optical Imaging Technologies for Microfluidics. *Micromachines*, *13*(2). https://doi.org/10.3390/mi13020274

Chapter 5

Synthesis and future research

5.1 Synthesis

Microbial transformations govern biogeochemical cycling within the oceans. Although the dynamics of marine microbial communities are certainly shaped by larger-scale processes, the life and metabolism of an individual microorganism is defined by processes occurring on a much smaller scale (micrometer to millimeter scale). At this scale, marine microorganisms reside within so-called microenvironments, where chemical conditions are controlled by the interplay between transport processes and microbial activity itself. However there is still limited knowledge about the occurrence of marine microenvironments and microbial metabolism within them.

The aim of this thesis was to investigate the mechanisms of the formation of microenvironments due to the interplay of transport processes and microbial metabolism, and its consequences on the biogeochemical cycling. In the thesis I developed microfluidic techniques and combined them with model simulations to investigate the microscale processes controlling the formation of microenvironments.

In **chapter 2**, to my knowledge, for the first time we were able to visualize the production and consumption of oxygen on individual sand grains. The observed high variability in respiration rates was linked to the patchy microbial colonization on the sand surface, suggesting the presence of distinct microenvironments which can potentially turn anoxic. However, our incubations were conducted in a static microfluidic device, limiting the study to diffusive solute supply without considering advection. To overcome this limitation, we incorporated transport processes in sandy sediments and used modeling approach to estimate the volumes of anoxic microenvironments. This revealed that the microenvironments play an extremely important role in sands, and in fact, when we integrated results into North Sea models, it appears we previously

underestimated denitrification rates by 40%. Within **chapter 2** we realized that there is a knowledge gap in our understanding on the interplay of flow and diffusive exchange processes on the microscale. In **chapter 3**, we improved on this by developing a new method: SensPIV to visualize the microscale transport, i.e. diffusive and advective fluxes, of oxygen revealing new insights into the chemical-conditions within microenvironments. Our non-invasive method was successfully applied to a model laboratory particle resembling marine aggregates and reef-building corals. Applying the SensPIV technique, we could reproduce O_2 concentration fields surrounding porous and impermeable aggregates that were previously measured with microsensors (Ploug et al., 1997; Ploug et al., 1999). Based on the examination of aggregate interior and exterior oxygen concentrations over time under no flow and flow conditions in the absence of reactions, we estimated a tenfold increase in O_2 exchange over previous estimates at similar Pèclet numbers (Kiørboe et al., 2001; Kiørboe & Thygesen, 2001). Previous estimates assumed stationarity which implies that fluxes into the aggregate and the reactions within the aggregate are in equilibrium. When simulating aggregates as solid particles, these stationary conditions are imposed by applying Dirichlet (constant concentration) or Neumann (constant flux) boundary conditions (Kiørboe et al., 2001). The disparity between our results and the modeling results for solid particles probably originate from the fact that these boundary conditions and the Pèclet number alone are not sufficient to represent the complexity of O_2 exchange between the aggregates interior and exterior, particularly, when time variant conditions are present. Further, the parametrization of the Dirichlet and Neumann boundary conditions requires an a priori knowledge on the reactions inside the aggregate. Flow induced uptake enhancement is only occurring if the interior of the particle is O_2 limited, which is difficult to estimate from boundary conditions alone. To resolve this, the recently newly developed mathematical modelling approach that simulates aggregates as

porous, impermeable particles (Moradi et al., 2021), in combination with measurements through the SensPIV technology, has the potential to provide new insights in O_2 exchange between aggregates and the surrounding water column

After the quantification of the formation of distinct microenvironments due to complex interplay between transport processes and microbial respiration rates, I aimed to study the microbial activity and biological adaptations of the microbial community inhabiting these distinct microenvironments. Specifically, my focus was on studying how microorganisms respond to changing oxygen concentrations within microenvironments. In **chapter 4**, I developed a microfluidic device that allowed us to trap and cultivate individual cells and observe their growth rates and morphotypes under well-defined oxygen concentrations. The results showed varying growth rates of cells under oxic and anoxic environments, along with delayed morphological adaptations within the community as a response to different oxygen concentrations. We also observed some morphological variability within the microbial community in oxic and anoxic environments.

However, many aspects controlling biogeochemical cycling in marine environments, specifically related to microscale mass transport and microbial activity within anoxic microenvironments, remain unknown. During my research, I encountered key challenges that led to open questions, which I aim to address in the following section. I will also propose possible experiments to explore and shed light on these unresolved aspects.

5.2 Open questions and future research

What are the other sandy sediment properties that support high microbial respiration?

Since the original microscopy studies of sand grains (Anderson & Meadows, 1978; Weise & Rheinheimer, 1977), the patchy microbial colonization on the surface has been correlated with cracks and depressions, putatively as a protection against abrasion (Ahmerkamp et al., 2020; Yawata et al., 2016). While I observed similar patterns of colonization on individual sand grains, it also became apparent to me that not all sand grains were the same and so far, it remains unknown how other factors contribute to the patchy colonization and transport of solute to the microbial community residing on the sand grains. For instance, what impact does the mineral composition, shape, and transparency of the sand grains have in microbial colonization and activity?

The mineral composition of a sand grain typically consists of various minerals, such as quartz, feldspar, mica, and other minerals depending on the specific source and geological origin of the sand (Doyle, 1965; Folk, 1954). Different mineral compositions of the sand grains provide varying surface properties and chemical characteristics (Barclay & Buckingham, 2009; Ghadr & Assadi-Langroudi, 2019), and I hypothesize that these influence the attachment, growth, and activity of the microorganisms. Some of these observations of the differences in mineral composition and shape of sand grains are shown in Figure 01. Furthermore, I observed that phototrophs were more associated with the transparent sand grains. Studies reported similar observations for continental shelf sediments, attributing the behavior to the more penetration of light (Jahnke, 2010; Kühl & Jørgensen, 1994). The transparency of sand grains could be influenced by its mineral composition. To investigate this, after conducting oxygen respiration

experiments (**chapter 2**), correlative analysis could be carried out using techniques such as energy-dispersive X-ray spectroscopy with scanning electron microscopy (EDX with SEM) or Raman spectroscopy to determine the sand grain mineral composition, and surface heterogeneity (Foucher et al., 2013; Hope et al., 2001; Pye, 2004). Machine learning approaches could also be used to determine different shape parameters of the sand grains (Kim et al., 2022) and correlate with the measured mineral composition and the oxygen respiration rates. By studying the properties of sand grains, including their mineral composition, shape, and oxygen respiration rates, we can gain a better understanding of the factors that control microbial colonization forming anoxic microenvironments in oxic sediments.

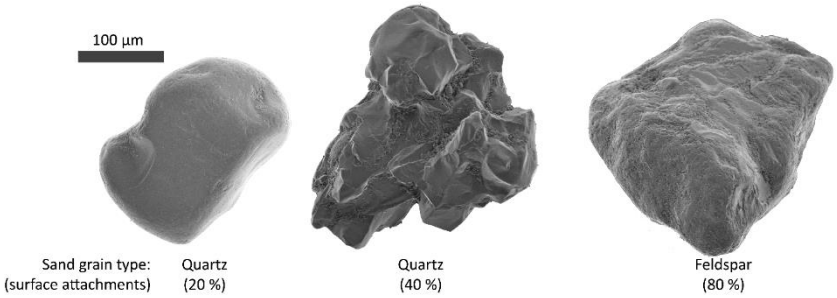

Figure 01: **Scanning electron micrographs of sandy sediments from the North Sea.** Sand grains collected from the same station showed high variability in shape, mineral composition and percent of surface attachments in the form of biofilm and attached minerals.

How is the transport of solute to the microbial community influenced by the shape of sand grains?

The microfluidic incubations performed with sands (**chapter 2**) were carried out under static conditions, limited to only diffusive transport. Therefore in order to

integrate the impact of pore water velocity on the formation of microenvironments, the results were incorporated in a two-dimensional spherical sand grain model. However, this does not incorporate the complex three dimensional transport of solute and the shape heterogeneity of the sand grains.

In future, microfluidic incubations using sandy sediments (**chapter 2**) should be performed with continuous flow within the microfluidic device. Implementing continuous flow in the microfluidic system will facilitate enhanced transport of solutes from the pore space to the sand grains. This approach allows for a more realistic simulation of advective and diffusive supply of solute to the sandy sediments. It is also recommended to integrate the microfluidic incubations with sensPIV (**chapter 3**) particles to simultaneously visualize both oxygen concentrations and the transport processes based on flow field. This will enable to study the microscale oxygen gradients experienced by the microbial communities residing on the sandy sediments (Glud, 2008; Huettel et al., 2003, 2014; Mendoza-Lera et al., 2017). Ahmerkamp et al., (2020) introduced a conceptual model that emphasizes the formation of anoxic microenvironments resulting from diffusion limitations based on the shape of sand grains (Figure 02). By observing the flow patterns, we can gain insights into the advection and diffusion rates of various substances, influencing the availability of solutes for the microbial communities (Franklin et al., 2019).

Visualizing O_2 gradients around sand grains is of utmost importance for investigating aerobic and anaerobic microbial activity, identifying oxic and anoxic zones (Berg et al., 2022), and gaining insights into the occurrence of denitrification and other anaerobic processes (Chua et al., 2022). By understanding the behavior of bacteria in response to oxygen gradients and flow, we can gain valuable information on microbial colonization. This comprehensive approach will enable a deeper understanding of the interplay between transport processes and

microbial behavior, contributing to our knowledge of microenvironment formation and its significance in biogeochemical cycling within marine ecosystems.

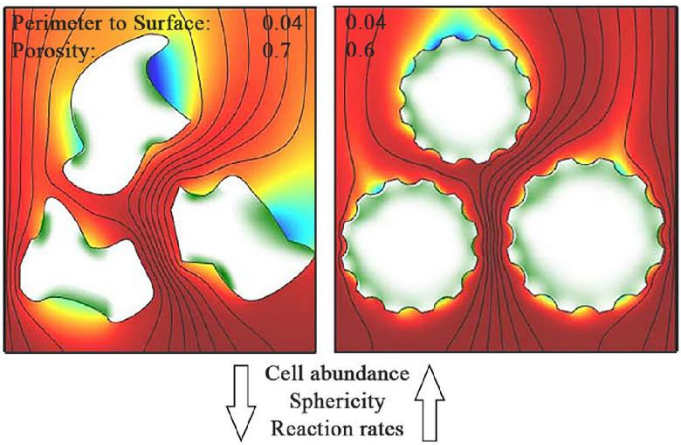

Figure 02: A schematic representation depicting the arrangement of microbial colonization and oxygen distribution within the pore spaces of sandy sediments for grains with varying shape. Oxic volumes are represented in red, anoxic volumes in blue, and microbial colonization in green. (Adapted from Ahmerkamp et al., (2022)

Influence of extracellular polymeric substances (EPS) and internal biofilm heterogeneity in formation of anoxic microenvironments?

Studies in the past have shown the sediment attached microbial community influences the flow-regime (Scheidweiler et al., 2019, 2021; Young et al., 2022) in porous media through the production of extracellular polymeric substances (EPS). EPS is a complex mixture of polymers produced by the microorganisms in aquatic environments. Recent studies have found that extracellular polymeric substances

(EPS) originating from benthic or pelagic primary producers change permeability altering the advective transport processes within sediment (Markale et al., 2023; Zetsche et al., 2011). Formation of EPS might as well lead to diffusion limitation transport regimes in pore space causing clogging, leading to the formation of anoxic microenvironments. The key factors responsible for driving EPS formation and internal respiration rates of a biofilm remain unidentified. To gain insights into factors influencing EPS formation, I propose conducting long-term incubations in a microfluidic device (**chapter 2**) using sensPIV particles (**chapter 3**) with controlled pore water flow on collected inactive sandy sediments with a fast-growing biofilm forming culture. This approach will help investigate the impact of parameters like pore water velocity and surface roughness on EPS formation. Two major learning from the above suggested experiment will be i) production of EPS influencing sediment stability and pore space clogging and ii) quantification of the alteration in advective flow due to EPS formation. Improved characterization of transport processes within the sediments will enhance our ability to estimate biogeochemical fluxes more accurately.

Effects of microscale concentrations gradients on biogeochemical cycling

This thesis emphasizes the significance of anoxic microenvironments in controlling the extent of denitrification within oxic sediments (**chapter 2**), hinting that other anoxic metabolic pathways might take place within these microenvironments. The results presented here, particularly the observed heterogeneity on individual sediments and strong gradients within the diffusive boundary layer, offers microscale insights on the level of biodiversity found in pore spaces. Previous research has reported sulfate reduction in oxic sediments, I speculate this to be in anoxic microenvironments (Bourceau et al., 2023; Jørgensen, 1977). To identify the potential microbial communities inhabiting the anoxic microenvironments and elucidate the overlap in the consumption of

electron acceptors, I suggest to employ advanced techniques such as Raman spectroscopy (Lee et al., 2021; Wagner, 2009) and BONCAT (Bioorthogonal non-canonical amino acid tagging) (Couradeau et al., 2019; Krukenberg et al., 2021). Raman spectroscopy allows us to probe the chemical composition and molecular structure of microorganisms within the microenvironments. Additionally, BONCAT is a powerful technique that enables the selective labeling and detection of actively metabolizing microbial cells. By incorporating specific non-canonical amino acids into the microbial community and detecting the labeled cells with fluorescence-based methods like FISH (Fluorescence in situ hybridization) for correlative imaging (Kitzinger et al., 2021). The above mentioned methods are also limited and provide information on uptake rate and cannot conclusively show what was used for respiration. Despite these limitations, the methods are valuable tools providing information about microbial communities within anoxic microenvironments.

What are the implications of methodological developments in terrestrial environments like soil?

Expanding the methods developed in this thesis to investigate the formation of microenvironments in soils holds great promise for advancing our understanding of microbial ecology and nutrient cycling in terrestrial ecosystems. Soil is a complex and dynamic matrix characterized by spatial heterogeneity in physical and chemical properties, which significantly influences microbial behavior and nutrient dynamics (Foster, 1988; Zhu et al., 2022). Studies in the past have employed planar optodes to quantify the volume of anoxic microenvironments (Keiluweit et al., 2017, 2018), with limited spatial resolution. By adapting the microfluidic approach used in the study of sandy sediments, we can study how microorganisms interact with and respond to oxygen gradients and flow conditions in soil. Understanding the formation and characteristics of microenvironments in soil will shed light on the spatial distribution of microbial

activity and nutrient turnover, enabling a more comprehensive understanding of ecosystem functioning.

What are the factors controlling oxygen transport at the microscale in sinking particles?

The formation and sinking of marine aggregates through the ocean's water column has significant ecological and biogeochemical impacts on carbon and nitrogen cycling (Asper et al., 1992). Despite being considered carriers of organic matter through their high sinking speeds, marine aggregates also serve as sites of intense microbial activity, facilitating rapid and efficient turnover of particulate organic carbon in the ocean (Figure 03; Azam, 1998; Iversen et al., 2010; Simon et al., 2002).

Several studies using microsensors have been conducted to study the time scales of solute in and out of a sinking particle (Ploug et al., 1997; Kiorboe et al., 2001). These studies provide great insights into the transport processes to a sinking particle, however using a microsensor hinders the flow around the sinking particle and lacks two dimensional mapping of O_2 concentrations in and around the particle. Integration of sensPIV particles (**chapter 3**) with the collected aggregates will provide information into the interplay between the transport of O_2 and microbial reaction rate on the marine aggregates, without hindering the flow field. For instance, the isolation of individual marine aggregates, as demonstrated by Karthäuser et al., (2021), can be combined with the use of the scale-free vertical tracking microscope to simulate flow (Krishnamurthy et al., 2020), along with the sensPIV particles.

Modeling investigations have attempted to assess the transport processes of sinking marine aggregates to explore their role in biogeochemical cycling. Most of these studies treated the aggregates as impermeable to flow and focused on fluxes

at the aggregate-water interface (Kiørboe & Jackson, 2001; Liu et al., 2012). It is crucial to consider that most marine aggregates exhibit high porosity, with porosities reaching up to 99% (Alldredge & Cohen, 1987). Therefore, representing aggregates as solid spheres in models may not accurately reflect their in situ characteristics. The models included the transport processes from vicinity to particle and incorporating the measured microbial respiration rates from the above suggested experiments will improve the flux estimates (Moradi et al., 2018, 2021). Further developments in the model have the capability to investigate the limitations, rates, and interactions of physical, chemical, and biological processes that may occur within the microenvironment of sinking aggregates. The transport estimates from the above mentioned experiments can be integrated into model studies to better estimate the transport fluxes and microbial respiration rates contributing to the formation of anoxic microenvironments influencing the biogeochemical cycling.

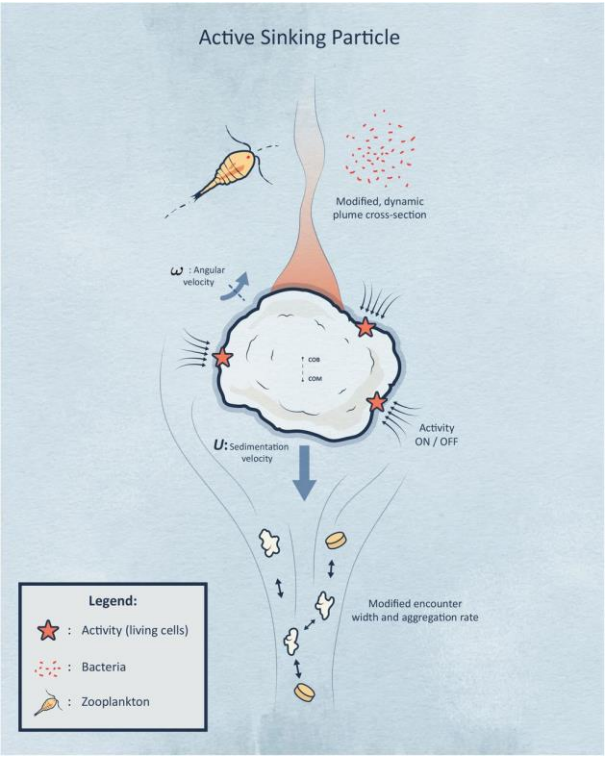

Figure 03: **Sinking particles in marine environments**. Active sinking particles were considered passive entities, influenced solely by the surrounding flow, presence of attached organisms might alter the local flow and sinking dynamics of these aggregates. (Adapted from Krishnamurthy et al., 2023)

What are the oxygen concentrations thresholds for the microbial community residing in the microenvironments, for anaerobic respiration over aerobic respiration?

The oxic-anoxic interface in marine environments is a critical zone where distinct microenvironments coexist, and the interplay between transport processes and

microbial activity plays a pivotal role in shaping biogeochemical processes (**chapter 2-3**). Microorganisms residing in these distinct microenvironments encounter varying oxygen concentrations, leading to diverse metabolic activities and physiological responses (**chapter 4**). In low-oxygen microenvironments with reduced or absent oxygen, microorganisms rely on alternative anaerobic metabolic pathways to meet their energy requirements (Bianchi et al., 2018; Froelich et al., 1979; Zakem et al., 2020). However, the precise oxygen concentration thresholds that triggers this metabolic switch remains largely unknown.

To elucidate this threshold, a microfluidic device presented in **chapter 4** can be utilized to cultivate bacterial cultures, such as denitrifiers in combination with labeled isotopic incubations within the microfluidic system. The bacterial community can be exposed to well-defined oxygen concentrations and further analyzed in nanoscale secondary ion mass spectrometry (Alcolombri et al., 2022) for precise determination of the concentration at which the switch occurs, for example between oxygen and nitrate respiration by facultative denitrifiers (Gao et al., 2010; Marchant et al., 2017). By pinpointing this critical transition point, we can gain valuable insights into the metabolic strategies of microorganisms in response to changing oxygen availability.

Furthermore, integrating this precise determination of the respiration metabolism switch into global nitrogen cycling and greenhouse gas modeling approaches could significantly enhance our understanding of how microbial activity at the oxic-anoxic interface influences larger-scale biogeochemical processes (Ahmerkamp et al., 2017; Falkowski, 2006; Falkowski et al., 2008; Hutchins & Fu, 2017; Kuypers et al., 2018; Marchant et al., 2016). Such modeling efforts will contribute to better predictions of nitrogen cycling dynamics and greenhouse gas emissions in marine environments, which, in turn, are crucial for

assessing the impacts of climate change and human activities on the oceans and the Earth's atmosphere.

What are the organic carbon and electron donor limitations within microenvironments?

The limitation of organic carbon and electron donor availability can play a crucial role in creating strong zonations within microbial communities in anoxic microenvironments (Jäntti et al., 2022; Rojas et al., 2021). Although this aspect has not been explicitly discussed in this thesis where I instead focused on O_2 as an electron acceptor, it should be considered as an important factor. In the environment, microbial activity is often limited by the availability of organic carbon sources, such as dissolved organic matter or particulate organic carbon, which serve as essential substrates for microbial metabolism (Hobbie & Hobbie, 2013; Lønborg et al., 2022). Similarly, the presence and availability of electron donors, like organic compounds or inorganic substances, significantly influence the microbial redox reactions. Microbes adapt their metabolism based on the type and concentration of available electron donors, leading to the establishment of distinct microbial microenvironments with specific metabolic capabilities (Ishii et al., 2018). These distinct microenvironments, in turn, can lead to the formation of pronounced zonations within microenvironments, where different microbial communities thrive in response to varying organic carbon and electron donor availability (Louca et al., 2023; Lovley, 2022). Understanding the dynamics of organic carbon limitation and electron donor availability in anoxic microenvironments is vital to comprehensively assess the role of microbial communities in biogeochemical cycling. These limitations can shape the microbial community structure, metabolic activities, and nutrient cycling processes.

5.3 Concluding remarks

This thesis advances our understanding of microbial interactions and their impact on biogeochemical cycling by integrating microscale microbial reaction rates with transport processes to investigate the formation of microenvironments. These microenvironments play a critical role in shaping the microbial community and influencing biogeochemical processes, which were previously challenging to study using conventional methods. This thesis work shows that:

i) the interplay of transport processes and the patchy microbial reaction rates is a crucial factor in shaping the formation of distinct microenvironments, leading, for example to the development of anoxic microenvironments in oxic sediments. These microenvironments, which are not detectable via conventional techniques, represent an entirely new mechanism by which anaerobic processes are mediated in oxic environments. By quantifying the volume of these anoxic microenvironments, we gain a better understanding of the extent of denitrification in sediments, ultimately improving our estimates of total nitrogen cycling within these environments.

ii) the newly developed sensPIV method offers a non-invasive approach to map the transport and microbial reaction of oxygen at microbially relevant scales. This method emphasizes the significance of simultaneously studying transport processes and microbial reaction rates, thereby enhancing our understanding of microscale transport processes.

iii) exposing the microbial community to precisely controlled solute concentrations revealed different microbial adaptations and activity within distinct microenvironments. Microorganisms exhibited varied physiological responses and growth rates as a response to local changes in oxygen availability, diverging from the bulk measurements of the overall activity.

In conclusion, within seemingly homogeneous environments, there are significant differences in the microbial activity and behavior, influenced by microscale gradients due to solute transport and microbial reaction rates. These microenvironments influence nutrient cycling, carbon sequestration, and the overall functioning of marine ecosystems, ultimately regulating the Earth's system. As we focus on smaller scales where microbial interactions take place in the ocean, it is essential to give due consideration to physical processes, as they profoundly influence the microenvironment experienced by marine microbes and their interactions within it.

Bibliography

Ahmerkamp, S., Jalaluddin, F. M., Cui, Y., Brumley, D. R., Pacherres, C. O., Berg, J. S., Stocker, R., Kuypers, M. M. M., Koren, K., & Behrendt, L. (2022). Simultaneous visualization of flow fields and oxygen concentrations to unravel transport and metabolic processes in biological systems. *Cell Reports Methods*, *2*(5), 100216. https://doi.org/10.1016/j.crmeth.2022.100216

Ahmerkamp, S., Marchant, H. K., Peng, C., Probandt, D., Littmann, S., Kuypers, M. M. M., & Holtappels, M. (2020). The effect of sediment grain properties and porewater flow on microbial abundance and respiration in permeable sediments. *Scientific Reports*, *10*(1), 1–12. https://doi.org/10.1038/s41598-020-60557-7

Ahmerkamp, S., Winter, C., Krämer, K., Beer, D. de, Janssen, F., Friedrich, J., Kuypers, M. M. M., & Holtappels, M. (2017). Regulation of benthic oxygen fluxes in permeable sediments of the coastal ocean. *Limnology and Oceanography*, *62*(5), 1935–1954. https://doi.org/10.1002/lno.10544

Alcolombri, U., Pioli, R., Stocker, R., & Berry, D. (2022). Single-cell stable isotope probing in microbial ecology. *ISME Communications*, *2*(1), 1–9. https://doi.org/10.1038/s43705-022-00142-3

Alldredge, A. L., & Cohen, Y. (1987). Can Microscale Chemical Patches Persist in the Sea? Microelectrode Study of Marine Snow, Fecal Pellets. *Science*, *235*(4789), 689–691. https://doi.org/10.1126/science.235.4789.689

Anderson, J. G., & Meadows, P. S. (1978). Microenvironments in marine sediments. *Proceedings of the Royal Society of Edinburgh. Section B.*

Biological Sciences, *76*(1–3), 1–16. https://doi.org/10.1017/S0269727000002761

Asper, V. L., Deuser, W. G., Knauer, G. A., & Lohrenz, S. E. (1992). Rapid coupling of sinking particle fluxes between surface and deep ocean waters. *Nature*, *357*(6380), 670–672. https://doi.org/10.1038/357670a0

Azam, F. (1998). Microbial Control of Oceanic Carbon Flux: The Plot Thickens. *Science*, *280*(5364), 694–696. https://doi.org/10.1126/science.280.5364.694

Barclay, D. R., & Buckingham, M. J. (2009). On the shapes of natural sand grains. *Journal of Geophysical Research*, *114*(B2), B02209. https://doi.org/10.1029/2008JB005993

Berg, J. S., Ahmerkamp, S., Pjevac, P., Hausmann, B., Milucka, J., & Kuypers, M. M. M. (2022). How low can they go? Aerobic respiration by microorganisms under apparent anoxia. *FEMS Microbiology Reviews*, *46*(3), 1–14. https://doi.org/10.1093/femsre/fuac006

Bianchi, D., Weber, T. S., Kiko, R., & Deutsch, C. (2018). Global niche of marine anaerobic metabolisms expanded by particle microenvironments. *Nature Geoscience*, *11*(4), 263–268. https://doi.org/10.1038/s41561-018-0081-0

Bourceau, O. M., Ferdelman, T., Lavik, G., Mussmann, M., Kuypers, M. M. M., & Marchant, H. K. (2023). Simultaneous sulfate and nitrate reduction in coastal sediments. *ISME Communications*, *3*(1), 37–40. https://doi.org/10.1038/s43705-023-00222-y

Chua, E. J., Huettel, M., Fennel, K., & Fulweiler, R. W. (2022). A case for addressing

the unresolved role of permeable shelf sediments in ocean denitrification. *Limnology And Oceanography Letters*, *7*(1), 11–25. https://doi.org/10.1002/lol2.10218

Couradeau, E., Sasse, J., Goudeau, D., Nath, N., Hazen, T. C., Bowen, B. P., Chakraborty, R., Malmstrom, R. R., & Northen, T. R. (2019). Probing the active fraction of soil microbiomes using BONCAT-FACS. *Nature Communications*, *10*(1), 2770. https://doi.org/10.1038/s41467-019-10542-0

Doyle, L. J. (1965). *Chapter IV The Continental Shelves* (pp. 53–83). https://doi.org/10.1016/S0422-9894(08)70763-3

Falkowski, P. G. (2006). Tracing Oxygen's Imprint on Earth's Metabolic Evolution. *Science*, *311*(5768), 1724–1725. https://doi.org/10.1126/science.1125937

Falkowski, P. G., Fenchel, T., & Delong, E. F. (2008). The microbial engines that drive earth's biogeochemical cycles. *Science*, *320*(5879), 1034–1039. https://doi.org/10.1126/science.1153213

Folk, R. L. (1954). The Distinction between Grain Size and Mineral Composition in Sedimentary-Rock Nomenclature. *The Journal of Geology*, *62*(4), 344–359. https://doi.org/10.1086/626171

Foster, R. C. (1988). Microenvironments of soil microorganisms. *Biology and Fertility of Soils*, *6*(3), 189–203. https://doi.org/10.1007/BF00260816

Foucher, F., Lopez-Reyes, G., Bost, N., Rull-Perez, F., Rüßmann, P., & Westall, F. (2013). Effect of grain size distribution on Raman analyses and the

consequences for in situ planetary missions. *Journal of Raman Spectroscopy*, *44*(6), 916–925. https://doi.org/10.1002/jrs.4307

Franklin, S., Vasilas, B., & Jin, Y. (2019). More than Meets the Dye: Evaluating Preferential Flow Paths as Microbial Hotspots. *Vadose Zone Journal*, *18*(1), 1–8. https://doi.org/10.2136/vzj2019.03.0024

Froelich, P. N., Klinkhammer, G. P., Bender, M. L., Luedtke, N. A., Heath, G. R., Cullen, D., Dauphin, P., Hammond, D., Hartman, B., & Maynard, V. (1979). Early oxidation of organic matter in pelagic sediments of the eastern equatorial Atlantic: suboxic diagenesis. *Geochimica et Cosmochimica Acta*, *43*(7), 1075–1090. https://doi.org/10.1016/0016-7037(79)90095-4

Gao, H., Schreiber, F., Collins, G., Jensen, M. M., Kostka, J. E., Lavik, G., De Beer, D., Zhou, H. Y., & Kuypers, M. M. M. (2010). Aerobic denitrification in permeable Wadden Sea sediments. *ISME Journal*, *4*(3), 417–426. https://doi.org/10.1038/ismej.2009.127

Ghadr, S., & Assadi-Langroudi, A. (2019). Effect of Grain Size and Shape on Undrained Behaviour of Sands. *International Journal of Geosynthetics and Ground Engineering*, *5*(3), 18. https://doi.org/10.1007/s40891-019-0170-1

Glud, R. N. (2008). Oxygen dynamics of marine sediments. *Marine Biology Research*, *4*(4), 243–289. https://doi.org/10.1080/17451000801888726

Hobbie, J. E., & Hobbie, E. A. (2013). Microbes in nature are limited by carbon and energy: the starving-survival lifestyle in soil and consequences for estimating microbial rates. *Frontiers in Microbiology*, *4*. https://doi.org/10.3389/fmicb.2013.00324

Hope, G. A., Woods, R., & Munce, C. G. (2001). Raman microprobe mineral identification. *Minerals Engineering*, *14*(12), 1565–1577. https://doi.org/10.1016/S0892-6875(01)00175-3

Huettel, M., Berg, P., & Kostka, J. E. (2014). Benthic Exchange and Biogeochemical Cycling in Permeable Sediments. *Annual Review of Marine Science*, *6*(1), 23–51. https://doi.org/10.1146/annurev-marine-051413-012706

Huettel, M., Røy, H., Precht, E., & Ehrenhauss, S. (2003). Hydrodynamical impact on biogeochemical processes in aquatic sediments. *Hydrobiologia*, *494*(1–3), 231–236. https://doi.org/10.1023/A:1025426601773

Hutchins, D. A., & Fu, F. (2017). Microorganisms and ocean global change. *Nature Microbiology*, *2*(May). https://doi.org/10.1038/nmicrobiol.2017.58

Ishii, S., Suzuki, S., Tenney, A., Nealson, K. H., & Bretschger, O. (2018). Comparative metatranscriptomics reveals extracellular electron transfer pathways conferring microbial adaptivity to surface redox potential changes. *The ISME Journal*, *12*(12), 2844–2863. https://doi.org/10.1038/s41396-018-0238-2

Iversen, M. H., Nowald, N., Ploug, H., Jackson, G. A., & Fischer, G. (2010). High resolution profiles of vertical particulate organic matter export off Cape Blanc, Mauritania: Degradation processes and ballasting effects. *Deep Sea Research Part I: Oceanographic Research Papers*, *57*(6), 771–784. https://doi.org/10.1016/j.dsr.2010.03.007

Jahnke, R. A. (2010). *Global Synthesis*. 597–615. https://doi.org/10.1007/978-3-540-92735-8_16

Jäntti, H., Jilbert, T., Aalto, S. L., Simojoki, A., Mangayil, R., Peura, S., & Rissanen, A. J. (2022). The role of organic matter and microbial community controlling nitrate reduction under elevated ferrous iron concentrations in boreal lake sediments. *Hydrobiologia*, *849*(9), 2145–2160. https://doi.org/10.1007/s10750-022-04858-0

Jørgensen, B. B. (1977). Bacterial sulfate reduction within reduced microniches of oxidized marine sediments. *Marine Biology*, *41*(1), 7–17. https://doi.org/10.1007/BF00390576

Karthäuser, C., Ahmerkamp, S., Marchant, H. K., Bristow, L. A., Hauss, H., Iversen, M. H., Kiko, R., Maerz, J., Lavik, G., & Kuypers, M. M. M. (2021). Small sinking particles control anammox rates in the Peruvian oxygen minimum zone. *Nature Communications*, *12*(1), 3235. https://doi.org/10.1038/s41467-021-23340-4

Keiluweit, M., Gee, K., Denney, A., & Fendorf, S. (2018). Anoxic microsites in upland soils dominantly controlled by clay content. *Soil Biology and Biochemistry*, *118*(December 2017), 42–50. https://doi.org/10.1016/j.soilbio.2017.12.002

Keiluweit, M., Wanzek, T., Kleber, M., Nico, P., & Fendorf, S. (2017). Anaerobic microsites have an unaccounted role in soil carbon stabilization. *Nature Communications*, *8*(1), 1–8. https://doi.org/10.1038/s41467-017-01406-6

Kim, Y., Ma, J., Lim, S. Y., Song, J. Y., & Yun, T. S. (2022). Determination of shape parameters of sands: a deep learning approach. *Acta Geotechnica*, *17*(4), 1521–1531. https://doi.org/10.1007/s11440-022-01464-1

Kiørboe, T., & Jackson, G. A. (2001). Marine snow, organic solute plumes, and

optimal chemosensory behavior of bacteria. *Limnology and Oceanography*, *46*(6), 1309–1318. https://doi.org/10.4319/lo.2001.46.6.1309

Kiørboe, T., Ploug, H., & Thygesen, U. (2001). Fluid motion and solute distribution around sinking aggregates. I. Small-scale fluxes and heterogeneity of nutrients in the pelagic environment. *Marine Ecology Progress Series, 211*(Kiørboe 2000), 1–13.

Kiørboe, T., & Thygesen, U. (2001). Fluid motion and solute distribution around sinking aggregates. II. Implications for remote detection by colonizing zooplankters. *Marine Ecology Progress Series, 211*, 15–25.

Kitzinger, K., Tienken, D., Littmann, S., Kidane, A. T., Kuypers, M. M. M., & Milucka, J. (2021). *Assigning Function to Phylogeny: FISH-nanoSIMS* (pp. 207–224). https://doi.org/10.1007/978-1-0716-1115-9_13

Krishnamurthy, D., Li, H., Benoit du Rey, F., Cambournac, P., Larson, A. G., Li, E., & Prakash, M. (2020). Scale-free vertical tracking microscopy. *Nature Methods*, *17*(10), 1040–1051. https://doi.org/10.1038/s41592-020-0924-7

Krishnamurthy, D., Pepper, R., & Prakash, M. (2023). Active sinking particles: sessile suspension feeders significantly alter the flow and transport to sinking aggregates. *Journal of The Royal Society Interface*, *20*(199). https://doi.org/10.1098/rsif.2022.0537

Krukenberg, V., Reichart, N. J., Spietz, R. L., & Hatzenpichler, R. (2021). Microbial Community Response to Polysaccharide Amendment in Anoxic Hydrothermal Sediments of the Guaymas Basin. *Frontiers in Microbiology*, *12*. https://doi.org/10.3389/fmicb.2021.763971

Kühl, M., & Jørgensen, B. B. (1994). The light field of microbenthic communities: Radiance distribution and microscale optics of sandy coastal sediments. *Limnology and Oceanography*, *39*(6), 1368–1398. https://doi.org/10.4319/lo.1994.39.6.1368

Kuypers, M. M. M., Marchant, H. K., & Kartal, B. (2018). The microbial nitrogen-cycling network. *Nature Reviews Microbiology*, *16*(5), 263–276. https://doi.org/10.1038/nrmicro.2018.9

Lee, K. S., Landry, Z., Pereira, F. C., Wagner, M., Berry, D., Huang, W. E., Taylor, G. T., Kneipp, J., Popp, J., Zhang, M., Cheng, J.-X., & Stocker, R. (2021). Raman microspectroscopy for microbiology. *Nature Reviews Methods Primers*, *1*(1), 80. https://doi.org/10.1038/s43586-021-00075-6

Liu, B., Kindler, K., & Khalili, A. (2012). Dynamic solute release from marine aggregates. *Limnology and Oceanography: Fluids and Environments*, *2*(1), 109–120. https://doi.org/10.1215/21573689-2016772

Lønborg, C., Baltar, F., Calleja, M. L., & Morán, X. A. G. (2022). Heterotrophic Bacteria Respond Differently to Increasing Temperature and Dissolved Organic Carbon Sources in Two Tropical Coastal Systems. *Journal of Geophysical Research: Biogeosciences*, *127*(12). https://doi.org/10.1029/2022JG006890

Louca, S., Taylor, G. T., Astor, Y. M., Buck, K. N., & Muller-Karger, F. E. (2023). Transport-limited reactions in microbial systems. *Environmental Microbiology*, *25*(2), 268–282. https://doi.org/10.1111/1462-2920.16275

Lovley, D. R. (2022). Electrotrophy: Other microbial species, iron, and electrodes as electron donors for microbial respirations. *Bioresource Technology*, *345*,

126553. https://doi.org/10.1016/j.biortech.2021.126553

Marchant, H. K., Ahmerkamp, S., Lavik, G., Tegetmeyer, H. E., Graf, J., Klatt, J. M., Holtappels, M., Walpersdorf, E., & Kuypers, M. M. M. (2017). Denitrifying community in coastal sediments performs aerobic and anaerobic respiration simultaneously. *ISME Journal*, *11*(8), 1799–1812. https://doi.org/10.1038/ismej.2017.51

Marchant, H. K., Holtappels, M., Lavik, G., Ahmerkamp, S., Winter, C., & Kuypers, M. M. M. (2016). Coupled nitrification-denitrification leads to extensive N loss in subtidal permeable sediments. *Limnology and Oceanography*, *61*(3), 1033–1048. https://doi.org/10.1002/lno.10271

Markale, I., Carrel, M., Kurz, D. L., Morales, V. L., Holzner, M., & Jiménez-Martínez, J. (2023). Internal Biofilm Heterogeneities Enhance Solute Mixing and Chemical Reactions in Porous Media. *Environmental Science and Technology*, *57*(21), 8065–8074. https://doi.org/10.1021/acs.est.2c09082

Mendoza-Lera, C., Frossard, A., Knie, M., Federlein, L. L., Gessner, M. O., & Mutz, M. (2017). Importance of advective mass transfer and sediment surface area for streambed microbial communities. *Freshwater Biology*, *62*(1), 133–145. https://doi.org/10.1111/fwb.12856

Moradi, N., Klawonn, I., Iversen, M. H., Wenzhöfer, F., Grossart, H. P., Ploug, H., Fischer, G., & Khalili, A. (2021). A Novel Measurement-Based Model for Calculating Diffusive Fluxes Across Substrate-Water Interfaces of Marine Aggregates, Sediments and Biofilms. *Frontiers in Marine Science*, *8*(August), 1–12. https://doi.org/10.3389/fmars.2021.689977

Moradi, N., Liu, B., Iversen, M., Kuypers, M. M., Ploug, H., & Khalili, A. (2018). A

new mathematical model to explore microbial processes and their constraints in phytoplankton colonies and sinking marine aggregates. *Science Advances*, *4*(10). https://doi.org/10.1126/sciadv.aat1991

Ploug, H., Kühl, M., Buchholz-Cleven, B., & Jørgensen, B. B. (1997). Anoxic aggregates - An ephemeral phenomenon in the pelagic environment? *Aquatic Microbial Ecology*, *13*(3), 285–294. https://doi.org/10.3354/ame013285

Ploug, H., & Jørgensen, B. (1999). A net-jet flow system for mass transfer and microsensor studies of sinking aggregates. *Marine Ecology Progress Series, 176(1987)*, 279–290.

Pye, K. (2004). Forensic examination of rocks, sediments, soils and dusts using scanning electron microscopy and X-ray chemical microanalysis. *Geological Society Special Publication*, *232*(1942), 103–122. https://doi.org/10.1144/GSL.SP.2004.232.01.11

Rojas, C. A., De Santiago Torio, A., Park, S., Bosak, T., & Klepac-Ceraj, V. (2021). Organic Electron Donors and Terminal Electron Acceptors Structure Anaerobic Microbial Communities and Interactions in a Permanently Stratified Sulfidic Lake. *Frontiers in Microbiology*, *12*. https://doi.org/10.3389/fmicb.2021.620424

Scheidweiler, D., Mendoza-Lera, C., Mutz, M., & Risse-Buhl, U. (2021). Overlooked Implication of Sediment Transport at Low Flow: Migrating Ripples Modulate Streambed Phototrophic and Heterotrophic Microbial Activity. *Water Resources Research*, *57*(3). https://doi.org/10.1029/2020WR027988

Scheidweiler, D., Peter, H., Pramateftaki, P., de Anna, P., & Battin, T. J. (2019). Unraveling the biophysical underpinnings to the success of multispecies biofilms in porous environments. *ISME Journal*, *13*(7), 1700–1710. https://doi.org/10.1038/s41396-019-0381-4

Simon, M., Grossart, H., Schweitzer, B., & Ploug, H. (2002). Microbial ecology of organic aggregates in aquatic ecosystems. *Aquatic Microbial Ecology*, *28*, 175–211. https://doi.org/10.3354/ame028175

Wagner, M. (2009). Single-Cell Ecophysiology of Microbes as Revealed by Raman Microspectroscopy or Secondary Ion Mass Spectrometry Imaging. *Annual Review of Microbiology*, *63*(1), 411–429. https://doi.org/10.1146/annurev.micro.091208.073233

Weise, W., & Rheinheimer, G. (1977). Scanning electron microscopy and epifluorescence investigation of bacterial colonization of marine sand sediments. *Microbial Ecology*, *4*(3), 175–188. https://doi.org/10.1007/BF02015075

Yawata, Y., Nguyen, J., Stocker, R., & Rusconi, R. (2016). Microfluidic studies of biofilm formation in dynamic environments. *Journal of Bacteriology*, *198*(19), 2589–2595. https://doi.org/10.1128/JB.00118-16

Young, E., Melaugh, G., & Allen, R. J. (2022). Pinning transition in biofilm structure driven by active layer dynamics. *BioRxiv*, 2022.03.21.485164. https://www.biorxiv.org/content/10.1101/2022.03.21.485164v1%0Ahttps://www.biorxiv.org/content/10.1101/2022.03.21.485164v1.abstract

Zakem, E. J., Polz, M. F., & Follows, M. J. (2020). Redox-informed models of global biogeochemical cycles. *Nature Communications*, *11*(1), 1–10.

https://doi.org/10.1038/s41467-020-19454-w

Zetsche, E., Paterson, D. M., Lumsdon, D. G., & Witte, U. (2011). Temporal variation in the sediment permeability of an intertidal sandflat. *Marine Ecology Progress Series*, *441*, 49–63. https://doi.org/10.3354/meps09390

Zhu, K., Ye, X., Ran, H., Zhang, P., & Wang, G. (2022). Contrasting effects of straw and biochar on microscale heterogeneity of soil O2 and pH: Implication for N2O emissions. *Soil Biology and Biochemistry*, *166*(July 2021), 108564. https://doi.org/10.1016/j.soilbio.2022.108564

Author contribution

Chapter 2:

Microenvironments on individual sand grains enhance nitrogen loss in coastal sediments

Farooq Moin Jalaluddin, Soeren Ahmerkamp, Hannah K. Marchant, Volker Meyer, Klaus Koren, Marcel MM Kuypers

The research was designed by S.A., M.M.M.K. and me. I performed the experiments. I and S.A. designed the chip, and developed the model. I and S.A. analysed and visualized data. V.M., developed the lifetime imaging modulation box. K.K. provided sensor-particles. I wrote the manuscript with S.A., H.K.M. and M.M.M.K. with the contributions from all co-authors.
Manuscript under review in PNAS.

Chapter 3:

Simultaneous visualization of flow fields and oxygen concentrations to unravel transport and metabolic processes in biological systems

Soeren Ahmerkamp*, Farooq Moin Jalaluddin*, Yuan Cui*, Douglas R. Brumley, Cesar O. Pacherres, Jasmine Berg, Roman Stocker, Marcel MM Kuypers, Klaus Koren, Lars Behrendt

*equal contribution

I and S.A. performed experiments with laboratory particles and processed data. S.A. developed and built optical setups. S.A., L.B., K.K, M.M.M.K., J.B., D.R.B. and R.S. conceived the study and interpreted data. K.K. synthesized sensor particles. Y.C.

and L.B. performed experiments with microfluidic chips and processed data. C.O.P. and S.A. developed flow-chamber setup, performed experiments with coral fragments and processed data. C.O.P. performed microsensor measurement. All authors edited and approved the paper.
Manuscript published in Cell Report Methods.

Chapter 4:
Single cell growth rates in well-defined oxygen gradients using a novel microfluidic device
Farooq Moin Jalaluddin*, Juliane Schoetz*, Soeren Ahmerkamp, Hannah K. Marchant, Wiebke Mohr, Marcel M.M. Kuypers

potential co-authors who were involved in the presented work but have not yet read the manuscript:
Jana Milucka, Lars Behrendt, Simon van Vliet, Klaus Koren, Sten Littmann

*equal contribution

The research was designed by J.S., S.A., W.M., J.M., M.M.M.K. and me. I, S.A. and J.S. produced microfluidic chips. I performed experiments with sensPIV particles, and processed data. I and S.A. developed models. I and J.S. performed experiments with Photobacterium Aquimaris in microfluidic chips. I, J.S and S.A. discussed and interpreted the results with the help of W.M., J.M. and M.M.M.K. S.A. and J.S. designed silica wafer. S.V.V. and L.B. contributed microfluidic designs and expertise on wafer/microfluidic chip production. K.K. prepared sensor-particles. S.L. contributed with NanoSIMS and microscopy expertise. I wrote the manuscript with S.A., and H.K.M with the contributions from all authors.
Manuscript in preparation.

Versicherung an Eides Statt / *Affirmation in lieu of an oath*

gem. § 5 Abs. 5 der Promotionsordnung vom 18.06.2018 /
according to § 5 (5) of the Doctoral Degree Rules and Regulations of 18 June, 2018

Ich / I, Farooq Moin, Jalaluddin
(Vorname / First *Name*, Name / *Name*, Anschrift / *Address*, ggf. Matr.-Nr. / *student ID no., if applicable)*

versichere an Eides Statt durch meine Unterschrift, dass ich die vorliegende Dissertation selbständig und ohne fremde Hilfe angefertigt und alle Stellen, die ich wörtlich dem Sinne nach aus Veröffentlichungen entnommen habe, als solche kenntlich gemacht habe, mich auch keiner anderen als der angegebenen Literatur oder sonstiger Hilfsmittel bedient habe und die zu Prüfungszwecken beigelegte elektronische Version (PDF) der Dissertation mit der abgegebenen gedruckten Version identisch ist. / *With my signature I affirm in lieu of an oath that I prepared the submitted dissertation independently and without illicit assistance from third parties, that I appropriately referenced any text or content from other sources, that I used only literature and resources listed in the dissertation, and that the electronic (PDF) and printed versions of the dissertation are identical.*

Ich versichere an Eides Statt, dass ich die vorgenannten Angaben nach bestem Wissen und Gewissen gemacht habe und dass die Angaben der Wahrheit entsprechen und ich nichts verschwiegen habe. */ I affirm in lieu of an oath that the information provided herein to the best of my knowledge is true and complete.*

Die Strafbarkeit einer falschen eidesstattlichen Versicherung ist mir bekannt, namentlich die Strafandrohung gemäß § 156 StGB bis zu drei Jahren Freiheitsstrafe oder Geldstrafe bei vorsätzlicher Begehung der Tat bzw. gemäß § 161 Abs. 1 StGB bis zu einem Jahr Freiheitsstrafe oder Geldstrafe bei fahrlässiger Begehung. / *I am aware that a false affidavit is a criminal offence which is punishable by law in accordance with § 156 of the German Criminal Code (StGB) with up to three years imprisonment or a fine in case of intention, or in accordance with § 161 (1) of the German Criminal Code with up to one year imprisonment or a fine in case of negligence.*

Bremen, 31/07/2023

Ort / *Place*, Datum / *Date*

Unterschrift / *Signature*